INCREASING THE SURFACE AREA OF IRIDIUM OXIDE AS AN OXYGEN EVOLUTION REACTION CATALYST

This project report is submitted in part fulfilment of the requirements of the Master: Applied Sciences in Chemistry

Department of Chemistry,
Cape Peninsula University of Technology

By

ZIYANDA JABE

Student No. 213008270

Supervisor: Prof. Mangaka Matoetoe (Chemistry)

Co-Supervisor: Dr. Jessica Chamier (Chemical Engineering)

Date: 15th August 2024

DECLARATION

I, Ziyanda Sikho Jabe, declare that the contents of this thesis/dissertation represent my unaided work and that the thesis/dissertation has not previously been submitted for academic examination towards any qualification. Furthermore, it represents my own opinions and not necessarily those of the Cape Peninsula University of Technology.

Signed:  **Date: 15th August 2024**

ABSTRACT

Hydrogen is a promising clean energy carrier for transportation and chemical industries, helping reduce fossil fuel emissions and combat climate change. Proton exchange membrane water electrolysis (PEMWE) efficiently produces high-purity hydrogen with minimal CO_2 emissions when powered by renewable energy sources like solar and wind. However, the oxygen evolution reaction (OER) at the PEMWE anode is kinetically challenging and requires significant amounts of noble metal oxide electrocatalysts. Iridium oxide (IrO_2) is the preferred OER catalyst due to its high activity and corrosion resistance, but its high cost and scarcity hinder widespread use. To overcome this, researchers are exploring ways to reduce iridium content, such as using support materials to improve efficiency and extend the catalyst duration.

This study focused on exploring different pathways to increase the surface area of iridium oxide-based and mixed oxide catalysts from metallic iridium supplied by local mines. Modifications were applied using various oxidising agents in the Adams' fusion method to adjust the catalyst's oxidation state, porosity, surface area, and morphology. Post-treatment processes involving different cooling rates were applied to modify the phase and crystallinity of metal oxides. Dispersing IrO_x on high-surface-area support material and mixed oxide to increase the surface area and OER performance.

The physicochemical properties of the in-house nanomaterials were confirmed using various analytical techniques. The X-ray spectroscopy (XRD) and high-resolution-scanning transmission electron microscopy (HR-STEM) analyses revealed that the synthesised catalysts were amorphous/low crystalline nanomaterials with an average particle size range $\pm$ 2 - 5 nm. X-ray photoelectron spectroscopy (XPS) showed that the in-house are in the Ir^{3+}/ Ir^{4+} oxidation state. According to the scanning electron microscopy-energy dispersive X-ray spectroscopy (SEM-EDX), the nanomaterials exhibit different iridium loading. The stability and activity of the iridium oxide-based nanomaterials for oxygen evolution reaction (OER) were evaluated using the rotating disk electrode (RDE) technique in an acidic electrolyte.

The highest OER performance was obtained from the catalyst produced by using sodium peroxide oxidising agent compared to barium peroxide. Different cooling rates did not result in a significant increase in catalyst surface area. A notable increase in surface area was achieved due to the usage of barium peroxide from 11.0 m^2/g to 31.7 m^2/g, while for mixed-oxide catalyst 18.4 m^2/g was obtained. Furthermore, the electrochemical stability of the catalyst was achieved for $IrO_{x\text{-}(Ba)}$ and $TaIrO_x$ catalysts, however at the expense of OER activity. The $IrO_{x\text{-}}$

$_{(Na)}$ catalyst outperformed both $IrO_{x\text{-}(Ba)}$ and $TaIrO_x$ mixed oxide with greater mass-specific activity at 1.525 V. Even though the $IrO_{x\text{-}(Na)\text{-}(R)}$ catalyst had the highest OER compared to all catalysts it was the least stable. For $TaIrO_x$, XPS revealed that Ta is present as Ta^{5+} (Ta_2O_5) at the catalyst surface, this likely affected OER activity since it is a non-conductive material.

ACKNOWLEDGEMENTS

Primarily, I thank the almighty God for the strength and knowledge I had throughout this project.

I would like to express my genuine gratitude to my supervisor Dr. Jessica Chamier played a pivotal role in shaping the direction of my research, providing insightful feedback, and offering constructive criticism that significantly enhanced the quality of this work. Her expertise, patience, and dedication were instrumental in helping me navigate through the challenges and complexities of the research process.

I am also grateful to Prof. M.C. Matoetoe for her unwavering encouragement and belief in my abilities, which served as a constant source of motivation during moments of doubt and uncertainty. Both supervisor mentorship not only contributed to the academic success of this thesis but also fostered my personal and professional growth.

I want to express my gratitude to the Hydrogen South Africa Catalysis Centre and the University of Cape Town for their assistance in facilitating and providing me with the necessary equipment and resources.

To my family, my friends, colleagues, and everyone else who walked this journey with me, I appreciate your support.

DEDICATION

This work is dedicated to my late mother, Nokondla Jabe, as well as the Jabe and Matshaya families. I want to extend a huge thank you to my family for supporting me through thick and thin. Without your encouragement, motivation, and prayers, I would not have been able to achieve this level of success.

TABLE OF CONTENTS

LIST OF FIGURES

LIST OF TABLES

GLOSSARY

List of abbreviations

AWE	Alkaline water electrolysis.
BET	Brunauer, Emmett and Teller
CA	Chronoamperometry
Cdl	Double-layer capacity
CV	Cyclic voltammetry
ECSA	Electrochemical Surface Area
EDX	Energy-dispersive X-ray spectroscopy
EIS	Electrochemical impedance spectroscopy
HER	Hydrogen evolution reaction
ICDD	PDF International Centre for Diffraction Data - Powder Diffraction File
LSV	Linear sweep voltammetry
MEA	Membrane electrode assembly
OER	Oxygen evolution reaction
PEM	Proton Exchange Membrane
PEMWE	Proton exchange membrane water electrolysis
RDE	Rotating disk electrode
RHE	Reversible hydrogen electrode
SEM	Scanning electron microscopy.
SEM-EDX	Scanning electron microscopy-energy dispersive X-ray spectroscopy.
SOWE	Solid oxide water electrolysis
TEM	Transmission electron microscopy

TKK	TANAKA
UCT-EMI	University of Cape Town's Electron Microscope Unit
XRD	X-ray diffraction
XPS	X-ray photoelectron spectroscopy

Units of measurements

A	Amps (current unit)
$A.gIr^{-1}$	Amps per gram (current density unit)
°C	Degrees Celsius (temperature unit)
°C min^{-1}	Degrees Celsius per minute (temperature unit)
eV	Electron volt (energy unit)
hr	Hour (time unit)
kt	Kiloton (mass unit)
kV	Kilovolts (potential unit)
m^2g^{-1}	Meters square per gram (surface area unit of measurement)
Mt	Megaton (mass unit)
mg	Milligrams (mass unit)
ml	Millilitres (volume unit)
$mL.m^{-1}$	Millilitres per minute (rate unit)
nm	nanometre distance unit)
rpm	Rotations per minute (speed unit)
V	Volts (potential unit)

RESEARCH OUTPUTS

1. Publications

i. Ziyanda Jabe, Mangaka C. Matoetoe, Jessica Chamier. Oxygen evolution reaction catalysts synthesised from Ir metal: exploring pathways to increase catalyst surface area, stability and activity. *Journal of American Chemical Society*.

2. Conference presentations

i. Poster presentation at the 34th Annual Meeting of the Catalysis Society of South Africa (CATSA), Champagne Sports Resort, Central Drakensberg, South Africa. 03-06 November 2024.

Ziyanda Jabe, Mangaka C. Matoetoe, Jessica Chamier. Title: Chamier. Oxygen evolution reaction catalysts synthesised from Ir metal: exploring pathways to increase catalyst surface area, stability and activity.

Chapter 1: INTRODUCTION

Chapter One provides a brief explanation of the main idea behind the research, the problem statement, and its various objectives. It also underlines the current state of electrocatalyst commercialization and the challenges that the organization faces.

1.1 Problem statement

South Africa is known as the largest producer of industrialized iridium metal in the globe. Unfortunately, due to limited resources, most of the raw metallic iridium is exported for processing. This has prompted the development of new ways to improve the production process of iridium dioxide catalyst locally by improving South African mineral beneficiation. The produced catalyst should be able to compete with the standards of the commercial international benchmarks produced by suppliers such as Heraeus, Umicore, and Tanaka (TKK). Impala Platinum, a mining company, has provided Ir metal to Hydrogen South Africa (HySA), a research group focused on hydrogen catalysis. The goal was to produce an IrO_2 catalyst in-house as a substitute for purchasing it directly from suppliers. At HySA, the metal was oxidized through an alkali fusion reaction. This reaction is a decomposition process that involves exposing a noble metal to high temperatures. Previously, in-house Ir metal fusion electrocatalysts have been produced successfully. Unfortunately, they were not high performing in proton exchange membrane water electrolysis (PEMWE)-based processes due to their large particle size and low surface area. The goal of this study is to improve the current catalyst surface area by, optimizing the post-treatment conditions, adding support material, and using alloys or bimetallic. It is proposed that the resulting catalyst, be used by the HySA fuel cell or electrolyser group for further research.

1.2 Background

The world is expected to increase its energy consumption significantly over the next couple of years (Morello, 2021), which means there is a need to find new energy sources that are both clean and efficient. This is a daunting challenge that the world should tackle to avoid

environmental disasters. Various sustainable energy sources such as solar, wind, and hydrogen are needed to meet the increasing electricity demand (Ehteshami, 2014). Unfortunately, renewable energy sources are unpredictable and can be difficult to produce large-scale. Therefore, one of the most important factors that can be considered when it comes to addressing the energy crisis is the connection of energy storage systems with other production facilities (International Energy Agency, 2021).

One of the most promising technologies for producing green hydrogen is water electrolysis. This process involves separating water into oxygen and hydrogen. It can help cut down on greenhouse gas emissions. Unfortunately, the electrolyser's environmental impact is greatly affected by the source of the power it requires to operate (Khan, 2024). For instance, if the electricity used in water electrolysis comes from Eskom, the process's carbon footprint would remain significant, which undermines the notion of green hydrogen. The process requires electricity from renewable sources such as wind, solar, and hydropower to make water electrolysis more sustainable. Integrating this energy can help reduce the greenhouse gas emissions associated with the process. In South Africa, it is important to understand the source of electricity used in water electrolysis. This will help us evaluate its sustainability.

The Green Hydrogen Summit was held in Cape Town, South Africa, in October 2023. It discussed the country's capabilities as a producer of green hydrogen and how it can help reduce its reliance on fossil fuels. One of the key projects that the government is working on is the establishment of a green hydrogen hub in Boegoebaai. The summit highlighted the importance of green hydrogen in helping South Africa meet its emissions reduction goals. Various projects that are focused on the production of green hydrogen from renewable sources such as wind and solar were also discussed. The Boegoebaai Green Hydrogen Development Programme aims to develop a green hydrogen hub on the West Coast, targeting an initial 1.2 GW electrolyzer capacity by 2028, scaling up to 5 GW by 2035, and 10–20 GW by 2050 (GHCSSA, 2022).

One promising method of producing pure hydrogen is using proton exchange membrane water electrolysis (Amano, 2020). Water electrolysis is a process that involves the decomposition of water into hydrogen gas and oxygen using an electric current. It can be performed using a proton exchange membrane PEM-based cell. Water is supplied to a certain part of the cell, and it is separated from the other compartments by a membrane electrode assembly (MEA). The water is decomposed at the anode, resulting in the formation of molecular oxygen and hydrogen ions. This process is referred to as the Oxygen Evolution Reaction (OER). Protons migrate

through the membrane to the cathode. The electrons and protons are recombined at the cathode to form molecular hydrogen, and this reaction is called the Hydrogen Evolution Reaction (HER). The HER reaction has faster kinetics because it only involves the transfer of electrons and protons to form hydrogen. The OER has slow kinetics because it is a four-electron-proton coupled reaction, whereas the HER is a two-electron-transfer reaction (Wei, 2019). The challenging anodic OER process is due to the need for high reaction rates and the limitations of materials with sufficient stability and catalytic activity. An electrocatalyst is required to improve efficiency and facilitate charge transfer reactions in OER applications. The PEMWE technology platform employs electrocatalysts based on precious metal substrates to facilitate both anodic and cathodic processes, as illustrated in Figure 1.1 and further elaborated in Section 2.3. Iridium oxide is regarded as the most active and corrosion-resistant OER catalyst from the platinum group metals (PGMs), (Alia, 2016).

Although many countries are currently using PEMWE systems to fuel their hydrogen production facilities, the main cost drivers of these systems are the production of hydrogen instead of oxygen. This is why cost reduction strategies are often focused on lowering the production cost of hydrogen. For instance, the current cost of hydrogen production ranges from 700 to 1400 USD/kW, with a target to reduce it to 200 USD/kW by 2050 (Shiva et al., 2022). On the other hand, the cost of oxygen production is often overlooked. While the main cost drivers of PEMWE development are hydrogen production and oxygen production, addressing the challenges associated with the production of oxygen could lead to significant cost reduction and system efficiency improvements. This could involve the development of new OER catalysts, the use of support materials to improve surface area and durability, and the application of alternative cooling and bubble removal methods to enhance oxygen evolution efficiency. Therefore, it is important in water splitting catalysis to minimize the kinetic overpotential and reduce catalyst loading to reduce cost without affecting system efficiency (Hong 2016; Fabbri 2014; Wei 2019). The various approaches utilized to achieve high OER while reducing the iridium content have been studied, this concept will be explained in more detail in Chapter 2.

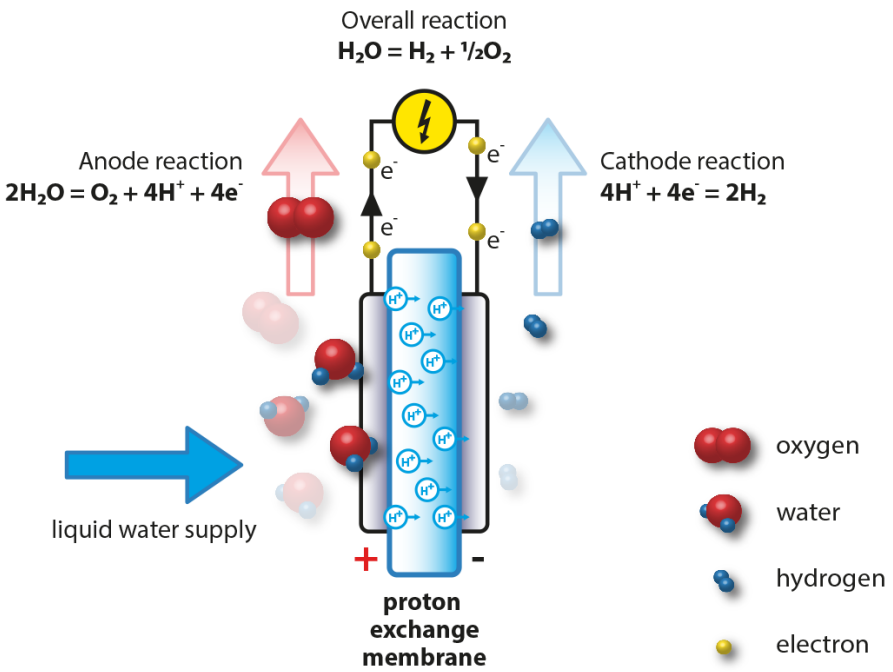

Figure 1-1: the proton membrane water electrolysis technology with their anode and cathode half-reaction (Hydron Energy., 2024).

1.3 Hypothesis and Assumptions

The surface area of a catalyst is directly correlated with the number of active sites for the reaction. A higher surface area allows for more sites to be utilized for the reaction, which increases the number of water molecules that can be oxidized and produces oxygen gas (Bernard et al., 2021). Factors such as morphology, structure, surface reactivity, and active site density can also affect a catalyst's OER performance (Poureshghi et al., 2023). According to Sangtam et al., 2023, the larger surface area helps improve the mass transfer of reactants and products. This also helps in the release of oxygen, which prevents bubbles from sticking to a catalyst's surface. The amount of energy required to drive a certain reaction at a certain rate is referred to as the overpotential. With higher surface areas, the ability to reduce this energy requirement can be achieved using catalysts.

The following hypotheses are proposed:

1. Increasing the iridium oxide (IrO_x) surface area will improve access to active sites on the surface and the overall activity of the catalyst. The concept of the surface area of a catalyst refers to its total physical dimension. On the other hand, the ECSA refers to the part of the surface that's actively involved in an electrochemical

reaction. Understanding these concepts is particularly important when it comes to designing and implementing catalysts for various applications in water electrolysis.

2. Employing of various synthesis techniques, such as post-treatment cooling can lead to smaller particles increasing the surface area of a catalyst. Amorphous or crystalline Ir-based materials may increase or decrease their surface area respectively enhancing their electrochemical activity and facilitating their accessibility to active sites (Oh et al., 2016).

3. Various substrates, such as metal oxides and carbon materials, can be utilized to provide support for IrO_x catalysts. These materials can increase the surface area where these reactions can be performed. In addition, they can help prevent the agglomeration and dissolution of IrOx particles (Islam, 2023).

1.4 Research Questions

1. How can the existing methodology of synthesising IrO_x be modified to increase the active surface area?
2. How will the surface area be influenced by adding it as either an alloy or supported onto a stable oxide material?
3. Will increasing the surface area of the catalyst increase its durability?
4. Can the required platinum group metals (PGM) content be reduced by supporting or alloying IrO_2 with Ta_2O_5?
5. How will post-treatment affect the surface area or particle size?

1.5 Aim and Objectives

Aim:

The aim of this project was to improve the surface area of the IrO_x synthesized from Ir metal, thereby improving its electrochemical activity.

The objectives that helped achieve the project goal include the following:

1. Optimising the Adam fusion conditions for Ir to IrO_x synthesis, considering different oxidising agents, post-treatments, and calcination conditions. Optimization should result in smaller particles and higher electrochemical activity.

2. Synthesis of IrO_x electrocatalysts by alloying with Ta_2O_5 and supporting IrO_2 onto Ta_2O_5. Determining the surface area, electrochemical performance, and durability.
3. Compare the physical and electrochemical properties of the produced Ir-based catalysts to the international benchmark.

1.6 Significance of the research

South Africa has the potential to become a significant producer of industrially significant minerals such as iridium dioxide by using the metallic iridium that is mined in the country. Through the beneficiation procedures, South Africa can increase its mineral exports, which can diversify the country's economy. Adam fusion is a process used in this study to synthesis iridium-based catalysts. It involves exposing noble metal to an oxidising material at high temperatures. This method for all in-house synthesis was modified from Lee, J 2011. A challenge with this method is that it produces iridium oxide with a low surface area and the main objective of the research is to increase the surface area of in-house iridium oxide-based nanomaterials. Different methods were evaluated to increase the surface area of iridium oxide by varying different oxidising agents, post-treatment cooling methods, and mixed-metal oxides. All the nanomaterials will be characterised using the analytical techniques mentioned above in section 2.5. The last chapter will focus on the findings and recommendations of this work.

1.7 Thesis outline

The study is comprised of six chapters.

Chapter 1: The chapter provides a brief explanation of the main idea behind the research, the problem statement and its various objectives. It also underlines the current state of electrocatalyst commercialisation and the challenges that the organization faces.

Chapter 2: Provides an overview of water electrolysis, focusing on the use of PEMWE and the Ir-based supported and unsupported OER electrocatalysts. Ways of increasing the surface area of IrO_2 and the

various analytical techniques used in the analysis of Ir-based nanomaterials.

Chapter 3: This chapter includes an introduction to the synthesis and characterization of iridium-based nanomaterials. It provides detailed synthesis methods involving various oxidizing agents, post-treatment cooling techniques, mixed-metal, and supported nanomaterials. The electrochemical protocols, ink formulations, and data collection methods are also described in detail.

Chapter 4: This chapter presents the data interpretation and discussion of the synthesis of unsupported iridium oxide nanomaterials using two different oxidizing agents, three cooling post-treatment methods, mixed-metal composition, and support material. The properties of the IrO_x nanoparticles were evaluated through spectroscopic characterization techniques. The discussion of the data and spectral analysis is compared to relevant literature for validation and insight. It will emphasize how different oxidizing agents, cooling post-treatments, mixed-metal systems, and material supports influence the elemental composition, structure, surface area, and oxidation states of the synthesized materials.

Chapter 5: The chapter discusses all the electrochemical studies for the OER performance of the IrO_x electrocatalysts. In addition to the information collected from the iridium-based nanomaterial's physiochemical properties, to gain a deeper understanding of how these properties affect the electrocatalysts' electrochemical performance.

Chapter 6: Conclusions and recommendations for enhancing the surface area of in-house iridium oxide for use as an oxygen evolution reaction catalyst.

1.8 References

Amano, F., Furusho, Y., & Hwang, Y. M. (2020). Amorphous Iridium and Tantalum Oxide Layers Coated on Titanium Felt for Electrocatalytic Oxygen Evolution Reaction. *ACS Applied Energy Materials,* 3(5), 4531–4538. https://doi.org/10.1021/acsaem.0c00208.

Alia, S. M., Rasimick, B., Ngo, C., Neyerlin, K. C., Kocha, S. S., Pylypenko, S., Xu, H., & Pivovar, B. S. (2016). Activity and Durability of Iridium Nanoparticles in the Oxygen Evolution Reaction. *Journal of The Electrochemical Society*, *163*(11), F3105–F3112. https://doi.org/10.1149/2.0151611jes.

Bernard, P., Stelmachowski, P., Broś, P., Makowski, W., & Kotarba, A. (2021). Demonstration of the Influence of Specific Surface Area on Reaction Rate in Heterogeneous Catalysis. *Journal of Chemical Education*, *98*(3), 935–940. https://doi.org/10.1021/acs.jchemed.0c01101.

Ehteshami, S. M. M., & Chan, S. H. (2014). The role of hydrogen and fuel cells to store renewable energy in the future energy network - potentials and challenges. *Energy Policy*, *73*, 103–109. https://doi.org/10.1016/j.enpol.2014.04.046.

Fabbri, E., Habereder, A., Waltar, K., Kötz, R., & Schmidt, T. J. (2014). Developments and perspectives of oxide-based catalysts for the oxygen evolution reaction. In *Catalysis Science and Technology* (Vol. 4, Issue 11, pp. 3800–3821). Royal Society of Chemistry. https://doi.org/10.1039/c4cy00669k.

Green Hydrogen Commercialising Strategy For South Africa (GHCSSA). (2022). Full-Report-Green-Hydrogen-Commercialisation-Strategy.https://www.thedtic.gov.za/wp-content/uploads/Full-Report-Green-Hydrogen-Commercialisation-Strategy.pdf.

Hong, B. K., Mandal, P., Oh, J. G., & Litster, S. (2016). On the impact of water activity on reversal tolerant fuel cell anode performance and durability. *Journal of Power Sources*, *328*, 280–288. https://doi.org/10.1016/j.jpowsour.2016.07.002.

International Energy Agency. (2021). Review 2021 Assessing the effects of economic recoveries on global energy demand and CO_2 emissions in 2021 Global Energy. Available at: https://www.iea.org/reports/global-energy-review-2021. (Accessed: 20 January 2023).

Islam, J., Kim, S. K., Rahman, M. M., Thien, P. T., Kim, M. J., Cho, H. S., Lee, C., Lee, J. H., & Lee, S. (2023). The effect of iridium content in boron carbide-supported iridium catalyst on

the activity and stability of proton exchange membrane water electrolyzer. *Materials Today Energy*, *32*. https://doi.org/10.1016/j.mtener.2022.101237.

Khan, M. H. A., Sitaraman, T., Haque, N., Leslie, G., Saydam, S., Daiyan, R., Amal, R., & Kara, S. (2024). Strategies for life cycle impact reduction of green hydrogen production – Influence of electrolyser value chain design. *International Journal of Hydrogen Energy*, *62*, 769–782. https://doi.org/10.1016/j.ijhydene.2024.01.081.

Lee, J., & Kim, Y. (2011). Chemical dissolution of iridium powder using alkali fusion followed by high-temperature leaching. *Materials Transactions*, *52*(11), 2067–2070. https://doi.org/10.2320/matertrans.M2011202.

Morello., S. (2021). WWF. Effects of Climate Change. Available at: https://www.worldwildlife.org/threats/effects-of-climate-change. (Accessed: 10 January 2022).

Poureshghi, F., Seland, F., Jensen, J. O., Heath, M. M., & Sunde, S. (2023). Exploring the influence of composition and morphology on the oxygen evolution reaction performance of Co-based catalysts. *Journal of Alloys and Compounds*, *967*. https://doi.org/10.1016/j.jallcom.2023.171627.

Shiva Kumar, S., & Lim, H. (2022). An overview of water electrolysis technologies for green hydrogen production. In *Energy Reports* (Vol. 8, pp. 13793–13813). Elsevier Ltd. https://doi.org/10.1016/j.egyr.2022.10.127.

Wei, C., Rao, R. R., Peng, J., Huang, B., Stephens, I. E. L., Risch, M., Xu, Z. J., & Shao-Horn, Y. (2019). Recommended Practices and Benchmark Activity for Hydrogen and Oxygen Electrocatalysis in Water Splitting and Fuel Cells. In *Advanced Materials* (Vol. 31, Issue 31). Wiley-VCH Verlag. https://doi.org/10.1002/adma.201806296.

Chapter 2: LITERATURE REVIEW

This chapter reviews relevant literature related to iridium oxide as an oxygen evolution reaction catalyst and the need to increase its surface area. It also provides a more in-depth description of its applications in different industries such as proton exchange membrane water electrolysis and the challenges that confront the technology's development. Furthermore, various analytical techniques used in the analysis of iridium oxide are reviewed and the significance of the research is highlighted.

2.1 Introduction

Iridium is one of the platinum group metals known for its rarity as well as remarkable chemical, and physical properties. Combined with oxygen, IrO_x forms various structures, stoichiometries and oxidation states. The structure and oxidation state of iridium oxide can influence its colour as it exhibits varying shades of blue, black, and brown (Scarpelli et al., 2022). The most common kind is iridium (IV) dioxide (IrO_2), which is in the Ir^{4+} oxidation state (Park et al., 2023). It has a widespread application in electrochemical processes with a substantial potential for future development due to its unique and attractive properties. It exhibits useful characteristics, such as high conductivity, catalytic activity, and stability (Quinson et al., 2022). Iridium oxide thermal stability allows it to endure harsh operating conditions, such as high temperatures, highly acidic or alkaline conditions and corrosive environments. This material can be particularly beneficial in certain types of energy conversion equipment, such as steam generators and gas turbines (Tatrari et al., 2024). Iridium oxide is commonly used as a catalyst in various processes, such as the oxidation of oxygen. Its exceptional catalytic activity makes it an indispensable component in water-splitting devices, which convert water into hydrogen and oxygen using this chemical. More applications are presented in Table 2.1 below.

Table 2-1: *Applications of iridium oxide in various fields.*

Sector	Application	References
Electrochemical Applications	Enhance the performance and durability of the electrodes	Clapp et al., 2023
Water Electrolysis	Anode electrode in PEMWE	Abbott et al., 2016
Electrochemical Sensors	Detection of gases, particularly oxygen	Dong et al., 2021
Biomedical Applications	Medical devices, such as neural stimulation electrodes	Sun et al., 2023
Environmental Monitoring	pH electrodes in water quality monitoring and physiological analysis	Zhou et al., 2020
Fuel Cells	High electrical conductivity - oxygen-water conversion process	Hoffman et al., 2023
Metal-Air Batteries	Catalyst to improve the OER's kinetics to improve battery performance	Cheng et al., 2021
Photoelectrochemical Cells	Solar energy into chemical fuels	Klyuev et al., 2019

2.2 The challenge of rare iridium for OER

Iridium is a rare element of which the refining, and extraction processes are expensive and complex (Filho et al., 2023). According to a report by the European Commission's Ad-hoc working group on defining critical materials, iridium is one of the most critical raw materials in the Pt-metal group (Sawy et al., 2017). Due to the scarcity of mining sites and the location of the mines, it is very risky to secure a steady supply of iridium. Most of the time, it occurs in the form of sulphide or alloyed with copper, nickel, or osmium (Wei et al., 2024). There are only a few iridium-rich sites in Canada, Russia, and South Africa. Due to the development of

high-temperature crucibles that can be used to produce single-crystal semiconductors, the demand for this material has increased (Filho et al., 2023).

As the demand for IrO_2 continues to rise, optimising its utilisation becomes more important to ensure technological and sustainable growth. The scarcity and price of iridium highlight the importance of utilising IrO_2 efficiently. The optimisation of the iridium loading required to drive the efficient operation of PEM-electrolysis catalysts is a critical component of the development of industrial-scale OER technologies. Currently, the anodic loadings of Ir-coated products are around 2 $mg_{Ir}.cm^{-2}$. This is a significant concern for the various projects that are focused on PEM-based electrolysis. The projected shortage and high cost of iridium have prompted the need for a reduction in the Ir-loads (Han et al., 2023).

2.3 Water electrolysis and the oxygen evolution reaction

Various methods to produce hydrogen are water electrolysis, coal gasification, and steam methane reforming. The latter is used, and according to data released by the IEA in 2021, it has resulted in the release of high greenhouse gases compared to water electrolysis which highly requires an energy-consuming process. Water electrolysis is the most advanced technology that can produce green hydrogen at the scale needed to achieve climate neutrality (IEA, 2022). Currently, there are three diverse types of water electrolysis systems being used: solid oxide water electrolysis (SOWE), PEMWE, and alkaline electrolysis (AWE) presented in Figure 2.1 with their half-reactions. The latter is made using inexpensive and readily available materials. They can function efficiently even though they have certain impurities, like sulphur and carbon dioxide. In addition, it can produce substantial amounts of hydrogen, which is ideal for commercial industry. However, it is more prone to corrosion than a Proton Exchange Membrane (PEM) model. This makes it more costly to maintain and its temperature range can limit its responsiveness to high temperatures. (Gambou et al., 2022). Solid oxide electrolysis is a type of high-temperature process that can be utilized in certain applications, such as in chemical plants. These electrolysers have better efficiency than PEMWE or alkaline electrolysers, and they can potentially convert carbon dioxide and water into various useful products. However, their high operating temperature can pose challenges in terms of their durability and materials. According to numerous studies, PEM water electrolysis is the most viable method due to its exceptional efficiency, quick response times, and low operating temperatures. Proton exchange membrane electrolysers are frequently utilised in diverse applications to produce hydrogen (Nady et al., 2022). Some of their disadvantages include the

PEM's limitations. For instance, thin membranes cannot tolerate high pressures, and increasing their thickness can result in lower conductivity (Bonanno et al., 2024).

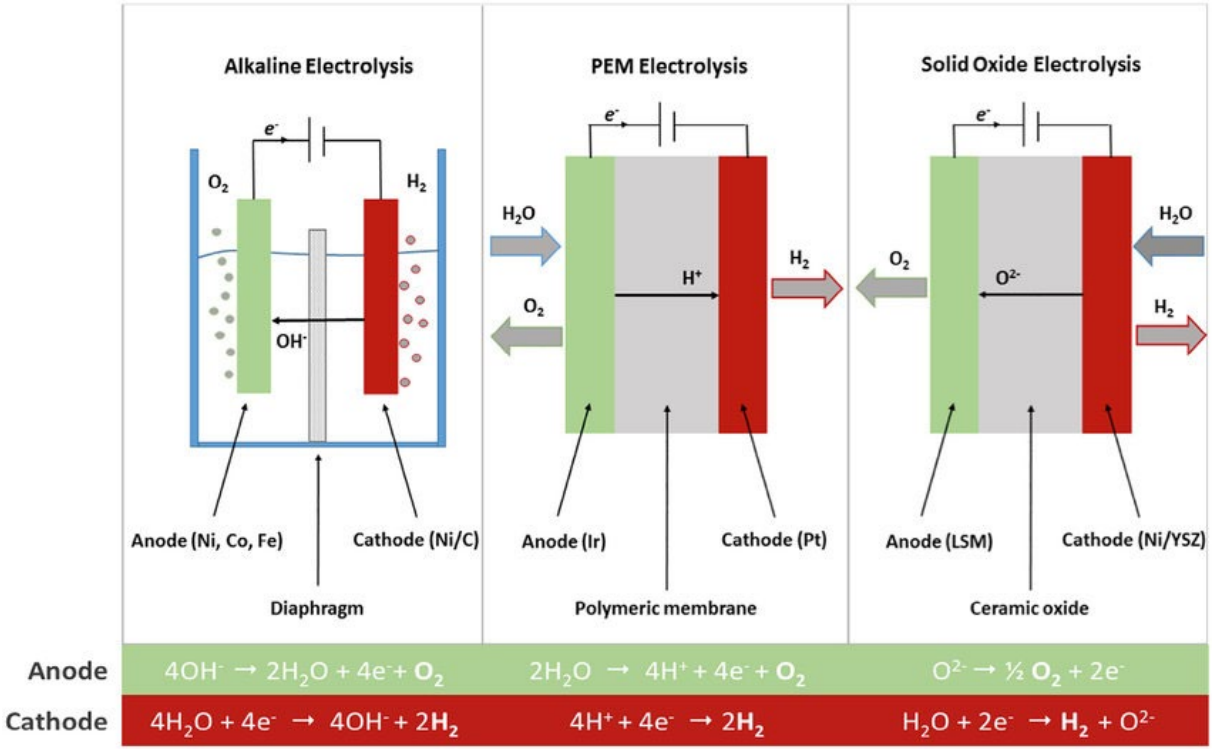

Figure 2-1: The three main water electrolysis technologies are alkaline water electrolysis, proton exchange membrane, and solid oxide electrolysis with their anode and cathode half-reaction (Sapountzi et al., 2017).

This study focuses on the application of oxygen evolution reaction in the PEMWE. It is a water electrolysis device that converts water into oxygen and hydrogen using an electrochemical process. One of the advantages of PEMWE is its ability to produce high-purity hydrogen gas, as the proton exchange membrane prevents any mixing of gases (Shiva et al., 2019). As seen in Figure 2.1 above, it uses a PEM which selectively blocks electrons while allowing protons to pass through. When water is exposed to an electric current through the PEMWE system, it decomposes at the anode, resulting in the formation of molecular oxygen and hydrogen ions. The protons then travel through the membrane to the cathode, which reduces them to hydrogen gas. The overall reaction for the two half reactions shown in Figure 2.1 under the PEM electrolyser column is shown below.

$$2H_2O \rightarrow 2H_2 + O_2 \qquad E°=1.23\ V \qquad (2.1)$$

The goal of the research efforts is to develop affordable Ir-based OER catalysts that can be used for PEM-electrolysis. The reduction of the anode's precious metal loadings is the most important goal to make this technology economically feasible. The OER plays a vital role in various water electrolysis technologies that are focused on producing hydrogen energy. This process is regarded as an efficient and environmentally friendly way to produce hydrogen. Researchers are working to improve the efficiency of these processes by developing new catalysts and materials. However, the adsorption scaling energy between the different reaction intermediates has a significant negative impact on the reaction kinetics of OER catalysts and can lead to significant overpotential and sluggishness. The critical factors to consider in the design of high-efficiency and novel catalysts are the relationship between the catalytic activities, and the electronic and structural properties of the compound.

2.4 Oxygen evolution reaction electrocatalysts

The choice of the right catalyst for oxygen evolution reaction applications is influenced by numerous factors, such as its cost, activity, stability, and availability (Quinson et al., 2022). An electrocatalyst for the OER should be highly conductive, operate at high power densities, and have a wide range of electrolyte compositions. It should be made from earth-friendly materials, and it should undergo low-cost preparation and manufacturing (Filho et al., 2023).

The surface area of an OER electrocatalyst is very important to improve its stability, performance, charge transfer and electronic structure optimization. By increasing surface area using nanostructured or porous materials, it is possible to enhance the overall electrochemical performance of the catalysts. In addition to optimizing the surface area, it's also important to consider the stability of the OER electrocatalyst to ensure its long-term durability. This component’s development contributes to the advancement of more robust and efficient electrocatalysts, which are vital for water electrolysis and the promotion of green hydrogen. Table 2.2 below shows the relationship between the surface area and the different factors that affect the OER’s performance.

Table 2-2: *Four critical factors influencing OER electrocatalysts and surface area.*

Factors	Impact on OER Performance	Surface Area Relation	References
High Catalytic Activity	Boost reaction rate by increasing active sites.	Greater surface area exposes more sites for OER reactions.	Zhao et al., 2021; Khan et al., 2023
Good Stability	Prevents degradation over time in harsh conditions.	Distributes reaction load, reducing the risk of localised catalyst breakdown.	Clapp et al., 2023
Enhanced Charge Transfer	Facilitates efficient electron and ion movement.	Increases contact points between catalyst particles and electrode surface.	Yao et al., 2024
Electronic Structure	Influences adsorption/desorption of reaction intermediates.	Alters surface atom properties to improve interaction with oxygen species.	Wang et al, 2021; van der Merwe et al., 2023

One of the most crucial factors that can be considered when it comes to the design and performance is its corrosion resistance (Clapp et., al 2023). This ensures that the operation of the electrode will continue for a long time without requiring replacement or maintenance. The overpotential for the OER is shown in equation 2.1 and it refers to how much additional voltage is required to catalyse a reaction compared to the thermodynamic equilibrium potential (Wang et al., 2020). Various factors, such as the energy requirements of the activation process and the concentration gradients, can cause the overpotential of an electrochemical cell. The OER is initiated by breaking the bonds in water molecules. On the other hand, concentration gradients can limit the mass transport of water (Heiranian et al., 2023). The overpotential of devices that

utilise the OER can significantly affect their efficiency and performance. Some of these include water electrolysers and fuel cells.

Due to their electronic properties and crystal structures, various types of Perovskite oxides (Wong et al., 2021), such as strontium ruthenate ($SrRuO_3$) and lanthanum cobaltite ($LaCoO_3$), have been identified as potential catalysts for the OER (Chen et al., 2020). Currently, researchers are focused on developing effective strategies to optimize the performance of these materials. Although perovskite oxides exhibited promising results in laboratory tests, their commercialization remains in its early stages. Various challenges need to be resolved such as scalability, stability, and cost (Khatoon et al., 2023). The most studied OER catalysts include those involving transition metals such as manganese oxide (Radinger et al., 2021), and cobalt oxide (Burke et al., 2015). These catalysts are effective for alkaline conditions they are known for their abundant and relatively low cost but not good catalysts for OER in acidic conditions.

Various metal heterostructures and alloys, such as those containing NiFe (Lim et al., 2020), doped metal oxides (Hoffman et al., 2023; Rajan et al., 2020), hybrid structures (Mathew et al., 2021), and metal oxide composites, have the potential to be effective OER catalysts due to their synergistic effects. Currently, researchers are focused on developing novel architectures that can enhance stability and activity (Mahfoudh et al., 2023). The commercialisation of OER catalysts made from metal alloys is still in its early stages (Bojovic et al., 2022). Combining noble metals can enhance promising performance in the laboratory but their commercial potential is constrained by factors such as high cost, insufficient raw materials, scaling issues, and limitations on production (Karthikeyan et al., 2018).

2.5 Iridium oxide as an oxygen evolution reaction catalyst

This study will focus on one of the most widely used oxygen evolution reaction catalysts iridium oxide. Extensive studies have been conducted on this type of catalyst to gain a deeper understanding of its various characteristics (Felix et al., 2012; Malinovic et al., 2023 & Banti et al., 2023). Among the many noteworthy characteristics of iridium oxide is its catalytic activity, especially towards the OER. Iridium oxide can reduce the required overpotential significantly, enabling the OER at lower applied voltages (Naito et al., 2021).

Figure 2.2 compares the overpotential (η) with the standard heat of formation, and the overpotential is defined as the potential required to achieve a given current density. In the

volcano plot below, RuO_x is the most active catalyst followed by IrO_x but it's unstable and quickly dissolves in acidic solutions. Studies have shown that the dissolution rate of Ru-based catalysts is significantly higher than that of other OER materials (Danilovic et al., 2014; Qu et al., 2021). This suggests that the onset of the catalysts' corrosion potential is related to the Ru's metal composition (Wei et al., 2019). Similar degradation issues can be encountered with Ir-based catalysts (Alia et al, 2016). During the long-term catalytic process, the rutile oxide of IrO_x will transition to other phases that are soluble in acid media (Badam et al., 2018). Although IrO_x is a good catalyst for the operation of the OER, it is expensive and prone to agglomeration, which can significantly reduce its efficiency. Researchers are working on finding ways to address these challenges using catalysts that are both low in precious metals and non-toxic.

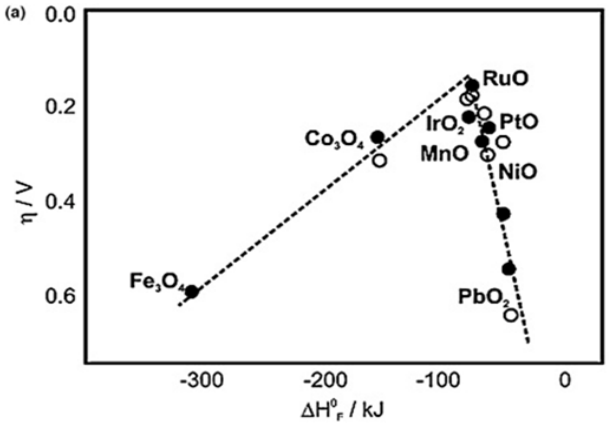

Figure 2-2: Demonstrations of the volcano plot of the OER catalysts (Badam et al., 2018).

Ruthenium oxide (RuO_x) and iridium oxide are commonly used as benchmarks for OER electrocatalysts (Suen et al., 2017; Kim et, al., 2017; Baik et al., 2020; Ma 2023, & Daiane et al., 2021). Through theoretical studies, a method has been developed to predict the activity of an OER reaction using universal descriptors for different electrocatalytic substances. The studies were conducted using the density functional theory (DFT) method, which is focused on determining the overall reaction overpotential. Studies on the free energies of noble metal surfaces revealed that the affinity of the OER-catalysed reactions toward the same surface is linked to the reaction's binding energies (García-Mota et al., 2012; Rossmeisl et al., 2005). These are independent of the specific mechanism, and the scale of these reactions binding energies is proportional to each other. According to the study, the free energy diagrams of the OER can be used to analyse the various steps in the reaction process. The authors proposed a descriptor that describes the difference between the adsorption energy of the bound O* and

HO*. This allows for the creation of volcano-shaped curves and the OER overpotential can be plotted against the standard to visualise the activity of a catalyst (Higareda et al., 2023; Fabbri et al., 2018).

Iridium oxide catalysts are frequently utilised in diverse industrial processes as mentioned in Table 2.1. Various companies supply IrO_2-based catalysts, which are commonly used in various industrial processes, such as water electrolysis and corrosion protection. Its commercial availability makes it a viable choice for researchers and industrial engineers who are looking for dependable OER catalysts. South Africa is regarded as the largest producer of iridium metal in the world. This study aims to develop a durable and high-performing high-surface area iridium oxide from metallic iridium supplied by a local mine. Producing IrO_x using iridium metal in South Africa will offer numerous advantages, such as technological progress, environmental sustainability, and economic growth. The nation can also claim to be a leader in the global market for such technologies and materials by leveraging its natural resources and manufacturing processes.

2.6 Synthesis of Iridium oxide

The specific synthesis technique used to make iridium oxide can have an impact on its properties. The synthesis methodology controls the crystal structure, particle size, and morphology of the material, as well as the catalyst's performance. Choosing a synthesis method that fits the requirements of the given application is especially important. The synthesis conditions, including the temperature, pressure, and concentration of precursor gases, should be carefully adjusted to enhance the surface area of the IrO_x catalyst. The synthesis of iridium oxide can be produced through various methods such as the chemical method (Bhattacharyya et al., 2021), sol-gel processes (Sztaberek et al., 2019), poly method (Malinovic et al., 2023; Oh et al., 2016), and microwave-assisted hydrothermal deposition (Gawande et al., 2014; Salvatore et al., 2021; Massué et.al., 2017). A general synthesis overview process involves Ir-based precursors such as iridium chloride ($IrCl_3$), Chazapis et al., 2023 & Zaman et al., 2018), hydrogen hexachloroiridate (IV) hydrate (H_2IrCl_6 x H_2O) (Scarpelli et al., 2022; Patel et al., 2015), iridium (III)-acetylacetonate $Ir(acac)_3$ or ammonium hexachloroiridate ($[NH_4]_2IrCl_6$, Jia et al., 2021; Ye et al., 2011). The most common method is the thermal decomposition (Banti et al., 2023; Musić et al., 2019) of an iridium salt precursor. A typical example of the synthesise procedure involves a solution containing an iridium precursor that is usually dissolved in water

or alcohol. To control its morphology and particle size, a stabilising agent, such as polyvinylpyrrolidone (PVP) or surfactants, is added. The dry reagents or precursor solution is heated to a certain temperature, which then causes the compound to decompose. Thereafter, the nanoparticles are washed several times to remove impurities, then dried and the resulting suitable IrO_x product is then used in various applications.

The Adams fusion technique is mostly used to prepare catalysts for various types of metals, such as iridium and ruthenium oxides. It is regarded as a simple yet effective method for producing high-quality metal oxides with excellent catalytic characteristics. In addition, it can be used to prepare mixed metal oxides to ensure a high degree of uniformity (Felix et al., 2019, Lui et al., 2018 & Verner et al., 2023).

2.7 Increasing the surface area of a catalyst

A catalyst's catalytic activity can be enhanced by increasing its surface area. A higher surface area allows for more active sites, resulting in better reaction efficiency (Zhao et al., 2021). Here are various general approaches that can be used to enhance the surface area of catalysts. Abbott conducted a study using the Adam fusion method to increase the surface area of a catalyst. In this study, they reviewed the correlation between particle size and morphology. The results indicated that the synthesised iridium oxide had the highest particle size 1.7 ± 0.4 nm and a specific surface area of 150 $m^2 g^{-1}$ showed the highest OER activity. The researchers noted that the OER activity increased with the decrease in particle size. In addition, it was observed that, although the capacitance of the surface charge is linearly correlated with the Brunauer Emmett and Teller (BET) surface area, it does not match that of the OER activity.

One of the ways of increasing the surface area is by reducing the particle size. The size can be reduced by using ball milling. Costa de Oliveira et al., 2020, conducted a study on the effects of ball milling on the surface area and activity of Fe-N-C catalysts. They found that increasing the milling time by three hours significantly increased the surface area of the catalysts, but this effect could be reversed by the longer duration of the process. As seen in Figure 2.3, mechanical grinding breaks down bigger particles into smaller ones, which increases the surface area (Ajayi, E. 2019).

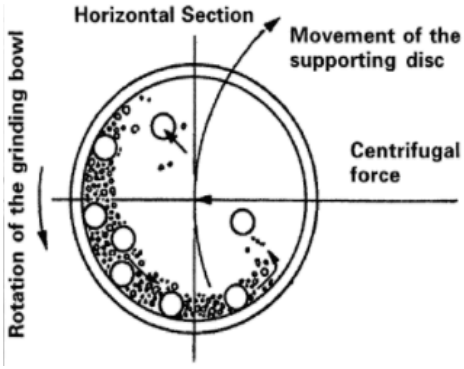

Figure 2-3: High energy planetary grinding action of planetary mills (Ajayi, 2019).

Another approach to increasing surface area is the use of mesoporous or microporous materials, which form catalysts with a well-defined network of interconnected pores, enhancing accessibility to active sites. These materials can be created by a process called templating, which involves discarding a template after the synthesis. In 2020, Baik, Pak, Lee, and S.W. stated that the presence of macropores in catalysts can improve the reaction's performance. Compared to catalysts without these features, those with many macropores exhibited better OER stability and activity. The presence of macropores allows for faster mass transport during a reaction, which can help regenerate active sites and facilitate bubble detachment.

In this study, the Adam fusion method was optimised and modified to enhance the catalyst's surface area and performance. These modifications involved using different oxidising agents, post-treatment processes using cooling rates, and supporting the catalyst on various substrates. The use of different oxidising agents can affect the oxidation state, porosity, surface area and morphology of the catalyst. The phase and crystallinity of metal oxides can be affected by controlled cooling rates. For instance, rapid quenching can lead to the formation of metastable or amorphous phases. On the other hand, slow cooling allows for the establishment of more stable and crystalline forms. Supporting a catalyst on a substrate can enhance its surface area and improve its catalytic activity. Commonly supported materials include carbon, graphene, and titanium dioxide. Its stability and electronic properties can also be affected by the choice of support.

2.8 Physical characterisation of oxygen evolution reaction electrocatalysts

Understanding the various properties of iridium oxide is especially important to develop effective and efficient catalyst. Different analytical techniques shown in Figure 2.4, were used to confirm the physical, and chemical properties of synthesised and commercial IrO_x-based materials. In confirmation of structural characterisation, different techniques were used such

as an X-ray diffraction (XRD) which study can be performed to determine the phase composition and crystal structure of IrO_x that has been synthesised. The information provided by transmission electron microscopy (TEM) is focused on the particle size, crystallinity, and morphology of the catalysts produced. Scanning Electron Microscopy (SEM) was used to study the morphology, and the elemental composition of a synthesised substance was assessed using Energy-dispersive X-ray spectroscopy (EDX). The information collected by the X-ray Photoelectron Spectroscopy (XPS) was used to study the oxidation state of the catalysts.

2.9 Electrochemical characterisation of oxygen evolution reaction electrocatalysts

The cyclic voltammetry (CV) was used to analyse the IrO_x's electrochemical behaviour, including its role in the oxygen evolution reaction. A linear sweep voltammetry (LSV) technique was used to measure the potential sweep of an electrode while it was working. The resulting current can be either a positive or negative-going potential and the information collected by the procedure identifies the catalyst's electrochemical behaviour. The technique of chronoamperometry (CA) involves keeping a constant potential on an electrode while also measuring its current. This allowed one to study the various reactions taking place at the surface of the electrode (Abbott et al., 2018; Alia et al., 2016; Higareda et al., 2023; Naito et al., 2021).

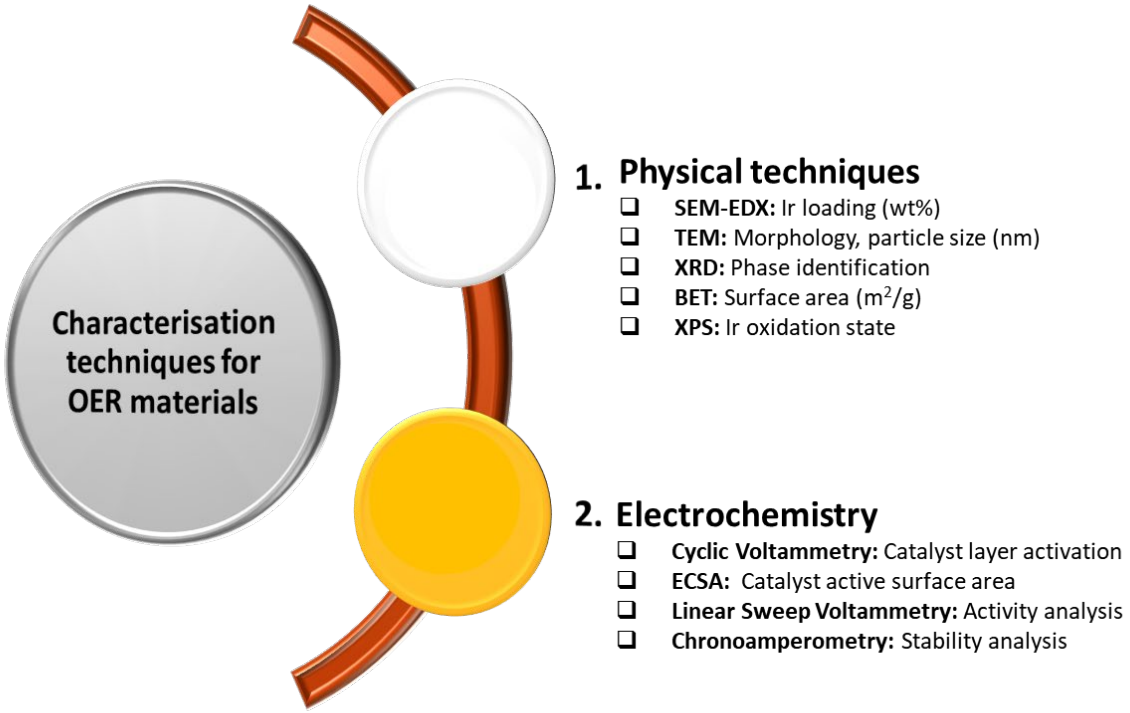

Figure 2-4: Characterisation techniques for the oxygen evolution reaction materials.

2.10 Optimization of influential parameters for OER electrocatalysts

Several key parameters must be optimized to make electrocatalysts for oxygen evolution reaction more effective and are listed in Table 2.3 below. This is significant to improve the stability and catalytic efficiency of these materials.

Table 2-3: *Summary of the optimization of influential parameters for OER electrocatalysts*

Parameter	Optimization	Effect on OER
Catalyst Loading	Optimize the amount of catalyst loaded on the electrode.	Balances active site availability and avoids excessive catalyst mass, improving efficiency and performance.
Rotating Speed	Adjust electrode rotation speed to improve mass transport and bubble removal.	Enhances reactant/product transport, reduces bubble interference, and increases effective current density.
Electrolyte Concentration	Optimize ionic conductivity and pH of the electrolyte.	Affects OER efficiency; higher concentrations improve conductivity, while maintaining optimal pH prevents side reactions.
Catalyst Composition and Morphology	Optimize the material, structure, and surface area of the catalyst.	Enhances active site exposure, improving catalytic activity and stability.
Cell Design and Geometry	Adjust electrode spacing and surface area for optimal electric field distribution and mass transport.	Ensures efficient electrode interaction and reduces energy loss during the OER process.

2.11 Determining the activity catalyst towards the oxygen evolution reaction

The activity of an oxygen evolution reaction catalyst is the measure of the amount of O_2 which can be produced, with the lowest required overpotential. The amount of O_2 produced is measured as a maximum resulting current, for a given potential. The most common method for reporting catalytic activity is to calculate the mass or specific activity. Rajan et al., 2020, conducted a protocol standard procedure where the mass activity is the standardisation of the current for the mass of the catalyst on the electrode, whereas the specific activity is the standardisation of the current for the surface area of IrO_2.

The activity of a catalyst is then typically compared by calculating the current density at 1.525-1.55V vs Reversible Hydrogen Electrode (RHE). The overpotential for oxygen evolution is the extra voltage beyond the theoretical 1.23V needed to overcome kinetic barriers, such as breaking O-H bonds and facilitating electron transfer. Voltages of 1.525-1.55V are used to evaluate electrocatalyst performance, as this range provides reliable current density measurements. Below this range, the reaction may be too slow for accurate assessment. Operating within this voltage range also minimizes slow or irregular oxygen bubble formation, ensuring stable and accurate measurements without interference.

While activity is a measure of the current generated when an overpotential is applied, durability is related to the amount of time the catalyst is used before dissolution occurs (Wei 2019). The OER currents are converted to Ir mass-specific activity by normalisation to the mass of iridium present on the Rotational Disc Electrode (RHE) for technically relevant comparison. This is determined using the Ir weight percentage (wt%) obtained from the dispersive X-ray spectroscopy (EDS) analysis. To determine the relative loss of mass activity, the catalyst is exposed to activation steps using chronoamperometry from 1.5 - 1.560V vs. RHE in 20 mV steps, for a period of 1 minute per step before and after the durability test. These before and after activation steps are used to plot Tafel slopes which can estimate the durability of the catalyst (Rajan et al., 2020). The Tafel slopes are important in electrochemistry, especially in the study of catalytic reactions. They play a vital role in understanding how these reactions work. They are derived from the Tafel equation, which relates the overpotential (η) to the logarithm of the current density (j), a is a constant, and b is the Tafel slope.

$$\eta = a + b\log(j) \tag{2.3}$$

It is important to optimise the electrochemical surface area (ECSA) of Iridium oxide to achieve better results in electrochemical processes. The ECSA refers to the catalyst surface area available for the OER. Unlike with oxygen reduction reaction catalysts like Pt, it is more complicated to determine the ECSA of IrO_2-based catalysts as they are not active for proton adsorption/desorption nor CO_2 poisoning (Jackson et.al., 2017; Nagai et.al., 2019). According to Vincent et al., 2016, Labi et al., 2019, McCrory et al.,2013, and Zhao et al., 2015, the OER catalyst ECSA estimation is calculated by considering the double-layer electrochemical capacitances of different materials and it is then normalised with the Ir loading the catalyst. However, different ECSA methods were conducted by Duran et al., 2021 and Felix et al.,2019. According to Biesheuvel and Dykstra in 2018, the non-Faradaic potential refers to the region responsible for storing charge on a catalyst's surface. In this work, the ECSA of the electrocatalysts were estimated using the double-layer capacitance of the catalysts. The linear slope of the current vs scan rate, which is equivalent to twice the double-layer capacity (Cdl), was then used as the ECSA's representation. A typical representation of the OER activity in literature is provided below in Figures 2.5 and 2.6. In literature, Alia et al., 2016, investigated the activity and durability of various Ir/IrO_2 catalysts before and after 13.5 hours of 1.6V hold and discovered that the mass activity at 1.55 V vs. RHE for IrO_2 before the potential hold was 140 $A.g^{-1}$ Ir but dropped by 54% to 90 $A.g^{-1}$ Ir after the potential hold. This study will use the same procedure as shown in Figure 2.5, to estimate the performance of each catalyst.

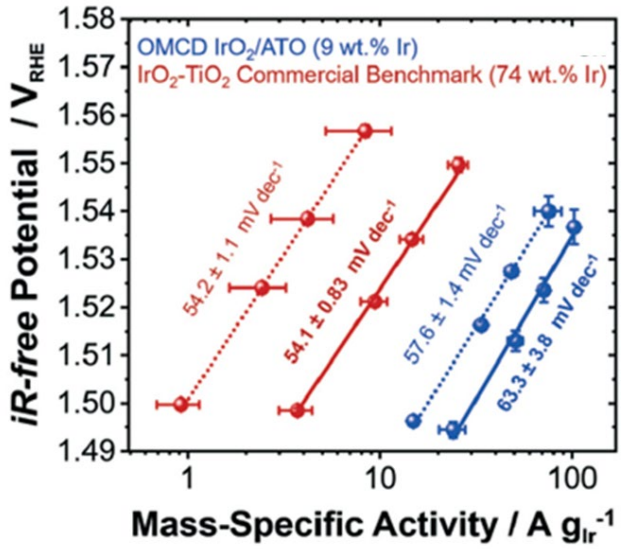

***Figure 2-5**:* **An example of the OER activity represented in literature by Rajan et al., 2020.**

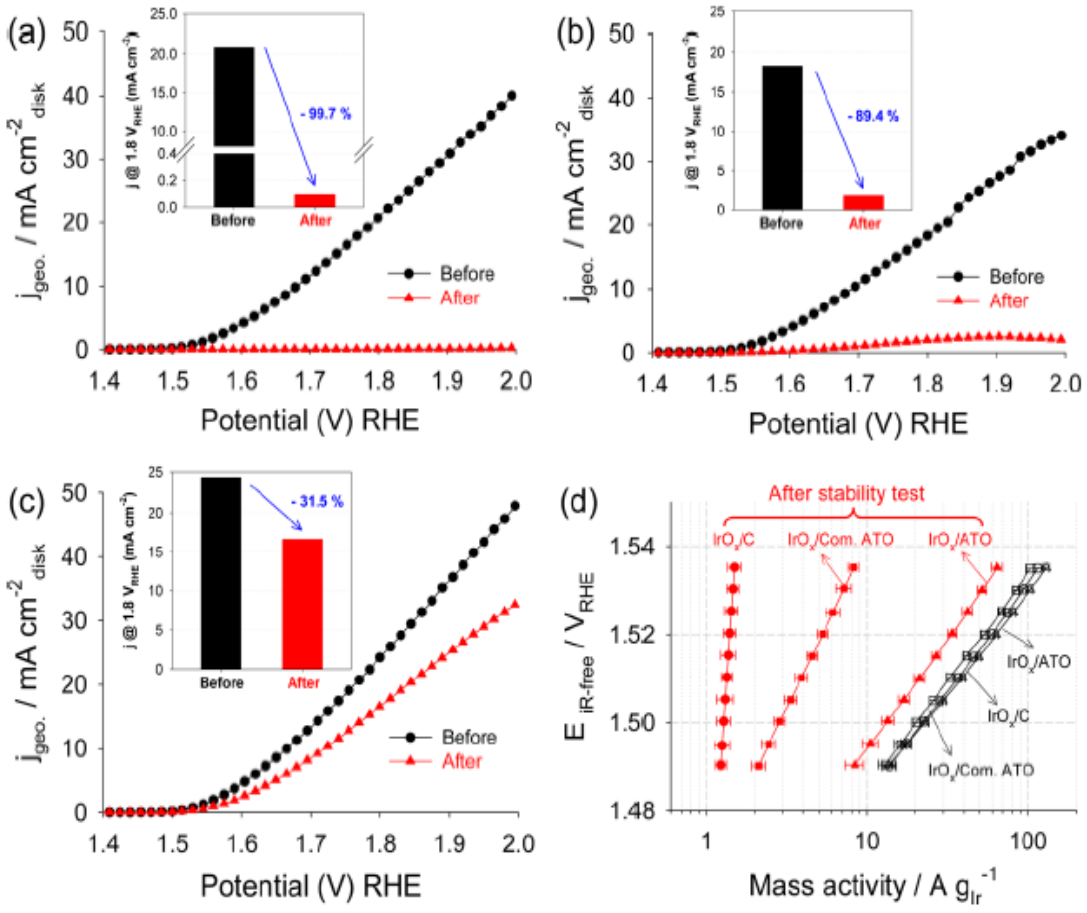

Figure 2-6: An example of the OER activity represented in literature by Oh et al., 2018.

2.12 References

Abbott, D. F., Lebedev, D., Waltar, K., Povia, M., Nachtegaal, M., Fabbri, E., Copéret, C., & Schmidt, T. J. (2016). Iridium oxide for the oxygen evolution reaction: Correlation between particle size, morphology, and the surface hydroxo layer from operando XAS. *Chemistry of Materials*, *28*(18), 6591–6604. https://doi.org/10.1021/acs.chemmater.6b02625.

Alia, S. M.; Rasimick, B.; Ngo, C.; Neyerlin, K. C.; Kocha, S. S.; Pylypenko, S.; Xu, H.; Pivovar, B. S. 2016. Activity and Durability of Iridium Nanoparticles in the Oxygen Evolution Reaction. *J. Electrochemistry. Soc.* 163 (11).

Ajayi, E. 2019. (n.d.). Fabrication of Copper/Reinforced Carbon Nanotube Bipolar Plate Using Cold Spray. https://www.researchgate.net/publication/301291779.

Amorim, I., & Bento, F. (2024). Electrochemical Sensors Based on Transition Metal Materials for Phenolic Compound Detection. In *Sensors* (Vol. 24, Issue 3). *Multidisciplinary Digital Publishing Institute (MDPI).* https://doi.org/10.3390/s24030756.

Ávila-Vázquez, V., Galván-Valencia, M., Ledesma-García, J., Arriaga, L. G., Collins-Martínez, V. H., Guzmán-Martínez, C., Escalante-Garcia, I. L., & Durón-Torres, S. M. (2015). Electrochemical performance of an Sb-doped SnO2 support synthesized by coprecipitation for oxygen reactions. *Journal of Applied Electrochemistry*. 45(11), 1175–1185. https://doi.org/10.1007/s10800-015-0876-2.

Badam, R., Hara, M., Huang, H., and Yoshimura, M, 2018. Synthesis and electrochemical analysis of the novel IrO_2 nanoparticle catalysts supported on carbon nanotube for oxygen evolution reaction. *Int J Hydrogen Energy*. Elsevier Ltd;43,468-8511.

Baik, C., Lee, S. W., & Pak, C. (2020). Control of the pore size distribution inside the RuO_2 catalyst by using silica nanosphere particles for highly efficient water electrolysis. *Microporous and Mesoporous Materials*, *309*. https://doi.org/10.1016/j.micromeso.2020.110567.

Banti, A., Papazisi, K. M., Balomenou, S., & Tsiplakides, D. (2023). Effect of Calcination Temperature on the Activity of Unsupported IrO_2 Electrocatalysts for the Oxygen Evolution Reaction in Polymer Electrolyte Membrane Water Electrolyzers. *Molecules*, *28*(15). https://doi.org/10.3390/molecules28155827.

Bhattacharyya, K., Poidevin, C., & Auer, A. A. (2021). Structure and Reactivity of IrO_x Nanoparticles for the Oxygen Evolution Reaction in Electrocatalysis: An Electronic Structure Theory Study. *Journal of Physical Chemistry C*, *125*(8), 4379–4390. https://doi.org/10.1021/acs.jpcc.0c1009.

Bojovic, N. (2022). Strategic framing of enabling technologies: Insights from firms digitizing smell and taste. *Research Policy*, *51*(3). https://doi.org/10.1016/j.respol.2021.104469.

Bonanno, M., Müller, K., Bensmann, B., Hanke-Rauschenbach, R., Aili, D., Franken, T., Chromik, A., Peach, R., Freiberg, A. T. S., & Thiele, S. (2024). Review and Prospects of PEM Water Electrolysis at Elevated Temperature Operation. *In Advanced Materials Technologies (Vol. 9, Issue 2).* John Wiley and Sons Inc. https://doi.org/10.1002/admt.202300281.

Burke, M. S., Kast, M. G., Trotochaud, L., Smith, A. M., & Boettcher, S. W. (2015). Cobalt-Iron (Oxy) hydroxide Oxygen Evolution Electrocatalysts: The Role of Structure and Composition on Activity, Stability, and Mechanism. *Journal of the American Chemical Society*, *137*(10), 3638–3648. https://doi.org/10.1021/jacs.5b00281.

Chazapis, N., Stavrou, M., Papaparaskeva, G., Bunge, A., Turcu, R., Krasia-Christoforou, T., & Couris, S. (2023). Iridium-Based Nanohybrids: Synthesis, Characterization, Optical Limiting, and Nonlinear Optical Properties. *Nanomaterials*, *13(14).* https://doi.org/10.3390/nano13142131.

Chen, H., Shi, L., Liang, X., Wang, L., Asefa, T., & Zou, X. (2020). Optimization of Active Sites via Crystal Phase, Composition, and Morphology for Efficient Low-Iridium Oxygen Evolution Catalysts. *Angewandte Chemie - International Edition*, *59*(44), 19654–19658. ttps://doi.org/10.1002/anie.202006756.

Clapp, M., Zalitis, C. M., & Ryan, M. (2023). Perspectives on current and future iridium demand and iridium oxide catalysts for PEM water electrolysis. *Catalysis Today*, *420*. https://doi.org/10.1016/j.cattod.2023.114140.

Costa de Oliveira, M. A., Machado Pico, P. P., Freitas, W. da S., D'Epifanio, A., & Mecheri, B. (2020). Iron-based electrocatalysts for energy conversion: Effect of ball milling on oxygen reduction activity. *Applied Sciences (Switzerland)*, *10*(15). https://doi.org/10.3390/APP10155278.

Daiane Ferreira Da Silva, C., Claudel, F., Martin, V., Chattot, R., Abbou, S., Kumar, K., Jiménez-Morales, I., Cavaliere, S., Jones, D., Rozière, J., Solà-Hernandez, L., Beauger, C., Faustini, M., Peron, J., Gilles, B., Encinas, T., Piccolo, L., Barros De Lima, F. H., Dubau, L., & Low-Temperature Methane Conversion. *ACS Applied Nano Materials*, *4*(10), 11145–11158. https://doi.org/10.1021/acsanm.1c02620.

Danilovic, N., Subbaraman, R., Chang, K. C., Chang, S. H., Kang, Y. J., Snyder, J., Paulikas, A. P., Strmcnik, D., Kim, Y. T., Myers, D., Stamenkovic, V. R., & Markovic, N. M. (2014). Activity-stability trends for the oxygen evolution reaction on monometallic oxides in acidic environments. *Journal of Physical Chemistry Letters*, *5*(14), 2474–2478. https://doi.org/10.1021/jz501061n.

David, S. 2021. World's largest PEM electrolyser installed in Canada. Avaliable: https://hydrogentechworld.com/worlds-largest-pem-electrolyzer-installed-in-canada. [2022, 05 September].

Fabbri, E., & Schmidt, T. J. (2018). Oxygen Evolution Reaction - The Enigma in Water Electrolysis. In *ACS Catalysis* (Vol. 8, Issue 10, pp. 9765–9774). *American Chemical Society.* https://doi.org/10.1021/acscatal.8b02712.

Felix, C., Pasupathi, S., Bladergroen, B. J., Felix, C., Maiyalagan, T., Pasupathi, S., Bladergroen, B., & Linkov, V. (2012). Synthesis, Characterisation, and Evaluation of IrO_2 Based Binary Metal Oxide Electrocatalysts for Oxygen Evolution Reaction Hydrogen and Fuel cell View project Energy Storage View project Synthesis, Characterisation and Evaluation of IrO_2 Based Binary Metal Oxide Electrocatalysts for Oxygen Evolution Reaction. In Article in *International Journal of Electrochemical Science (Vol. 7).* www.electrochemsci.org.

Gambou, F., Guilbert, D., Zasadzinski, M., & Rafaralahy, H. (2022). A Comprehensive Survey of Alkaline Electrolyzer Modeling: Electrical Domain and Specific Electrolyte Conductivity. *In Energies (Vol. 15, Issue 9)*. MDPI. https://doi.org/10.3390/en15093452.

Gao, J., Xu, C. Q., Hung, S. F., Liu, W., Cai, W., Zeng, Z., Jia, C., Chen, H. M., Xiao, H., Li, J., Huang, Y., & Liu, B. (2019). Breaking Long-Range Order in Iridium Oxide by Alkali Ion for Efficient Water Oxidation. *Journal of the American Chemical Society*, *141*(7), 3014–3023. https://doi.org/10.1021/jacs.8b11456.

García-Mota, M., Bajdich, M., Viswanathan, V., Vojvodic, A., Bell, A. T., & Nørskov, J. K. (2012). Importance of correlation in determining electrocatalytic oxygen evolution activity on

cobalt oxides. *Journal of Physical Chemistry C*, *116*(39), 21077–21082. https://doi.org/10.1021/jp306303y.

Gawande, M. B., Shelke, S. N., Zboril, R., & Varma, R. S. (2014). Microwave-assisted chemistry: Synthetic applications for rapid assembly of nanomaterials and organics. *Accounts of Chemical Research*, *47*(4), 1338–1348. https://doi.org/10.1021/ar400309b.

Götz, M., Lefebvre, J., Mörs, F., McDaniel Koch, A., Graf, F., Bajohr, S., Reimert, R., & Kolb, T. (2016). Renewable Power-to-Gas: A technological and economic review. In *Renewable Energy* (Vol. 85, pp. 1371–1390). Elsevier Ltd. https://doi.org/10.1016/j.renene.2015.07.066.

Heiranian, M., Fan, H., Wang, L., Lu, X., & Elimelech, M. (2023). Mechanisms and models for water transport in reverse osmosis membranes: history, critical assessment, and recent developments. *In Chemical Society Reviews* (Vol. 52, Issue 24, pp. 8455–8480). Royal Society of Chemistry. https://doi.org/10.1039/d3cs00395g.

Higareda, A., Hernández-Arellano, D. L., Ordoñez, L. C., Barbosa, R., & Alonso-Vante, N. (2023). Advanced Electrocatalysts for the Oxygen Evolution Reaction: From Single- to Multielement Materials. *In Catalysts* (Vol. 13, Issue 10). Multidisciplinary Digital Publishing Institute (MDPI). https://doi.org/10.3390/catal13101346.

Hoffman, J. A., Rajan, Z. S. H. S., Susac, D., Matoetoe, M. C., & Mohamed, R. (2023). Influence of Support Physicochemical Properties on the Oxygen Evolution Reaction Performance of ITO-Supported IrO_x Nanoparticles. *Journal of Physical Chemistry C*, *127*(2), 894–906. https://doi.org/10.1021/acs.jpcc.2c06501.

Hu, C., Xiao, Y., Zou, Y., & Dai, L. (2018). Carbon-Based Metal-Free Electrocatalysis for Energy Conversion, Energy Storage, and Environmental Protection. *In Electrochemical Energy Reviews* (Vol. 1, Issue 1, pp. 84–112). Springer Science and Business Media B.V. https://doi.org/10.1007/s41918-018-0003-2.

Hydrogen Production from Water Electrolysis status and future trends Ursua .(2013. (n.d.). International Energy Agency (IEA). *Global Hydrogen Review* 2022; OCED Publishing: Paris, 2022. DOI : 10.1787/39351842-en.

Jia, A., Peng, H., Zhang, Y., Song, T., Ye, Y., Luo, M., Lu, J., & Huang, W. (2021). The roles of precursor-induced metal–support interaction on the selective hydrogenation of

crotonaldehyde over Ir/TiO_2 catalysts. *Catalysts*, *11*(10). https://doi.org/10.3390/catal11101216.

Karthikeyan, B., Govindhan, R., Manikkavel, A., Karthikeyan, B., Govindhan, R., & Amutheesan, M. (2018). Noble metal oxide hybrid nanoparticles are spectroscopic. https://www.researchgate.net/publication/324983201.

Khan, I. A., Morgen, P., Gyergyek, S., Sharma, R., & Andersen, S. M. (2023). Selection of antimony-doped tin oxide (ATO) as an efficient support for iridium-based oxygen evolution reaction (OER) catalyst in acidic media. *Materials Chemistry and Physics*, *308*. https://doi.org/10.1016/j.matchemphys.2023.128192.

Khatoon, S., Kumar Yadav, S., Chakravorty, V., Singh, J., Bahadur Singh, R., Hasnain, M. S., & Hasnain, S. M. M. (2023). Perovskite solar cell's efficiency, stability, and scalability: A review. *In Materials Science for Energy Technologies* (Vol. 6, pp. 437–459). KeAi Communications Co. https://doi.org/10.1016/j.mset.2023.04.007.

Kim, Y. T., Lopes, P. P., Park, S. A., Lee, A. Y., Lim, J., Lee, H., Back, S., Jung, Y., Danilovic, N., Stamenkovic, V., Erlebacher, J., Snyder, J., & Markovic, N. M. (2017). Balancing activity, stability, and conductivity of nanoporous core-shell iridium/iridium oxide oxygen evolution catalysts. *Nature Communications*, *8*(1). https://doi.org/10.1038/s41467-017-01734-7.

Klyuev, R., Gavrina, O., & Madaeva, M. (2019). Benefits of Solar Power Plants for Energy Supply to Consumers in Mountain Territories. *International Multi-Conference on Industrial Engineering and Modern Technologies, FarEastCon*. https://doi.org/10.1109/FarEastCon.2019.8934222.

Korkmaz, S., Meydaneri Tezel, F., & Kariper, A. (2018). Synthesis and characterization of GO/IrO_2 thin film supercapacitor. *Journal of Alloys and Compounds*, *754*, 14–25. https://doi.org/10.1016/j.jallcom.2018.04.170.

Lim, D., Oh, E., Lim, C., Shim, S. E., & Baeck, S. H. (2020). Bimetallic NiFe alloys as highly efficient electrocatalysts for the oxygen evolution reaction. *Catalysis Today*, *352*, 27–33. https://doi.org/10.1016/j.cattod.2019.09.046

Liu, Y., Wang, C., Lei, Y., Liu, F., Tian, B., & Wang, J. (2018). Investigation of high-performance IrO_2 electrocatalysts prepared by Adams method. *International Journal of Hydrogen Energy*, *43*(42), 19460–19467. https://doi.org/10.1016/j.ijhydene.2018.08.196.

Mahfoudh, R., & Ghabra, N. (2023). Study of active design strategies to enhance physical activity in university educational buildings: a case study at King Abdulaziz University. *Journal of Umm Al-Qura University for Engineering and Architecture*, *14*(4), 241–270. https://doi.org/10.1007/s43995-023-00033-1.

Maillard, F. (2021). Oxygen Evolution Reaction Activity and Stability Benchmarks for Supported and Unsupported IrO_x Electrocatalysts. *ACS Catalysis*, *11*(7), 4107–4116. https://doi.org/10.1021/acscatal.0c04613.

Massué, C., Huang, X., Tarasov, A., Ranjan, C., Cap, S., & Schlögl, R. (2017). Microwave-Assisted Synthesis of Stable and Highly Active Ir Oxyhydroxides for Electrochemical Oxidation of Water. *ChemSusChem*, *10*(9), 1958–1968. https://doi.org/10.1002/cssc.201601864.

Mathew, S., Kim, J., Ha, Y., Li, O. L., & Cho, Y. R. (2021). Hybrid Catalytic-Protective Structure of $CuInS_2$ and B-N Doped Carbon as a Highly Efficient and Ultra-Stable Electrocatalyst for Oxygen Evolution Reaction. *Journal of Physical Chemistry C*, *125*(1), 546–557. https://doi.org/10.1021/acs.jpcc.0c09544.

Ma, Q., & Mu, S. (2023). Acidic oxygen evolution reaction: Mechanism, catalyst classification, and enhancement strategies. *Interdisciplinary Materials*, *2*(1), 53–90. https://doi.org/10.1002/idm2.12059.

Mazúr, P., Polonský, J., Paidar, M., & Bouzek, K. (2012). Non-conductive TiO_2 as the anode catalyst support for PEM water electrolysis. *International Journal of Hydrogen Energy*, *37*(17), 12081–12088. https://doi.org/10.1016/j.ijhydene.2012.05.129.

McCrory, C. C. L., Jung, S., Peters, J. C., & Jaramillo, T. F. (2013). Benchmarking heterogeneous electrocatalysts for the oxygen evolution reaction. *Journal of the American Chemical Society*, *135*(45), 16977–16987. https://doi.org/10.1021/ja407115p.

Mockl, M., Ernst, M. F., Kornherr, M., Allebrod, F., Bernt, M., Byrknes, J., Eickes, C., Gebauer, C., Moskovtseva, A., & Gasteiger, H. A. (2022). Durability Testing of Low-Iridium PEM Water Electrolysis Membrane Electrode Assemblies. *Journal of The Electrochemical Society*, *169*(6), 064505. https://doi.org/10.1149/1945-7111/ac6d14.

Moriau, L., Bele, M., Marinko, Ž., Ruiz-Zepeda, F., Koderman Podboršek, G., Šala, M., Šurca, A. K., Kovač, J., Arčon, I., Jovanovič, P., Hodnik, N., & Suhadolnik, L. (2021). Effect of the

Morphology of the High-Surface-Area Support on the Performance of the Oxygen-Evolution Reaction for Iridium Nanoparticles. *ACS Catalysis*, *11*(2), 670–681. https://doi.org/10.1021/acscatal.0c04741.

Musić, S., Popović, S., Maljković, M., Skoko, Ž., Furić, K., & Gajović, A. (2019). Thermochemical formation of IrO_2 and Ir. *Materials Letters*, *57*(29), 4509–4514. https://doi.org/10.1016/S0167-577X(03)00352-5.

Nady, S., Fadil, H. el, Koundi, M., Hamed, A., & Giri, F. (2022). Power to X Systems: STATE-OF-THE-ART (PTX). *IFAC-PapersOnLine*, *55*(12), 300–305. https://doi.org/10.1016/j.ifacol.2022.07.328.

Naito, T., Shinagawa, T., Nishimoto, T., & Takanabe, K. (2021). Recent advances in understanding oxygen evolution reaction mechanisms over iridium oxide. In Inorganic Chemistry Frontiers (Vol. 8, Issue 11, pp. 2900–2917). *Royal Society of Chemistry.* https://doi.org/10.1039/d0qi01465f.

Nikiforov, A. v., Tomás García, A. L., Petrushina, I. M., Christensen, E., & Bjerrum, N. J. (2011). Preparation and study of IrO_2/SiC-Si supported anode catalyst for high-temperature PEM steam electrolysers. *International Journal of Hydrogen Energy*, *36*(10), 5797–5805. https://doi.org/10.1016/j.ijhydene.2011.02.050.

Oh, H. S., Nong, H. N., Reier, T., Bergmann, A., Gliech, M., Ferreira De Araújo, J., Willinger, E., Schlögl, R., Teschner, D., & Strasser, P. (2016). Electrochemical Catalyst-Support Effects and Their Stabilizing Role for IrO_x Nanoparticle Catalysts during the Oxygen Evolution Reaction. *Journal of the American Chemical Society*, *138*(38), 12552–12563. https://doi.org/10.1021/jacs.6b07199.

Patel, P. P., Datta, M. K., Velikokhatnyi, O. I., Jampani, P., Hong, D., Poston, J. A., Manivannan, A., & Kumta, P. N. (2015). Nanostructured robust cobalt metal alloy-based anode electro-catalysts exhibiting remarkably high performance and durability for proton exchange membrane fuel cells. *Journal of Materials Chemistry A*, *3*(26), 14015–14032. https://doi.org/10.1039/c5ta01362c.

Park, J., Lee, S., & Kim, S. (2022). Recent advances in amorphous electrocatalysts for oxygen evolution reaction. *In Frontiers in Chemistry* (Vol. 10). Frontiers Media S.A. https://doi.org/10.3389/fchem.2022.1030803.

Qu, H. Y., He, X., Wang, Y., & Hou, S. (2021). Electrocatalysis for the oxygen evolution reaction in acidic media: Progress and challenges. *Applied Sciences (Switzerland)*, *11*(10). https://doi.org/10.3390/app11104320.

Quinson, J. (2022). Iridium and IrOx nanoparticles: an overview and review of syntheses and applications. *In Advances in Colloid and Interface Science* (Vol. 303). Elsevier B.V. https://doi.org/10.1016/j.cis.2022.102643.

Radinger, H., Connor, P., Stark, R., Jaegermann, W., & Kaiser, B. (2021). Manganese Oxide as an Inorganic Catalyst for the Oxygen Evolution Reaction Studied by X-ray photoelectron and Operando Raman Spectroscopy. *ChemCatChem*, *13*(4), 1175–1185. https://doi.org/10.1002/cctc.202001756.

Rajan, Z. S. H. S., Binninger, T., Kooyman, P. J., Susac, D., & Mohamed, R. (2020). Organometallic chemical deposition of crystalline iridium oxide nanoparticles on antimony-doped tin oxide support with high performance for the oxygen evolution reaction. *Catalysis Science and Technology*, *10*(12), 3938–3948. https://doi.org/10.1039/d0cy00470g.

Rao, S., & Kumar Szelam, J. (2016). Tidal Energy: A Review. *In Water Resources and Coastal Engineering*. https://www.researchgate.net/publication/310795127.

Reier, T., Oezaslan, M., & Strasser, P. (2012). Electrocatalytic oxygen evolution reaction (OER) on Ru, Ir, and Pt catalysts: A comparative study of nanoparticles and bulk materials. *ACS Catalysis*, *2*(8), 1765–1772. https://doi.org/10.1021/cs3003098.

Rossmeisl, J., Logadottir, A., & Nørskov, J. K. (2005). Electrolysis of water on (oxidized) metal surfaces. *Chemical Physics*, *319*(1–3), 178–184. https://doi.org/10.1016/j.chemphys.2005.05.038.

Sacco, L. N., & Vollebregt, S. (2023). Overview of Engineering Carbon Nanomaterials Such as Carbon Nanotubes (CNTs), Carbon Nanofibers (CNFs), Graphene and Nanodiamonds and Other Carbon Allotropes inside Porous Anodic Alumina (PAA) Templates. In *Nanomaterials* (Vol. 13, Issue 2). MDPI. https://doi.org/10.3390/nano13020260.

Saji, V. S. (2023). Corrosion and Materials Degradation in Electrochemical Energy Storage and Conversion Devices. *In ChemElectroChem* (Vol. 10, Issue 11). John Wiley and Sons Inc. https://doi.org/10.1002/celc.202300136

Salvatore, K. L., Deng, K., McGuire, S. C., Tan, S., Rui, N., Zhang, L., Rodriguez, J. A., & Wong, S. S. (2021). Microwave-Assisted Synthesis of Cu@IrO_2Core-Shell Nanowires for Low-Temperature Methane Conversion. *ACS Applied Nano Materials*, *4*(10), 11145–11158. https://doi.org/10.1021/acsanm.1c02620.

Sapountzi, F. M., Gracia, J. M., Weststrate, C. J. (Kees J., Fredriksson, H. O. A., & Niemantsverdriet, J. W. (Hans). (2017). Electrocatalysts for the generation of hydrogen, oxygen, and synthesis gas. *In Progress in Energy and Combustion Science* (Vol. 58, pp. 1–35). Elsevier Ltd. https://doi.org/10.1016/j.pecs.2016.09.001.

Saveleva, V. A., Wang, L., Kasian, O., Batuk, M., Hadermann, J., Gallet, J. J., Bournel, F., Alonso-Vante, N., Ozouf, G., Beauger, C., Mayrhofer, K. J. J., Cherevko, S., Gago, A. S., Friedrich, K. A., Zafeiratos, S., & Savinova, E. R. (2020). Insight into the Mechanisms of High Activity and Stability of Iridium Supported on Antimony-Doped Tin Oxide Aerogel for Anodes of Proton Exchange Membrane Water Electrolysers. *ACS Catalysis*, *10*(4), 2508–2516. https://doi.org/10.1021/acscatal.9b04449.

Scarpelli, F., Godbert, N., Crispini, A., & Aiello, I. (2022). Nanostructured Iridium Oxide: State of the Art. In *Inorganics* (Vol. 10, Issue 8). MDPI. https://doi.org/10.3390/inorganics10080115.

Shamma, A. M. (1980). *The 1973 Oil Embargo Arab Oil Diplomacy*. https://scholarworks.wmich.edu/masters theses.

Shiva Kumar, S., & Himabindu, V. (2019). Hydrogen production by PEM water electrolysis – A review. *In Materials Science for Energy Technologies* (Vol. 2, Issue 3, pp. 442–454). KeAi Communications Co. https://doi.org/10.1016/j.mset.2019.03.002.

Shell. 2021. *Recharge: Global News and Intelligence for the Energy Transition*. Available: https://www.shell.com/media/news-and-media-releases/2021/shell-starts-up-europes-largest-pem-green-hydrogen-electrolyser.html.[2022, 16 November].

Shi, G., Tano, T., Tryk, D. A., Uchiyama, T., Iiyama, A., Uchida, M., Terao, K., Yamaguchi, M., Tamoto, K., Uchimoto, Y., & Kakinuma, K. (2023). Nanorod Structuring of IrO_x on a Unique Microstructure of Sb-Doped Tin Oxide to Dramatically Boost the Oxygen Evolution Reaction Activity for PEM Water Electrolysis. *ACS Catalysis*, *13*(18), 12299–12309. https://doi.org/10.1021/acscatal.3c01647.

Siemens Energy. 2021. *Recharge: Global News and Intelligence for the Energy Transition*. Available: https://www.siemens-energy.com/global/en/home/products-services/product-offerings/hydrogen-solutions.html.[2022, 16 November].

Singerling, B. S. A.; Schulte, R. F. (2018). Minerals Yearbook Platinum-Group Metals; USGS: New York, 2021. https://d9-wret.s3. us-west-2.amazonaws.com/assets/palladium/production/atoms/files/myb1-2018-plati.pdf. Live PGM Prices - Price of Iridium, Rhodium, Rhenium &Osmium. *Metals Daily*. https://www.metalsdaily.com/live-prices/pgms/.

Suen, N. T., Hung, S. F., Quan, Q., Zhang, N., Xu, Y. J., & Chen, H. M. (2017). Electrocatalysis for the oxygen evolution reaction: Recent development and future perspectives. *In Chemical Society Reviews* (Vol. 46, Issue 2, pp. 337–365). Royal Society of Chemistry. https://doi.org/10.1039/c6cs00328a.

Sztaberek, L., Mabey, H., Beatrez, W., Lore, C., Santulli, A. C., & Koenigsmann, C. (2019). Sol-Gel Synthesis of Ruthenium Oxide Nanowires to Enhance Methanol Oxidation in Supported Platinum Nanoparticle Catalysts. *ACS Omega*, *4*(10), 14226–14233. https://doi.org/10.1021/acsomega.9b01489.

Tan, X., Shen, J., Semagina, N., & Secanell, M. (2019). Decoupling structure-sensitive deactivation mechanisms of Ir/IrO_x electrocatalysts toward oxygen evolution reaction. *Journal of Catalysis*, *371*, 57–70. https://doi.org/10.1016/j.jcat.2019.01.018.

Tatrari, G., Ahmed, M., & Shah, F. U. (2024). Synthesis, thermoelectric and energy storage performance of transition metal oxide composites. In *Coordination Chemistry Reviews* (Vol. 498). Elsevier B.V. https://doi.org/10.1016/j.ccr.2023.215470.

van der Merwe, M., Garcia-Diez, R., Lahn, L., Wibowo, R. E., Frisch, J., Gorgoi, M., Yang, W., Ueda, S., Wilks, R. G., Kasian, O., & Bär, M. (2023). The Chemical and Electronic Properties of Stability-Enhanced, Mixed $Ir\text{-}TiO_x$ Oxygen Evolution Reaction Catalysts. *ACS Catalysis*, *13*(23), 15427–15438. https://doi.org/10.1021/acscatal.3c02948.

Wang, H., Sayed, S. Y., Luber, E. J., Olsen, B. C., Shirurkar, S. M., Venkatakrishnan, S., Tefashe, U. M., Farquhar, A. K., Smotkin, E. S., McCreery, R. L., & Buriak, J. M. (2020). Redox Flow Batteries: How to Determine Electrochemical Kinetic Parameters. *ACS Nano*, *14*(3), 2575–2584. https://doi.org/10.1021/acsnano.0c01281.

Wang, H., Zhang, K. H. L., Hofmann, J. P., de la Peña O'Shea, V. A., & Oropeza, F. E. (2021). The electronic structure of transition metal oxides for oxygen evolution reaction. In *Journal of Materials Chemistry A* (Vol. 9, Issue 35, pp. 19465–19488). Royal Society of Chemistry. https://doi.org/10.1039/d1ta03732c.

Wei, C.; Rao, R. R.; Peng, J.; Huang, B.; Stephens, I. E. L.; Risch, M.; Xu, Z. J.; Shao-Horn, Y. 2019. Recommended Practices and Benchmark Activity for Hydrogen and Oxygen Electrocatalysis in Water Splitting and Fuel Cells. *Adv. Mater. 31* (31).

Wong, S. S., & Tong, X. (2021). Lanthanum-based double perovskite nanoscale motifs as support media for the methanol oxidation reaction.

Yao, Y., Lyu, J., Li, X., Chen, C., Verpoort, F., Wang, J., Pan, Z., & Kou, Z. (2024). A review of efficient electrocatalysts for the oxygen evolution reaction at large current density. *DeCarbon*, *5*, 100062. https://doi.org/10.1016/j.decarb.2024.100062.

Xu, J., Li, Q., Hansen, M. K., Christensen, E., Tomás García, A. L., Liu, G., Wang, X., & Bjerrum, N. J. (2012). Antimony-doped tin oxides and their composites with tin pyrophosphates as catalyst support for oxygen evolution *reaction in proton exchange membrane water electrolysis. International Journal of Hydrogen Energy, 37(24), 18629–18640*. https://doi.org/10.1016/j.ijhydene.2012.09.156.

Ye, H., Park, H. S., & Bard, A. J. (2011). Screening of electrocatalysts for photoelectrochemical water oxidation on W-doped $BiVO_4$ photocatalysts by scanning electrochemical microscopy. *Journal of Physical Chemistry C*, *115*(25), 12464–12470. https://doi.org/10.1021/jp200852c.

Zaman, W. Q., Sun, W., Zhou, Z. H., Wu, Y., Cao, L., & Yang, J. (2018). Anchoring of IrO_2 on One-Dimensional Co_3O_4 Nanorods for Robust Electrocatalytic Water Splitting in an Acidic Environment. *ACS Applied Energy Materials*, *1*(11), 6374–6380. https://doi.org/10.1021/acsaem.8b01349.

Zhao, F., Wen, B., Niu, W., Chen, Z., Yan, C., Selloni, A., Tully, C. G., Yang, X., & Koel, B. E. (2021). Increasing Iridium Oxide Activity for the Oxygen Evolution Reaction with Hafnium Modification. *Journal of the American Chemical Society*, *143*(38), 15616–15623. https://doi.org/10.1021/jacs.1c03473.

Zhao, S., Stocks, A., Rasimick, B., More, K., & Xu, H. (2018). Highly Active, Durable Dispersed Iridium Nanocatalysts for PEM Water Electrolyzers. *Journal of The Electrochemical Society*, *165*(2), F82–F89. https://doi.org/10.1149/2.0981802jes.

Zoller, F., Häringer, S., Böhm, D., Luxa, J., Sofer, Z., & Fattakhova-Rohlfing, D. (2021). Carbonaceous Oxygen Evolution Reaction Catalysts: From Defect and Doping-Induced Activity over Hybrid Compounds to Ordered Framework Structures. *In Small (Vol. 17, Issue 48).* John Wiley and Sons Inc. https://doi.org/10.1002/smll.202007484.

Chapter 3: SYNTHESIS AND CHARACTERISATION

The chapter describes the synthesis processes that were used to synthesise IrO_x-based materials for use in OER. This section also describes the various post-treatments introduced and the supporting and alloying of the catalyst. It also covers the various physical and electrochemical methods used to study the nanomaterials.

3.1 Reagents/material and glassware cleaning

Ir metal powder with a purity of 99% was received from Impala Platinum mining company. Sodium peroxide (Na_2O_2), isopropanol (IPA, 99.5%), Nafion, hydrogen peroxide (H_2O_2, 36.5%) sulphuric acid, hydrogen hexachloroiridate (IV) hydrate ($H_2IrCl_6 \cdot xH_2O$, 99.0%) and perchloric acid ($HClO_4$, 70.0%) were purchased at Sigma Aldrich and used without further purification. Nafion® ionomer solution (5 wt.% in water and aliphatic alcohols) Fuel Cell Earth. Ultra-pure deionised water was obtained from a Millipore Synergy Milli-Q® dispenser 18 Ω.cm was used throughout the experiments. All experiment glassware was soaked in a Nochromix® solution 1 for 24 hrs, the glassware was rinsed with deionised water a few times. The glassware was rinsed with deionised water a few times. Then, soaked in solution 2 and rinsed with ultrapure 18 MΩ Millipore deionised water before boiling it overnight. In preparation for solution 1 - in a 5L glass beaker 15 mL of [H_2SO_4] was added into 3 L of deionised water and a mass of 3 g of potassium permanganate ($KMnO_4$). Solution 2 - was prepared by adding 5 mL [H_2SO_4], 1 ml [H_2O_2], and 1L deionised water into a 2L beaker.

3.2 Synthesis of unsupported IrO_x using the Adam Fusion method varying the oxidants

3.2.1 Procedure using sodium peroxide vs barium peroxide as an oxidation agent

Figure 3.1 shows a schematic illustration of the synthesis process of the IrO_x catalyst. The optimal synthesis conditions were as follows; a ratio of 1:2 Ir-Na_2O_2 was bead-milled at 400 rpm for two hours with 10-minute resting intervals every 30 minutes. A planetary bead mill has a single Teflon grinding jar that is mounted on a planetary disc. A sample was placed inside a jar and filled with zirconium beads. A shaker was used to remove the excess reagents from the bead-mill beads and the mixture was then calcined in a preheated oven at 700 °C for eight hours using an aluminium oxide crucible in air. The sample was rinsed with 0.1 M HCl acidic

solution and followed by deionised water using a centrifuge at 5000 rpm and Rcf – 6.50 for five minutes each. The sample was dried overnight in an oven at 60 °C, and the catalyst was crushed and mixed using mortar and pestle before being characterised.

Figure 3-1: Schematic illustration of the synthesis process of Iridium oxide electrocatalysts.

During this evaluation, IrO_x was synthesised by a modified method described in section 3.2.1 in which barium peroxide was used as an oxidising agent. The catalyst was calcined in a two-step process under the same conditions for 6 hours at 700 °C in air. After the second calcination step, it was centrifuged using 0.0 1 M nitric acid (HNO_3) followed by hot deionised water. The solid retained was placed in an oven at 60 °C overnight.

3.2.2 Effects of post treatment methods on the Unsupported In-house catalysts

Three catalysts were synthesised using the method described in section 3.2.1 and were cooled differently after thermal treatment. These methods include the use of liquid nitrogen, carbon dioxide (dry ice), and slowing cooling. The $IrO_{x\text{-}(Na)\text{-}(S)}$ catalyst was slowed cooled in the

furnace after a period of 8 hours. The $IrO_{x-(Na)-(R)}$ was removed from the furnace at high temperatures and liquid nitrogen was then poured into the crucible as post-cooling. The same was done for the $IrO_{x-(Na)-(Q)}$ sample, however, carbon dioxide (CO_2) was used as cooling post-treatment.

3.3 Synthesis of mixed-metal nanoparticles supported with tantalum pentoxide using Adam Fusion

3.3.1 Synthesis of mixed metal using metallic iridium and tantalum pentachloride

The goal of this experiment was to synthesise a mixed-metal catalyst using a mixture of metallic Ir and tantalum pentachloride ($TaCl_5$). The synthesise, centrifugation and drying steps were applied according to section 3.2.1.

3.3.2 Synthesis of iridium oxide supported on tantalum pentoxide

A mass of Ta_2O_5 powder and dihydrogen hexachloroiridate (IV) hydrate ($H_2Cl_6Ir^{x}H_2O$) were stirred together in 5 mL isopropanol (IPA) for one hour. A mass of 2.3 g of sodium nitrate ($NaNO_3$) was added to the mixture and stirred overnight. The IPA was evaporated under stirring and heating at 80 °C until a solid was collected. The obtained solid was calcined in the muffle oven for 1h at 350 °C using a ramp rate of 4 °C/min. After cooling down, the grey to black solid was dispersed in water and washed five times with deionised water with a centrifuge and the catalyst was dried overnight in the oven at 60 °C.

3.4 Physical characterisation

3.4.1 X-ray Diffraction (XRD)

The XRD was used to determine the electrocatalyst's crystal structure and crystalline size. The Bruker D8 Advance diffractometer was used for the XRD measurements. It has a monochromatic Co kα radiate on (λ = 1.79026 Å) and operates at 40 kV and in the 1D mode with the Lyn-Eye-XE detector. In sample preparation, traces of impurities were extracted from

a zero-background film using ethanol solvent and a small amount of electrocatalyst was positioned on top of a zero-background. The X-ray beam hit the surface at a 2-theta angle ranging from 20 to 120 °C to produce the respective diffractograms. It was recorded using a step-scan method with a step size of 0.05 degrees, and a scan rate of 0.5 degrees per minute. The crystallographic lines were then compared with known patterns using the JCPDS database's search tool.

The particle size was computed using the Debye–Scherrer equation shown below (Monshi et al., 2012) which considers the intensity of the diffraction line.

Scherrer equation: $D = k\lambda/BCos\theta$

The nano crystallite size (D) is calculated by considering the wavelength λ (nm) of the radiation from measuring the corrected full width at half maximum (FWHM) of peaks (β) in the radian located at any diffracting angle of the peak (θ) in the pattern. Scherrer constant (k) can be 0.62 - 2.08 and in this study, the value used was 0.89 for calculations. All measurements were done at the University of Cape Town.

3.4.2 Scanning Electron Microscopy and Energy Dispersive X-ray Spectroscopy (SEM-EDX)

Energy-dispersive X-ray spectroscopy (EDX) was used to identify the elementary composition for all synthesised electrocatalysts. This technique was performed by connecting an EDX system with a Scanning Electron Microscopy (SEM). In this study, SEM, FEI Nova Nano SEM 230 was used to detect and generate X-rays powered by 20 kV beam energies and equipped with the Oxford X-22 MAX detector. EDX was used to quantify the elemental constituents (Ir, O, Na, and Ta) in the synthesised electrocatalysts. INCA Point and ID software were also used to obtain the element quantification and spectra. Ms Miranda Waldron at the University of Cape Town's Electron Microscope Unit (UCT-EMI) conducted all measurements.

3.4.3 X-ray Photoelectron Spectroscopy (XPS)

The XPS is a surface-based technique used to analyse the material composition based on the observed characteristic electron binding energies. The data collected using the XPS technique were analysed to study the oxidation state of iridium present in the synthesised and commercial

electrocatalysts. These measurements were performed on a Kratos Analytical Axis Ultra DLD system with a monochromatic Al Kα source (1486.71 eV). Samples were measured in XPS in a Thermo K-Alpha instrument using a monochromate Al Kalpha source and charge compensation. The overall energy resolution for core levels acquisition is better than 0.7 eV. The XPSPeak4.1 software was used to fit the Ir 4f, and Ta 4f, components.

A curve-fitting procedure was performed for the photoelectron peaks with a Lorentzian-Gaussian ratio of 20, with TS and TL asymmetry factors of 0.2 and 100 curve-fitted unless stated otherwise. The Shirley background was used to compensate for the inelastic scattering of electrons, which can occur when an electron gets caught in a collision with another electron as it exits a sample. The Ir 4f peaks were fitted with satellite peaks for the oxidation states Ir (III) and Ir (IV).

3.4.4 Transmission Electron Microscopy (TEM)

The TEM characterisation technique allows the study of the various aspects of the catalyst's structure and distribution by directly observing and measuring the individual nanoparticles. It also provides data on the particle size, morphology of the nanoparticles, and distribution of the support material. (Akbari 2011). The samples were prepared by dispersing approximately 2 mg of catalyst in isopropanol (IPA) and were ultra-sonicated (Kimix Analytical Reagent (AR)) for 20 mins. A drop of the sample was placed on a copper grid, which was then dried. The measurements were conducted on the synthesis of various catalysts by Dr. Nasheeta Hanief of the UCT-EMI using the F20 CRYO FEGTEM microscope. The instrument has a high-performance image of 200kV with CRYO capability using FEI imaging software. The visible lattice fringes on the images were used to extract the d-spacings of electrocatalyst nanoparticles and were then analysed using Image J, a Java-based software and the size distribution was studied statistically in histograms. To get the crystallite size accurately, ± 150 particles were analysed in each image.

3.4.5 Brunauer, Emmett and Teller (BET) surface area analyser

The concept of the BET theory is a method utilized to determine the average specific surface area (m^2/g) of porous materials or solids by means of nitrogen adsorption. Prior to the

measurement being performed, all samples were decontaminated to remove contaminants, including water. This process was conducted in a vacuum at extremely high temperatures. For the BET procedure, a minimum of ± 500 mg of sample was required.

3.5 Electrochemistry analysis

3.5.1Three-electrode electrochemical cell

All electrochemical experiments were performed ex-situ using the Gamry Instruments' potentiostat at room temperature (± 25 °C). The experimental rotational disc electrode (RDE) electrochemistry cell consisted of three components: an electrolyte, a glass cell, and electrodes, as shown in Figure 3.2. The GCE used as a working electrode was cleaned using the method described in section 3.5.3. The reference electrode used for this study was a mercury/mercurous sulphate oxide ($Hg/HgSO_4$) and was calibrated to the reversible hydrogen electrode (RHE) before each measurement. A platinum mesh counter electrode was used, and it was cleaned with a flame torch to remove traces of impurities. This component is used to complete a circuit and not limit the current. A gas inlet was used to ensure that the equilibrium of oxygen (O_2) is attained at a certain standard potential. The use of electrochemistry is a sensitive technique that requires deep cleaning mentioned in section 3.1 to remove any traces of metallic or organic impurities from glassware.

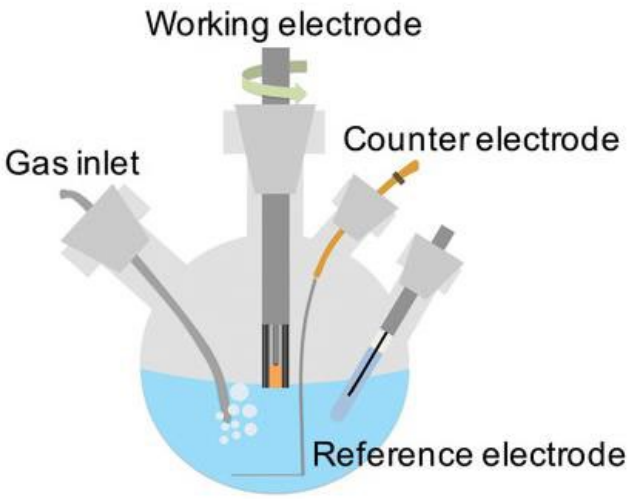

Figure 3-2: A three-electrode electrochemical cell setup consisting of three electrodes: working electrode, a counter electrode, reference electrode and gas inlet (Wei et al, 2019).

3.5.2 Preparation of electrolyte and calibration of reference potential

In a volumetric flask 0.1 M perchloric acid ($HClO_4$) was prepared by adding approximately 2.156 mL of $HClO_4$ filled up with deionised water to the desired volume. A glass container was filled with approx. 150 mL of 0.1 M $HClO_4$ electrolyte inside a fume cupboard, which was then bubbled with hydrogen for around 10 minutes. The two-probe multi-meter's metal tips were connected to the reference electrode Hg/H_2SO_4 and the platinum mesh counter electrode for reference potential reading in mV.

3.5.3 Ink formulation and cleaning of Glassy Carbon Electrode (GCE)

A standard catalyst ink was prepared by adding 7.6 mg of electrocatalyst material in a mixture of 7.6 ml H_2O and 2.4 m1 isopropanol, with a 40 µL Nafion® solution (5 wt% Nafion 117, Sigma-Aldrich). The ink was ultra-sonicated for approximately 30 mins and stirred for 10 mins before depositing 10 µL aliquot onto 0.196 cm^2 a micro-polished carbon disc electrode to achieve a catalyst loading of 100 μg_{cat} cm^{-2} dried at 60 °C for 10 mins in the oven.

Step 1 - the GCE surface area was initially rubbed against Meta-Di Supreme polycrystalline diamond 6µm which was sprayed onto lens paper. It was then subjected to an alumina powder of 1.0 µm and finally to 0.05 µm rinsing with deionised water in between. Step 2 – this was done to remove any powder residues remaining on the GCE surface area wall. An electrode was submerged in DI water, then into isopropanol and finally in DI water sonicated in intervals of 10 mins in each solvent.

3.5.4 Oxygen evolution reaction conditioning and activity protocol

At the beginning of the electrochemistry measurements, all the electrodes were subjected to cyclic voltammetry (CV) to clean and activate the catalyst layer. This was conducted at a potential window of 0 - 1.2 V vs RHE at a scan rate of 100 $mV.s^{-1}$ for fifty cleaning cycles. The OER activity was evaluated using a CV scan rate of 10 $mV.\ s^{-1}$ and corrected for internal resistance in the potential range 1.0 - 1.6V vs RHE. Electrochemical impedance spectroscopy (EIS) was performed at 1.0 V vs. RHE at a frequency range of 100 kilohertz (kHz) to one hundred millihertz (mHz.). This was done to determine the effective ohmic resistance used for

iR-correction. To eliminate the bubble formation, the electrode was rotated at 1600 rpm and the electrochemistry cell was also tilted to allow the removal of the bubbles. The CV's backward and forward sweeps were averaged to eliminate the currents that are generated by the capacitive elements found on the electrode's surface. Once the linear sweeps were averaged, the solution resistance was corrected using EIS analysis. All OER activity measurements were done in triplicate, and the mass activities were specified as OER activity standardised based on the mass of metallic Ir covered on the working electrode. All catalysts' activity was compared at 1.525 V vs. RHE.

3.5.5 Catalyst Durability Protocol

The durability tests were conducted by holding at 1.6 V vs. RHE for a duration of two hours. The catalyst was exposed to activation steps using chronoamperometry from 1.5 - 1.560V vs. RHE in 20 mV steps, for a period of 1 minute per step before and after the durability test to determine the relative loss of mass activity. These before and after chronoamperometry were used to plot Tafel slopes which can estimate the durability of the catalyst.

3.5.6 Electrochemical Surface Area (ECSA)

The ECSAs were determined using the same CV conditions mentioned in section 3.5.4. The ECSA was determined by considering the double-layer capacitance on the catalytic surface. A non-Faradaic capacitive current is associated with the double-layer charging process (McCrory 2013). The double-layer capacitance was determined in a potential window of 0.2 – 0.3 V at various scan rates ranging from 10, 25, 50, 100, and 500 millivolts per second. In this work, the ECSA of the electrocatalysts were estimated using the double-layer capacitance of the catalysts. The linear slope of the current vs scan rate, which is equivalent to twice the double-layer capacity (Cdl), was then used as the ECSA's representation.

3.6 References

Akbari, B., Pirhadi Tavandashti, M., & Zandrahimi, M. (2011). Particle size characterisation of nanoparticles – a practical approach.

Gómez-Tena, M. P., Gilabert, J., Toledo, J., Zumaquero, E., & Machí, C. (n.d.). (2013). Relationship between the specific surface area parameters determined using different analytical techniques. www.qualicer.org.

Fabbri, E., Habereder, A., Waltar, K., Kötz, R., & Schmidt, T. J. (2014). Developments and perspectives of oxide-based catalysts for the oxygen evolution reaction. *In Catalysis Science and Technology* (Vol. 4, Issue 11, pp. 3800–3821). https://doi.org/10.1039/c4cy00669k.

Lee, J., and Kim, Y. 2011. Chemical Dissolution of Iridium Powder Using Alkali Fusion Followed by High-Temperature Leaching. Mater. Trans. 52 (11): 2067–2070.

McCrory, C. C. L., Jung, S., Peters, J. C., & Jaramillo, T. F. (2013). Benchmarking heterogeneous electrocatalysts for the oxygen evolution reaction. *Journal of the American Chemical Society*, *135*(45), 16977–16987. https://doi.org/10.1021/ja407115p.

Monshi, A., Foroughi, M. R., & Monshi, M. R. (2012). Modified Scherrer Equation to Estimate More accurately Nano-Crystallite Size Using XRD. *World Journal of Nano Science and Engineering*, *02*(03), 154–160. https://doi.org/10.4236/wjnse.2012.23020.

Sinha, P., Datar, A., Jeong, C., Deng, X., Chung, Y. G., & Lin, L. C. (2019). Surface Area Determination of Porous Materials Using the Brunauer-Emmett-Teller (BET) Method: Limitations and Improvements. *Journal of Physical Chemistry C*, *123*(33), 20195–20209. https://doi.org/10.1021/acs.jpcc.9b02116.

Thommes, M., Kaneko, K., Neimark, A. v., Olivier, J. P., Rodriguez-Reinoso, F., Rouquerol, J., & Sing, K. S. W. (2015). Physisorption of gases, with special reference to the evaluation of surface area and pore size distribution (IUPAC Technical Report). *Pure and Applied Chemistry*, *87*(9–10), 1051–1069. https://doi.org/10.1515/pac-2014-1117

Wei, C., Rao, R. R., Peng, J., Huang, B., Stephens, I. E. L., Risch, M., Xu, Z. J., & Shao-Horn, Y. (2019). Recommended Practices and Benchmark Activity for Hydrogen and Oxygen Electrocatalysis in Water Splitting and Fuel Cells. *In Advanced Materials* (Vol. 31, Issue 31). Wiley-VCH Verlag. https://doi.org/10.1002/adma.201806296.

Chapter 4: SYNTHESIS AND CHARACTERISATION OF IRIDIUM OXIDE NANOMATERIALS

This chapter presents the data interpretation and discussion of the synthesis of unsupported iridium oxide nanomaterials using two different oxidizing agents, three cooling post-treatment methods, mixed-metal composition, and support material. The properties of the IrO_x nanoparticles were evaluated through spectroscopic characterization techniques. The discussion of the data and spectral analysis is compared to relevant literature for validation and insight.

4.1 Observations during synthesis of iridium-based materials

A total of seven different iridium-based nanomaterials were synthesized and compared to commercial iridium oxide in this chapter. Table 4.1 provides a brief description and sample identification used throughout the study. Physicochemical characterisation techniques were employed to evaluate the properties of both the commercial and synthesized iridium oxide nanomaterials. The resulting data was analysed and compared with relevant literature findings.

Table 4-1: *Sample identification and compound description of the synthesised and commercial iridium-based nanomaterials.*

Sample ID	Description
$IrO_{x\text{-}(Na)}$	Metallic Ir + Na_2O_2
$IrO_{x\text{-}(Ba)}$	Metallic Ir + Ba_2O_2
TKK	Commercial benchmark
$IrO_{x\text{-}(Na)\text{-}(S)}$	*(slow cooled)
$IrO_{x\text{-}(Na)\text{-}(R)}$	*(rapid cooled)
$IrO_{x\text{-}(Na)\text{-}(Q)}$	*(quenched)
$TaIrO_x$	Metallic + tantalum pentachloride + Na_2O_2
IrO_2-TiO_2	Commercial benchmark

Symbol (*) represents metallic iridium and Na_2O_2.

4.1.1 Synthesis of iridium oxide using various oxidising agents

During the synthesis of $IrO_{x-(Na)}$, special attention was given to the transfer process following the bead-milling step described in Chapter 3, Section 3.2.1. After bead milling, the mixture was immediately transferred into an alumina crucible to prevent exposure to air. This rapid transfer was essential to preserve the integrity of sodium peroxide (Na_2O_2), the oxidising agent used in the reaction.

Sodium peroxide, initially yellow undergoes a visible change when exposed to air, turning white due to its reaction with atmospheric moisture. This process leads to the formation of sodium hydroxide (NaOH) and hydrogen peroxide (H_2O_2), as shown in Equation (4.1):

$$Na_2O_2 + H_2O \rightarrow 2NaOH + H_2O_2 \qquad \text{(Equation 4.1)}$$

The formation of hydrogen peroxide is concerning because it decomposes at room temperature, producing water and oxygen gas, as indicated in Equation (4.2):

$$2H_2O_2 \rightarrow 2H_2O + O_2 \qquad \text{(Equation 4.2)}$$

This decomposition reduces the oxidation capacity of the sodium peroxide. In the context of synthesising $IrO_{x-(Na)}$, the effectiveness of Na_2O_2 as an oxidising agent directly impacts the oxidation state and crystalline structure of the resulting iridium oxide. Therefore, any reduction in its oxidising capacity can negatively affect the overall reaction efficiency and product quality.

To mitigate this issue, in this work the experimental protocol emphasised minimising the exposure time of sodium peroxide to air. Similar challenges related to the instability of sodium peroxide have been reported in the literature, particularly in studies where maintaining high oxidation potential is critical for achieving desired reproducible and high-quality material properties (Alberta, 2016).

After the calcination step, the crucible was removed from the intense heat during the calcination process to prevent the formation of particle growth. The nanomaterial synthesised using sodium peroxide had a molten compared to the barium peroxide material. The dark blue liquid colour that was observed during the centrifugation process for iridium oxide could be the result of the presence of ions in the solution. Iridium compounds usually have a black or dark blue colour

due to their electronic structure (Hintermair 2013). The final nanomaterials products were black and hydrophilic.

4.1.2 Synthesis of iridium oxide using various cooling post-thermal treatment

Various cooling post-treatments aimed to increase the surface area of IrO_x nanomaterials. Three different post-treatments of cooling were implemented: cryogenic agents' liquid nitrogen (N_2), dried ice (CO_2), and slow cooling in the furnace. The cooling post-treatments did not produce any notable differences for the iridium oxide products, which were hydrophilic and fine powdered black materials. The rapid and quenching cooling using liquid nitrogen and dry ice, respectively was implemented to promote the growth of finer structures or smaller particles(Jagga et al., 2020). The cooling rate of dry ice is slower than that of liquid nitrogen, which can result in different crystalline structures and particle sizes (Powers et al., 2024).

4.1.3 Synthesis of supported and mixed metal iridium oxide

After the synthesis of the two Ir-based materials, which were black $TaIrO_x$ and grey IrO_x-Ta_2O_5, the yields of these were 80 percent respectively. The $TaIrO_x$ material had a supernatant that was dark blue, this was observed in the various nanomaterials that were prepared using a sodium peroxide oxidising agent discussed in section 4.1.1.

4.2 XRD analysis of IrO_x nanomaterials

4.2.1 XRD analysis of IrO_x nanomaterials using different oxidising reagents and post-treatment

The XRD technique was utilised to confirm the structural characterisation of IrO_x nanomaterials. Figure 4.1 shows a comparison of the X-ray diffraction patterns recorded from the IrO_x commercial benchmark and six in-house synthesised IrO_x nanomaterials with corresponding reference diffraction pattern lines. According to quantitative XRD analysis, all nanomaterials exhibit a broad hump/peak around ± 35° 2θ, indicating an amorphous or low degree of crystallinity materials. A broad hump or peak near 30 - 35° 2θ in amorphous iridium oxide usually represents the material's mean interatomic distance which may resemble the atomic order of the crystalline IrO_x's 101 plane (Czioska et al., 2021). Unlike in crystalline materials, the patterns of XRD in amorphous iridium oxide do not have sharp peaks that are

associated with certain types of crystallographic planes. Instead, they are characterised by diffuse humps, which represent short-range atomic arrangements (Ali et al., 2022). The XRD particle and crystallite sizes of the IrO_x materials were not calculated due to the Scherrer equation is based on the well-defined Bragg Diffraction from crystalline materials. A broad hump in amorphous substances indicates that there are no such planes.

Similar results were observed in previous studies such as (Pfeifer et al., 2015; Tan et al., 2019 and Willinger et al., 2017). However, the Pfeifer diffraction pattern still showed metallic Ir attribution diffraction peak at 41°, 58° and 69° 2θ. In comparison of Figure 4.1 (a) and (b) all the prepared and commercial IrO_x materials exhibited no distinctive peaks for Ir (PDF 00-046-1044 JCPDS database's search tool) and IrO_2 (PDF 00-015-0870) XRD pattern. This could be because of the small particle size of the IrO_x nanoparticles below the detection limit of 3 nm. It has been reported that these materials exhibit enhanced OER catalytic capabilities due to their elevated surface area and number of active sites. While the synthesis did not achieve the formation of highly crystalline rutile IrO_2, the resulting amorphous IrO_x structure is still valuable, particularly for electrochemical applications such as the oxygen evolution reaction (Park et al., 2022).

In comparison Figure 4.1 (b) to (a), the is a slight decrease in the intensity of the (101) orientation of IrO_2 seen in the XRD patterns of the nanomaterials prepared using cooling post-treatment. The $IrO_{x\text{-}(Na)}$ and $IrO_{x\text{-}(Na)\text{-}(Q)}$ nanomaterials exhibited an additional peak at ± 23° 2θ which corresponds to Na_2IrO_3 suggesting that it is likely that traces of sodium iridate remained in the samples (Lee et al., 2011; Krizan et al., 2014). From the XRD analysis, it is difficult to understand what is going on for each nanomaterial since there is no substantial difference between them.

An interesting trend has been observed from different publications (Xu et al., 2017), for an example most iridium oxide nanomaterials synthesised using Ir-based salts such as iridium chloride ($IrCl_3$), Chazapis et al., 2023 & Zaman et al., 2018), and hydrogen hexachloroiridate (IV) hydrate (H_2IrCl_6 x H_2O) (Scarpelli et al., 2022; Patel et al., 2015), have an amorphous structure at low temperature below 350 °C and crystalline structure at high temperatures above 400 °C. However, this is not the case in this study, the trend is inversely proportional at higher temperatures 700 °C the iridium-based nanomaterials exhibit amorphous structure. Iridium oxide nanomaterials at higher temperatures favour crystalline structures made from salts, this would not be the same coming from a metal precursor despite using the Adam fusion method.

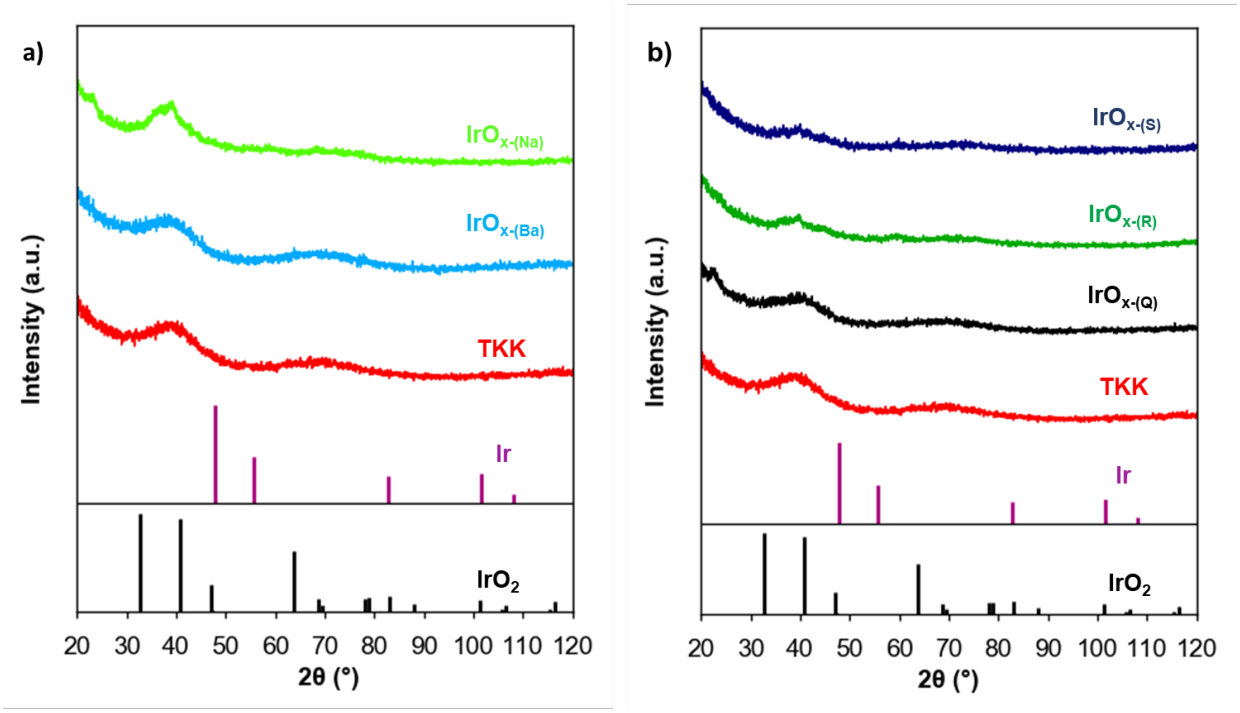

Figure 4-1: X-ray diffractograms (a) of the synthesised IrO_x nanomaterials using sodium $IrO_{x-(Na)}$, vs barium peroxide $IrO_{x-(Ba)}$ oxidising agent and (b) represent IrO_x nanomaterials made using various cooling methods compared to commercial IrO_x TKK. Purple lines represent Ir metal and black lines iridium oxide XRD patterns.

4.2.2 XRD analysis of IrO_x nanomaterials of the mixed-metal and supported material

In Figure 4.2, an X-ray diffraction analysis of the IrO_x-Ta_2O_5 showed that it has a low-intensity crystalline structure. Two IrO_2 weakly defined narrow peaks correspond to crystallographic planes. The left-shift pattern in the XRD peaks at (110) and (101) at 25° and 34 ° 2θ can be interpreted as evidence of an increase in the lattice spacing (Felix et al., 2022). Bragg's law states that when the d-spacing increases, the angle of diffraction decreases (Monshi et al., 2012). In comparison to $TaIrO_x$ nanomaterials exhibit the same structural characteristics (broad overlapping peaks at 35° 2θ indicate that there is no single oxide phase) discussed in section 4.2.1. Using the Scherrer formula for calculating the particle size of Ta-Ir was difficult due to the broad overlapping peaks. The low crystallinity of IrO_2 was attributed caused by the addition of Ta_2O_5, which is consistent with what is reported in the literature (Felix et al., 2012 Rasten et al., 2001).

The commercial nanomaterial exhibits a crystalline structure of IrO_2 with sharp peaks corresponding to crystallographic planes (110), (101), (200), (211) found at 34°, 42°, 48°, and

64° (Pfeifer et al., 2015). Yuan and colleagues (2017) noted that IrO_2 and TiO_2 are two kinds of rutile crystals that are part of a tetragonal configuration. They share similar lattice constants and symmetry, which makes them ideal for creating composite oxides with varying ratios. The XRD particle and crystallite sizes of the commercial IrO_2-TiO_2 materials were not calculated due to the in-house synthesised nanomaterials having no well-defined peaks which makes it irrelevant for comparison across the materials.

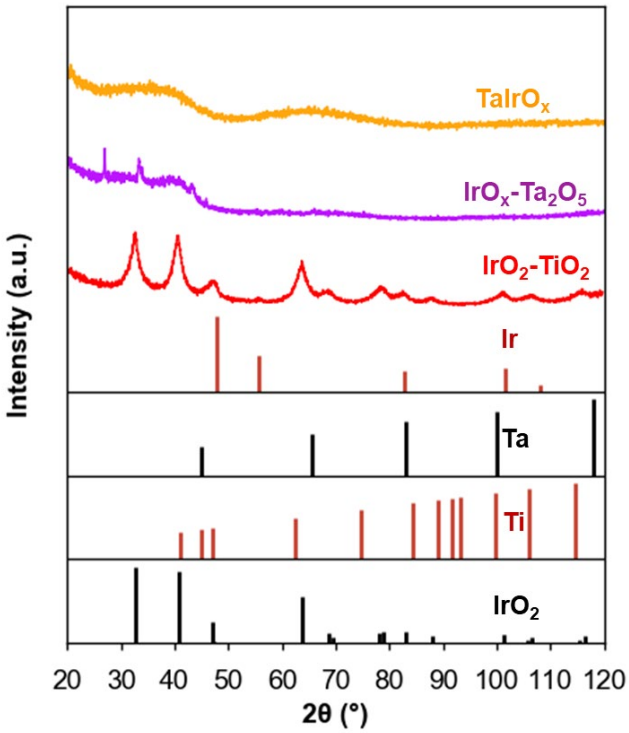

Figure 4-2: X-ray diffractograms of the synthesised IrO_x onto Ta_2O_5 (purple), $TaIrO_x$ (orange) and commercial IrO_2-TiO_2 (red). Maroon lines represent metallic iridium and tantalum, black lines iridium oxide and metallic titanium XRD reflexes.

4.3 EDX analysis of IrO_x nanomaterials

4.3.1 EDX analysis of IrO_x nanomaterials using different oxidising reagents and post-treatment

The elemental composition of the iridium oxides synthesised was assessed using EDX to determine the iridium loading or any impurities observed in each nanomaterial. Table 4.2 shows the first indication that a discrepancy is apparent between the samples and the corresponding EDX spectra are presented in Appendix A. The elemental compositions are reported in weight percentage for standard deviations, based on averaging of three readings.

According to the EDX spectra shown in Appendix 1, all nanomaterials show a carbon signal at 0.277 keV, this is due to using carbon tape as a sample holder. This could be due to the interactions between the carbon tape and the electron beam, or air exposure and a thin layer of carbon can also form on a sample's surface during handling or preparation. For these reasons, the carbon EDX weight percentage was not quantified in Table 4.2.

The analysis of the composition revealed that iridium and oxygen are the primary elements, and a small quantity of sodium was detected ± 4 wt% in some materials which can be a contributing factor in the XRD peak 23° explained in section 4.2.1. The commercial sample has high iridium content compared to the prepared materials. The $IrO_{x-(Ba)}$ sample shows a higher iridium weight percentage compared to the $IrO_{x-(Na)}$ sample. Sodium peroxide is a stronger oxidising agent and is more effective when it comes to releasing reactive oxygen species due to its ability to decompose quickly compared to barium peroxide.

Table 4-2: EDX elemental composition (wt.%) with standard deviation for the in-house synthesised iridium oxide catalysts and commercial TKK.

Sample ID	Oxidising agent/ cooling method	EDX elemental composition			
		Ir (wt.%)	O (wt.%)	Na / Ba (wt.%)	Cl (wt.%)
$IrO_{x-(Na)}$	Sodium peroxide	61.4 ± 2.4	34.7 ± 2.8	2.00 ± 0.7	2.30 ± 0.1
$IrO_{x-(Ba)}$	Barium peroxide	74.4 ± 6.5	21.0 ± 6.5	Ba = 0.98 ± 0.4	3.62 ± 0.7
TKK	Benchmark	74.7 ± 6.4	25.2 ± 6.4	-	0.07 ± 0.2
$IrO_{x-(Na)-(S)}$	Cooled in the furnace for 2 hrs then poured $N_{2(l)}$	65.0 ± 4.0	32.2 ± 4.0	2.80 ± 0.1	-
$IrO_{x-(Na)-(R)}$	Liquid N_2	69.3 ± 2.3	26.1 ± 2.3	4.60 ± 0.4	-
$IrO_{x-(Na)-(Q)}$	Dry Ice - (CO_2)	70.9 ± 8.0	29.1 ± 8.5	-	0.98 ± 0.6

For further optimising the synthesis process sodium peroxide was preferred as an oxidant agent due to its high efficiency and ability to facilitate oxidation. In contrast to the EDX results using

the different cooling post-treatment methods, the air-cooled has more oxygen content. According to the results obtained shown in Table 4.2, all materials have different iridium content increasing order $IrO_{x\text{-}(Na)\text{-}(S),}$ followed by $IrO_{x\text{-}(Na)\text{-}(R),}$ and the highest $IrO_{x\text{-}(Na)\text{-}(Q)}$. According to literature (Siracusano et al., 2017; Labi et al., 2021, Zhao et al., 2022 and Gao et al., 2019), the prolonged cooling of a material can help facilitate the oxidation of IrO_x, which can then be turned into its fully stable state. The material has enough time to incorporate oxygen, which helps minimise the oxygen vacancies. On the other hand, the rapid cooling of a material can prevent oxygen from diffusion into the surrounding materials, which can preserve the oxygen vacancies or partially reduced states. In addition, oxygen vacancies can serve as active sites for OER.

4.3.2 EDX analysis of IrO_x nanomaterials of the mixed-metal and supported material

Table 4.3 shows the elemental composition expressed in weight percentage (wt.%), indicating the relative proportion of each element in the IrO_x-based nanomaterials. The corresponding EDX spectra are presented in Appendix A. According to obtained EDX results, IrO_2-TiO_2 has the highest Ir loading weight percentage in decreasing order followed by $TaIrO_x$ and the lowest IrO_x-Ta_2O_5. The EDX analysis of the $TaIrO_x$ sample revealed iridium and oxygen as the primary elements. The presence of sodium was also detected, which is due to the sodium iridates observed and discussed in Chapter 4.2 Section 4.2.1 (Krizan et al., 2014). The $TaIrO_x$ material has a high Ir and less Ta weight percentage content. According to literature by Smolik et al., 2000, high temperatures such as 700 °C can cause tantalum pentoxide and other similar species to partially volatilise, decreasing the Ta content. In comparison, the IrO_x-Ta_2O_5 sample has higher Ta and Ir content.

The low weight percentage of titanium in the EDX analysis of the IrO_2-TiO_2 sample can be attributed to the peaks overlaps in the of iridium and titanium making it difficult to distinguish between them (Van der Merwe et al., 2023 and Harvey et al., 2024). The ability to analyse peak overlaps in energy dispersion spectroscopy has typically been a challenge. The Transmission electron microscopy mapping will be used to quantify the elemental composition of the IrO_2-TiO_2 sample.

Table 4-3: EDX elemental composition (wt.%) with standard deviation for the in-house synthesised tantalum-iridium oxide catalyst and commercial iridium dioxide on titanium pentoxide.

Sample ID	EDX elemental composition				
	Ir (wt.%)	**O (wt.%)**	**Ta (wt.%)**	**Na (wt.%)**	**Ti (wt.%)**
$TaIrO_x$	61.8 ± 0.9	27.9 ± 0.8	8.50 ± 1.0	1.80 ± 0.12	-
IrO_x-Ta_2O_5	29.3 ± 1.8	21.8 ± 0.2	43.9 ± 0.7	2.00 ± 0.12	-
IrO_2-TiO_2	75.3 ± 0.5	23.9 ± 0.1	-	-	0.8 ± 0.5

4.4 Morphological, particle size distribution and surface area analysis

4.4.1 Morphology and average TEM nanoparticle sizes of the IrO_x nanomaterials using different oxidising reagents and post-treatment

The TEM analysis and average particle size distribution for all the nanomaterials are shown in Figure 4.3 and were measured at 20 nm magnification. Ferret diameter was used to analyse the particle size and determine the corresponding distribution histograms, using on average ± 150 nanoparticles.

The TEM analysis was used to confirm the morphology and particle size for each nanomaterial. The TEM images of IrO_x produced by varying two oxidising agents and commercial nanomaterials are represented in Figure 4.3 (a, b & c) and corresponding histograms (a', b', & c'). The $IrO_{x\text{-}(Na)}$ and commercial nanomaterials show visible particles with an average of ± 2.74 nm and ± 1.98 nm, respectively. The commercial sample is likely to be more active due to the smaller particles size compared to $IrO_{x\text{-}(Na)}$. The $IrO_{x\text{-}(Ba)}$, morphology is more flake-like with an average dimension of each flake is about ± 50 -150 nm, while visible particles are highly agglomerated and difficult to differentiate between singular particles. Similar nanoflakes were found in a study conducted by Huang et al., 2019. They concluded that the compact and uniform MoS_2 nanoflakes could increase the surface area of active sites and enhance the efficiency of the OER process. However, porosity plays a significant role in the electrocatalyst's OER activity due to several factors such as surface area, mass transport,

structural stability and promoting electrolyte penetration. It can be challenging to predict the exact OER activity of IrO_x based on the nanoparticle or nanoflake structure and composition.

The TEM results using different cooling post-treatment are presented in Figure 4.3 presents (d, e, & f) with corresponding histograms (d,' e,' & f') illustrating the particle size distribution. All the nanomaterials have similar distorted spherical shapes with an average particle size 1–2.5 nm. These samples have smaller particle sizes compared to the air-cooled sample shown in Figure 4.3 (a).

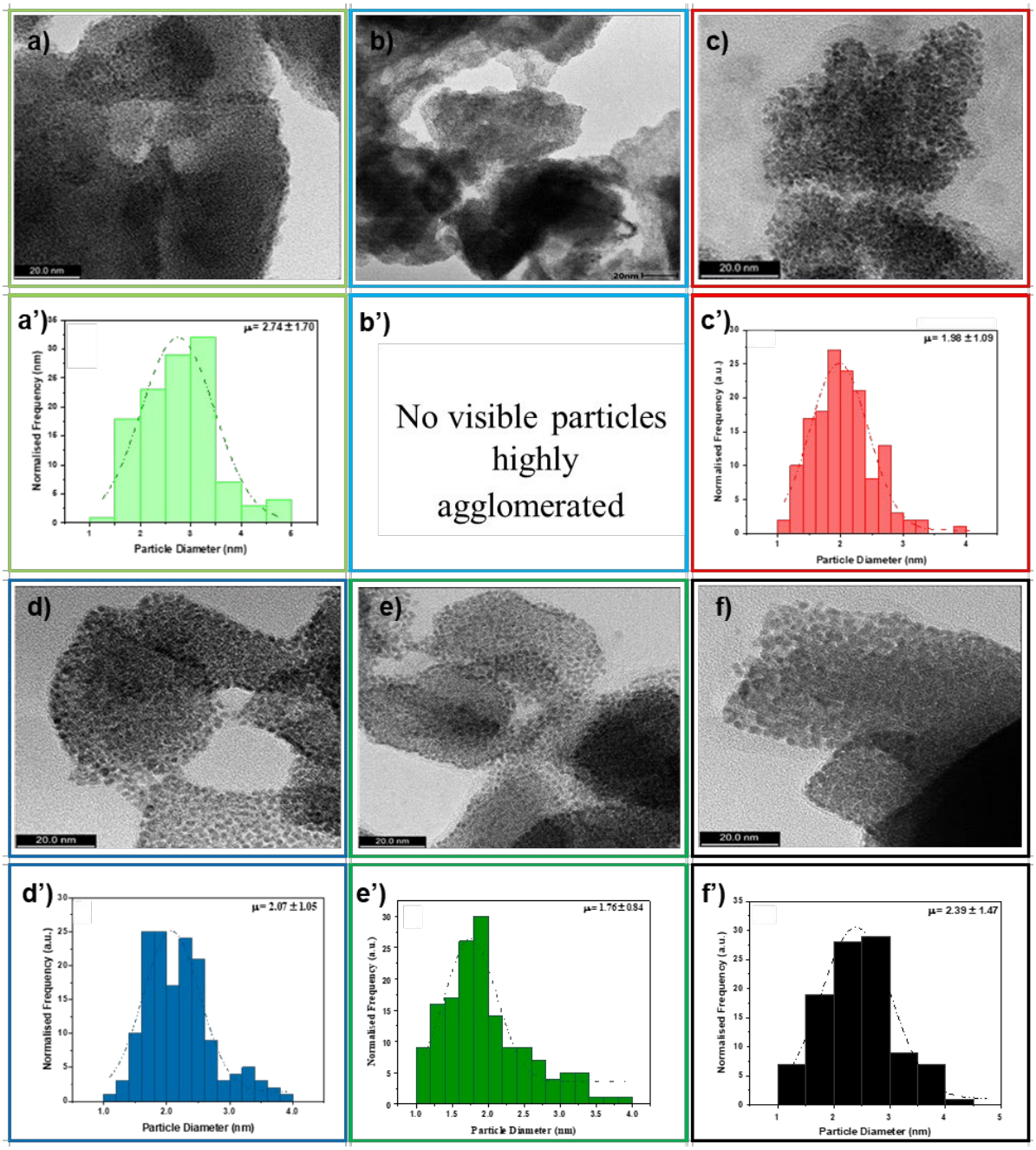

**SA – Surface area*

Figure 4-3: TEM micrograms and particle size distribution respectively for the synthesised IrO_x nanomaterials using sodium peroxide $IrO_{x\text{-}(Na)}$ (a), vs barium peroxide $IrO_{x\text{-}(Ba)}$ (b), commercial benchmark TKK (c), $IrO_{x\text{-}(Na)\text{-}(S)}$ (d), $IrO_{x\text{-}(Na)\text{-}(R)}$ (e), and $IrO_{x\text{-}(Na)\text{-}(Q)}$ (f) represents the IrO_x nanomaterials using various cooling methods.

4.4.2 Morphology and average TEM nanoparticle sizes of the IrO_x nanomaterials IrO_x nanomaterials of the mixed-metal and supported material

The morphology of the synthesised $TaIrO_x$, IrO_x-Ta_2O_5 and IrO_2-TiO_2 nanomaterial are shown in Figures 4.4 (a, b & c), respectively and the corresponding histogram Figure (a' & b'). As seen in Figure 4.4 (a & b), the iridium nanoparticles appear in black and the Ta_2O_5 phase exhibits a lighter grey. The IrO_x-Ta_2O_5 microgram shows uniformly dispersed Ir nanoparticles agglomerated in some regions on the Ta_2O_5 support with an estimated average visible particle of 4.59 nm. A similar particle size was obtained in the study conducted by Felix et al., 2019 using the Adam Fusion method. The $TaIrO_x$ nanomaterial is very agglomerated with no visible particle size, so it was not feasible to plot the distribution sizes of particles. The measured average dimension of agglomerated clumps is about 20.5 ± 0.84 nm. The EDS mapping of the IrO_2-TiO_2 sample was performed to determine Ti's presence. The EDX spectra was not provided and this made it challenging to differentiate between the peaks of Ir and Ti in SEM-EDS. The Ir (red) and Ti (blue) elements overlap to form purple regions and there are no visible particles.

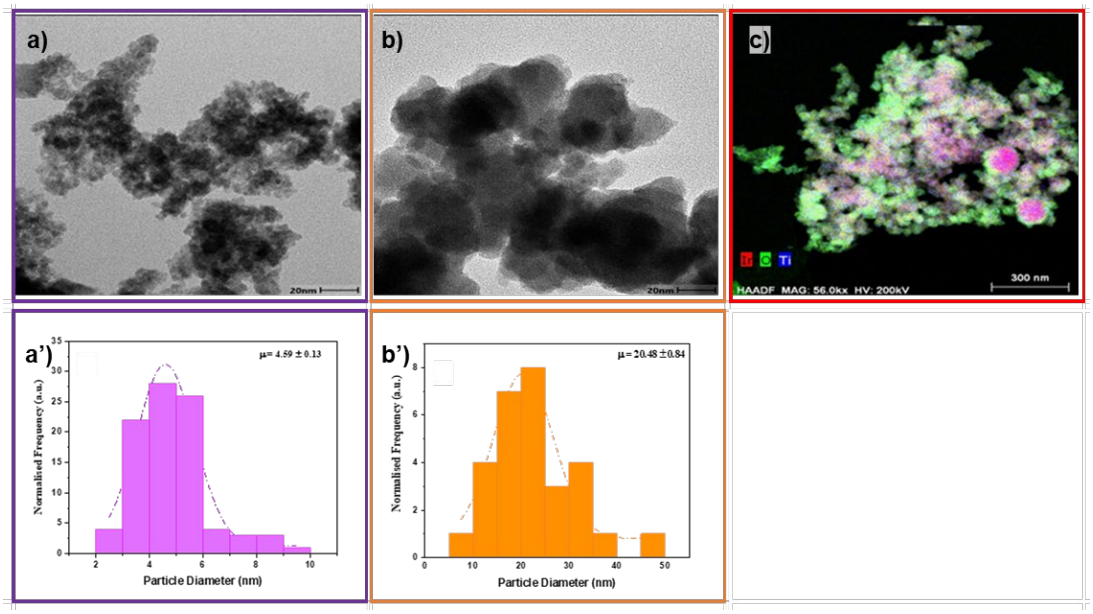

**SA – Surface area*

Figure 4-4: TEM micrograms and particle size distribution respectively of the nanomaterials (a)-(a'), IrO_x-Ta_2O_5(a)-(a'), $TaIrO_x$ (b)-(b'), and TEM mapping HAADF for IrO_2-TiO_2 (c).

4.4.3 BET surface area analysis and average TEM nanoparticle sizes of the different oxidising reagents, post treatments and mixed-metal and supported material

The specific surface areas of the nanomaterials were measured by using the BET surface area analysis. Surface area and particle size have an inverse relationship, high surface area is obtained from samples with small particle sizes. Table 4.4 shows the BET surface area, pore volume and pore size results for each material and the corresponding isotherm graph and pore distribution graphs are shown in Appendix B. A higher BET surface area typically indicates better dispersion of active components, as seen in Table 4.4, the commercial materials IrO_x-Ta_2O_5 have the highest surface area followed by IrOx TKK. In comparison with the in-house materials, the $IrO_{x\text{-}(Ba)}$ and $TaIrO_x$ nanomaterials have higher surface area. The $IrO_{x\text{-}(Na)\text{-}(R)}$ and $IrO_{x\text{-}(Na)\text{-}(S)}$ exhibit the lowest surface areas. Higher pore volume indicates higher capacity for gas adsorption, according to literature it benefits catalytic or adsorption applications. Referring to Table 4.4, $IrO_{x\text{-}(Na)\text{-}(R)}$ shows a remarkably higher pore volume compared to others and $IrO_{x\text{-}(Na)\text{-}(Q)}$ has the smallest pore volume.

In comparison to the pore size, $IrO_{x\text{-}(Na)\text{-}(R)}$ has the largest average pore size, likely indicating macroporosity or wide mesopores. Macroporosity generally results in lower surface areas but higher pore volumes (Baik et al., 2023). The IrO_x-Ta_2O_5 has the smallest pore size, consistent with more uniform mesoporosity. Mesopores provide a good balance between accessibility for larger molecules and surface reactivity (Baik et al., 2020). The synthesised materials were successfully made in comparison to the commercial materials. However, there is no clear correlation between particle size and the surface area in the nanomaterials. The TKK sample presents a more common correlation, where the higher surface area corresponds with smaller particle sizes (Rodríguez et al., 2012 & Rheinländer et.al., 2021). The average particle sizes of the cooling post-treatment method nanomaterials are estimated to be within the range of 1.7 to 2.4 nanometres. The supported materials IrO_x-Ta_2O_5 and IrO_2-TiO_2 have higher surface areas in contrast with the unsupported $TaIrO_x$. Compared to supported catalysts, the surface area of mixed metal oxide materials is lower. This is because the active material is dispersed in the bulk rather than on the surface (Mabate et al., 2023 & Masliuk et al., 2024).

Table 4-4: BET surface area analysis and average TEM nanoparticle sizes of IrO_x nanomaterials.

Material	BET Surface Area (m^2/g)	Pore Volume (cm^3/g)	Pore Size (nm)	Particle size (nm)
$IrO_{x-(Na)}$	13.5	0.01	4.19	2.74
$IrO_{x-(Ba)}$	31.7	0.01	4.72	0.00
TKK	80.0	0.02	5.33	1.98
$IrO_{x-(Na)-(S)}$	10.2	0.01	5.04	2.07
$IrO_{x-(Na)-(R)}$	9.60	0.12	5.89	1.76
$IrO_{x-(Na)-(Q)}$	11.9	0.00	5.17	2.39
$TaIrO_x$	18.4	0.01	5.28	agglomerates 20.5
IrO_x-Ta_2O_5	89.8	0.02	3.25	4.59

4.5 X-ray photoelectron spectroscopy (XPS)

To gain a deeper understanding of each nanomaterial surface chemistry and how the various synthesis techniques affected their nature, all nanomaterials were subjected to X-ray Photoelectron Spectroscopy (XPS) measurements. According to the XPS survey spectra data provided in Appendix C, the iridium Ir 4f peaks confirm the presence of Ir-based oxides in the nanomaterials and the oxidation states likely include a mixture of Ir^{3+} and Ir^{4+}, which can influence the catalytic properties. The O 1s peak shows contributions from lattice oxygen (metal-oxide bonds) and possibly adsorbed oxygen or hydroxyl species, similar results were obtained in the literature (Hoffman et al., 2023; Labi et al., 2021 & Tan et al., 2019). Variations in O 1s binding energy suggest differences in the chemical environment of oxygen in the materials.

Tantalum (Ta 4f and 4d) peaks indicate the presence of Ta_2O_5, confirming successful deposition or incorporation. The Ta^{5+} is the dominant oxidation state, consistent with tantalum pentoxide (Baik et al., 2023). Na peaks (Na 1s) confirm the presence of residual sodium, potentially from precursors or synthesis processes. The intensity suggests sodium contamination varies across samples. Chlorine Cl 2p peaks indicate residual chlorides, likely from precursors such as $TaCl_5$ or from washing 0.1 M HCl. This may suggest incomplete

calcination or washing. Higher ratios of Ir^{4+}/Ir^{3+} may suggest better catalytic performance in oxidation reactions. Residual Cl or Na may impact stability or performance, requiring additional processing to reduce contamination.

4.5.1 Analysis of the XPS narrow scans and Ir 4f components

Figure 4.5 reveals the spectra of Ir 4f, which show the characteristics of an iridium species found on the surface of synthesised materials. According to the analysis of the XPS narrow scans (Figure 4.5 a) the signal intensity of the sample that was prepared with barium peroxide is higher than the signal intensity of the sample that was made with sodium peroxide oxidizing agents. According to Saveleva et al., 2018 and Pfeifer et al., 2015, the intensity of the photoemission of an Ir 4f/7/2 or 4f/5/2 electron rises at 61.8 and 64.8 eV binding energy in IrO_2, respectively. The main peaks of $IrO_{x\text{-}(Na)}$ are in the Ir 4f spectrums intensity range between 61.2 and 64.3 eV. The shift to low binding energies suggests that samples may undergo varying oxidation states, with Ir (IV) being more prevalent in this instance. In contrast, the $IrO_{x\text{-}(Ba)}$ sample exhibits higher binding energy peaks at 62.0 eV and 65.1.0 eV, which is prevalent in the Ir (III) oxidation state. A pure rutile structure is usually characterised by an Ir 4f/7/2 peak at 61.8 eV. However, the peak at 62.5 eV could indicate that the surface has a hydrated structure for example IrO_2*H_2O (Siracusano et al., 2017).

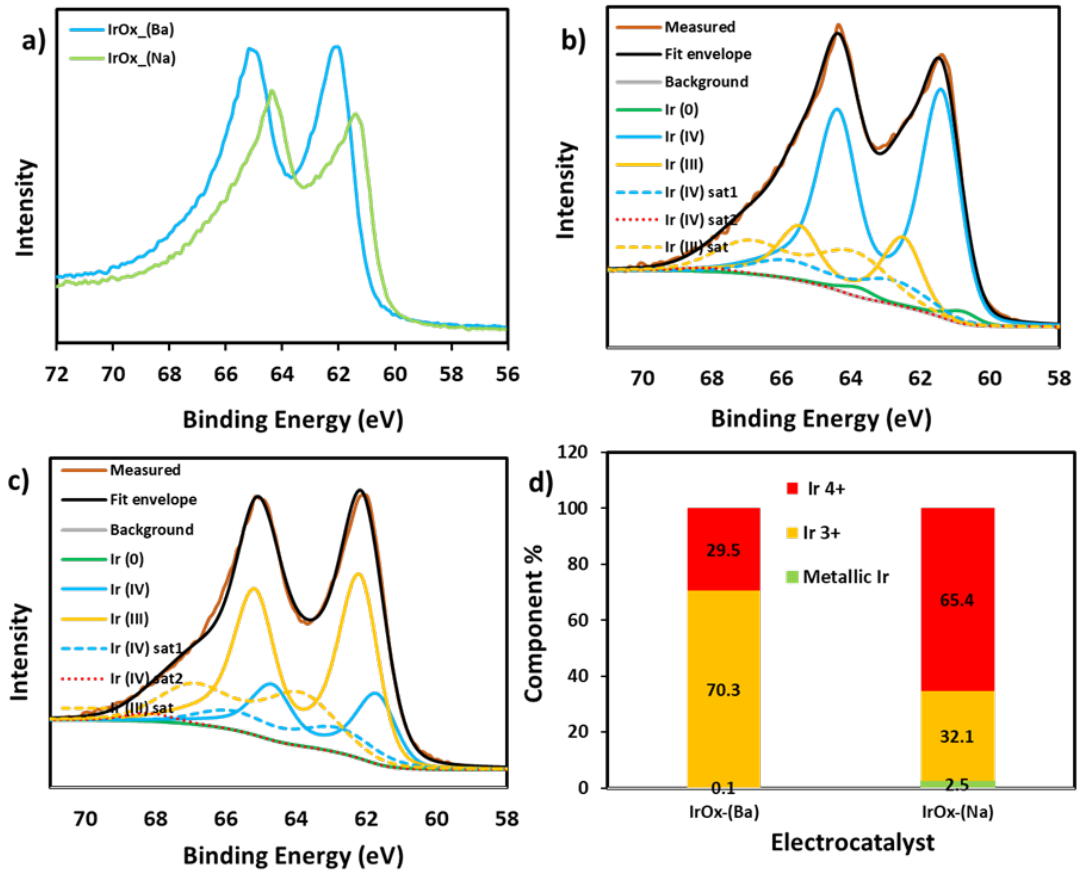

Figure 4-5: X-ray photoelectron spectroscopy raw data narrow scans showing the Ir 4f region (a), the curve-fitted spectra for $IrO_{x-(Na)}$ (b), curve-fitted spectra $IrO_{x-(Ba)}$ (c) and component contributions for both samples (d).

The Ir 4f peak shift observed in both samples could be due to the contributions of different oxidation states found in these samples. Although it is not feasible to draw a quantitative conclusion from raw data. The curve-fitting spectrum was used to provide additional information about a sample's chemical nature. Figure 4.5 b & c shows the curve fitting procedure for the IrO_x nanomaterials which is described in Chapter 3 section 3.5.3. The Ir 4f spectrum curve fitting was conducted according to the approach used by Rajan et al.,2020. It is in line with the works of Pfeifer 2016; Yu et al 2018; and Hoffman 2023. The Ir (IV), Ir(III), and metallic Ir were identified as having 61 eV, 62 eV, and 60 eV, respectively. The satellite peaks for Ir (IV) were observed at 62 eV and 67 eV, while those for Ir (III) were at 63 eV. According to (Figure 4.3 d), there was full Ir to IrO_x conversion during the synthesis step for the $IrO_{x-(Ba)}$ sample since the metallic iridium detection was less than 0.1%. In contrast, to $IrO_{x-(Na)}$ sample with an approximate ± 97.5% conversion due to the 2.5% metallic iridium detected.

The quantification of the Ir 4f spectrum of the prepared sample showed that the $IrO_{x-(Ba)}$ dominating Ir species was Ir (III) with a 70.3% contribution, whereas the remaining contribution comes from Ir (IV). The $IrO_{x-(Na)}$ sample predominated in an Ir (IV) oxidation state with 65.4% with a secondary contribution for Ir (III) of 32.1% and the remaining small contribution of 2.5% Ir (0). The quantification of the Ir 4f spectrum of the nanomaterials prepared using different cooling post-treatment methods is presented in Figure 4.6.

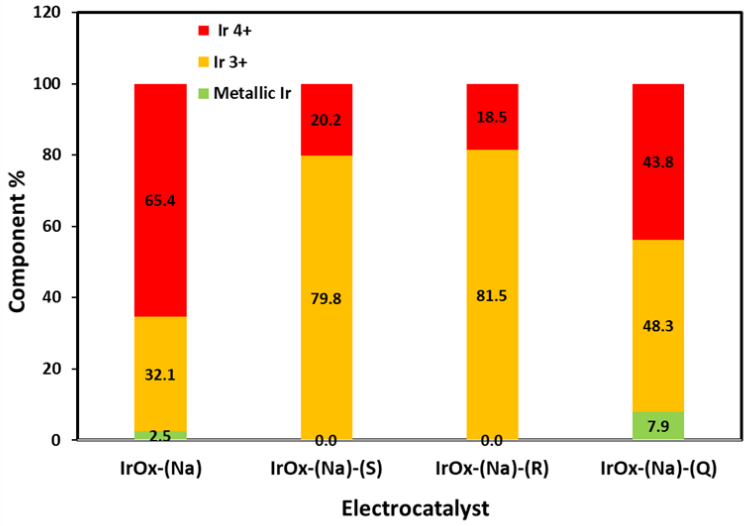

Figure 4-6: X-ray photoelectron spectroscopy for the component contributions of the air-cooled sample $IrO_{x-(Na)}$ and cooling methods samples $IrO_{x-(Na)-S, R, Q}$.

The corresponding raw data narrow scans and curve-fitted spectra are shown in Figure 4.7. The $IrO_{x-(Na)-(S)}$ and $IrO_{x-(Na)-(R)}$ samples are predominant in an Ir (III) oxidation state with a contribution of ± 80% and Ir (IV) of ± 20%, and no metallic iridium percentage was detected. The $IrO_{x-(Na)-(Q)}$ sample was not fully converted from Ir to IrO_x, due to metallic iridium contribution of 7.9 %. The Ir (III) and Ir (IV) oxidation states contributed 48.3% and 43.8% respectively, suggesting near equal distribution of Ir (III) and Ir (IV) oxidation states. All samples with the Ir (III) oxidation state are likely to be more active compared to that of Ir (IV). According to Vélez, 2016 and Cherevko 2016, Ir^{4+} is regarded as the most stable type of iridium and Ir^{3+} is more active and likely to undergo dissolution in iridium oxide materials.

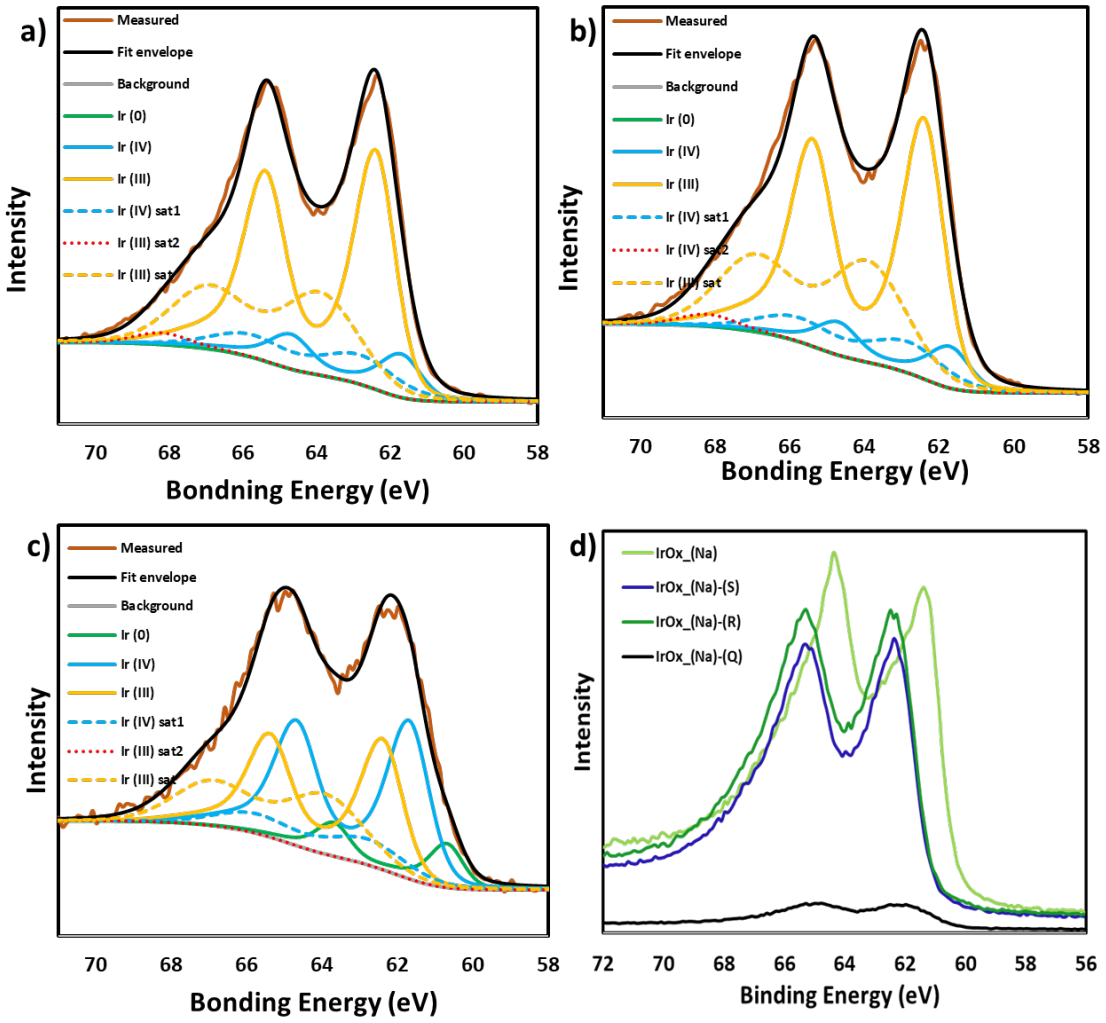

Figure 4-7: Curve fitted XPS spectra for $IrO_{x\text{-}(Na)\text{-}(s)}$ (a), $IrO_{x\text{-}(Na)\text{-}(R)}$, (b), and $IrO_{x\text{-}(Na)\text{-}(Q)}$ (c). Raw data XPS narrow scans for $IrO_{x\text{-}(Na)}$ (olive green), $IrO_{x\text{-}(Na)\text{-}(s)}$ (blue), $IrO_{x\text{-}(Na)\text{-}(R)}$, (dark green), $IrO_{x\text{-}(Na)\text{-}(Q)}$ (black) (d).

4.5.2 Analysis of the XPS narrow scans and Ir/Ta 4f components

According to Figure 4.8 (a), the signal intensity of IrO_x-Ta_2O_5 was higher than the signal intensity of $TaIrO_x$. The doublet due to spin-orbit splitting Ir 4F/7/2 or 4F/5/2 for IrO_x-Ta_2O_5 are around 62.3 and 65.3 eV and $TaIrO_x$ at 62.1 eV and 65.0 eV. The intensity of the photoemission of an Ir 4f/7/2 or 4f/5/2 electron rises at 61.8 and 64.8 eV binding energy in IrO_2 respectively (Saveleva et al., 2018 and Pfeifer et al., 2015). The shift in the Ir 4f peaks in XPS to higher binding energies is often linked to the oxidation state of Ir (III) and lower binding energy associated with the Ir (V) oxidation state (Tan et al., 2019 & Regmi et al., 2020).

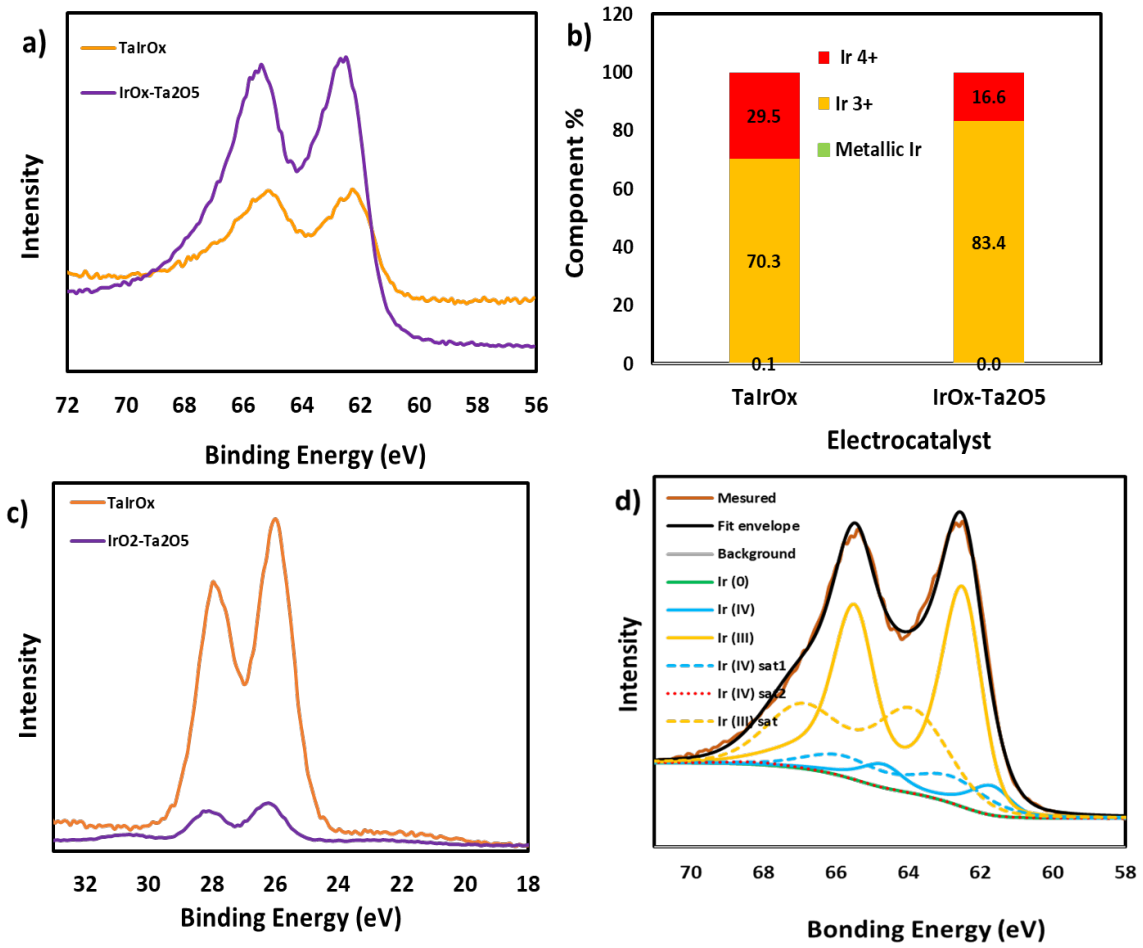

Figure 4-8: X-ray photoelectron spectroscopy raw data narrow scans showing the Ir 4f region (a), component contributions for both samples (b), Ta 4f (c) and curve-fitted spectra (d).

Peak deconvolution was performed using an established doublet fit, as shown in Figure 4.8 (a & c), and described in detail in the experimental section in Chapter 3 section 3.5.3. The quantification of the Ir 4f spectrum of the nanomaterials is presented in Figure 4.8 (b). The curve-fitting technique was used to determine the oxidation state of the two nanomaterials surface, the corresponding curve-fitted spectra are shown in Figure 4.8 (d). The IrO_x-Ta_2O_5 and $TaIrO_x$ samples show a preference for the Ir (III) oxidation state. The former has a significant contribution of over 80%, while the latter accounts for over 70%. The supported sample is therefore more likely to be active compared to the mixed metal oxide. On the other hand, $TaIrO_x$ is likely to be more stable due to a higher percentage of Ir (IV) oxidation state. Both samples were fully converted into iridium oxide as no metallic iridium was quantified. Figure 4.8 c shows the two narrow XPS spectra of Ta 4f with two peaks located at 28.0 and

26.0 eV correlating to Ta 4f5/2 and Ta 4f7/2 respectively with energy separation of 1.9 eV. This occurs due to the spin-orbit coupling Ta's oxidation states are attributed to Ta 4f 5/2 and Ta 4f7/2 similar results were obtained in a study conducted by (McLellan et al., 2023, and Atanassova et al., 1998). The peaks of Ta 4f are assigned to Ta ions within the 5^+ oxidation state such as Ta_2O_5 (Rong et al., 2023 & Baik et al., 2023).

4.6 References

Ali, A., Chiang, Y. W., & Santos, R. M. (2022). X-Ray Diffraction Techniques for Mineral Characterization: A Review for Engineers of the Fundamentals, Applications, and Research Directions. *Minerals*, *12*(2). https://doi.org/10.3390/min12020205.

Baik, C., Cho, J., Cha, J. I., Cho, Y., Jang, S. S., & Pak, C. (2023). Electron-rich Ir nanostructure supported on mesoporous Ta_2O_5 for enhanced activity and stability of oxygen evolution reaction. *Journal of Power Sources*, *575*. https://doi.org/10.1016/j.jpowsour.2023.233174.

Baik, C., Lee, S. W., & Pak, C. (2020). Control of the pore size distribution inside the RuO_2 catalyst by using silica nanosphere particles for highly efficient water electrolysis. *Microporous and Mesoporous Materials*, *309*. https://doi.org/10.1016/j.micromeso.2020.110567.

Czioska, S., Boubnov, A., Escalera-López, D., Geppert, J., Zagalskaya, A., Röse, P., Saraçi, E., Alexandrov, V., Krewer, U., Cherevko, S., & Grunwaldt, J. D. (2021). Increased Ir-Ir Interaction in Iridium Oxide during the Oxygen Evolution Reaction at High Potentials Probed by Operando Spectroscopy. *ACS Catalysis*, *11*(15), 10043–10057. https://doi.org/10.1021/acscatal.1c02074.

Felix, C., Bladergroen, B. J., Linkov, V., Pollet, B. G., & Pasupathi, S. (2019). Ex-situ electrochemical characterization of IrO_2 synthesized by a modified Adams fusion method for the oxygen evolution reaction. *Catalysts*, *9*(4). https://doi.org/10.3390/catal9040318.

Felix, C., Pasupathi, S., Bladergroen, B. J., Felix, C., Maiyalagan, T., Pasupathi, S., Bladergroen, B., & Linkov, V. (2012). Synthesis, Characterisation and Evaluation of IrO_2 Based Binary Metal Oxide Electrocatalysts for Oxygen Evolution Reaction Hydrogen and Fuel cell View project Energy Storage View project Synthesis, Characterisation and Evaluation of

IrO_2 Based Binary Metal Oxide Electrocatalysts for Oxygen Evolution Reaction. In *Article in International Journal of Electrochemical Science* (Vol. 7). www.electrochemsci.org.

Gao, J., Xu, C. Q., Hung, S. F., Liu, W., Cai, W., Zeng, Z., Jia, C., Chen, H. M., Xiao, H., Li, J., Huang, Y., & Liu, B. (2019). Breaking Long-Range Order in Iridium Oxide by Alkali Ion for Efficient Water Oxidation. *Journal of the American Chemical Society*, *141*(7), 3014–3023. https://doi.org/10.1021/jacs.8b11456.

Hoffman, J. A., Rajan, Z. S. H. S., Susac, D., Matoetoe, M. C., & Mohamed, R. (2023). Influence of Support Physicochemical Properties on the Oxygen Evolution Reaction Performance of ITO-Supported IrOx Nanoparticles. *Journal of Physical Chemistry C*, *127*(2), 894–906. https://doi.org/10.1021/acs.jpcc.2c06501.

Krizan, J. W., Roudebush, J. H., Fox, G. M., & Cava, R. J. (2014). The chemical instability of Na_2IrO_3 in air. *Materials Research Bulletin*, *52*, 162–166. https://doi.org/10.1016/j.materresbull.2014.01.021.

Monshi, A., Foroughi, M. R., & Monshi, M. R. (2012). Modified Scherrer Equation to Estimate More Accurately Nano-Crystallite Size Using XRD. *World Journal of Nano Science and Engineering*, *02*(03), 154–160. https://doi.org/10.4236/wjnse.2012.23020

Labi, T., van Schalkwyk, F., Andersen, S. M., Morgen, P., Ray, S. C., & Chamier, J. (2021). Increasing fuel cell durability during prolonged and intermittent fuel starvation using supported IrOx. *Journal of Power Sources*, *490*. https://doi.org/10.1016/j.jpowsour.2021.229568.

Pfeifer, V., Jones, T. E., & Velasco, J. J. (2015). *Supplementary Information to The Electronic Structure of Iridium Oxide Electrodes Active in Water Splitting*.

Rasten, E. (2001). Electrocatalysis in water electrolysis with solid polymer electrolyte, PhD thesis, Norwegian University of Science and Technology.

Siracusano, S., Baglio, V., Grigoriev, S. A., Merlo, L., Fateev, V. N., & Aricò, A. S. (2017). The influence of iridium chemical oxidation state on the performance and durability of oxygen evolution catalysts in PEM electrolysis. *Journal of Power Sources*, *366*, 105–114. https://doi.org/10.1016/j.jpowsour.2017.09.020

Smolik, G. R., Petti, D. A., Sharpe, J. P., & Schuetz, S. T. (2000). Oxidation and Volatilization from Tantalum Alloy T-222 During Air Exposure. https://doi.org/10.2172/776430.

Tan, X., Shen, J., Semagina, N., & Secanell, M. (2019). Decoupling structure-sensitive deactivation mechanisms of Ir/IrOx electrocatalysts toward oxygen evolution reaction. *Journal of Catalysis*, *371*, 57–70. https://doi.org/10.1016/j.jcat.2019.01.018.

Labi, T., van Schalkwyk, F., Andersen, S. M., Morgen, P., Ray, S. C., & Chamier, J. (2021). Increasing fuel cell durability during prolonged and intermittent fuel starvation using supported IrOx. *Journal of Power Sources*, *490*. https://doi.org/10.1016/j.jpowsour.2021.229568Willinger, E., Massué, C., Schlögl, R., & Willinger, M. G. (2017). Identifying Key Structural Features of IrOx Water Splitting Catalysts. *Journal of the American Chemical Society*, *139*(34), 12093–12101. https://doi.org/10.1021/jacs.7b07079.

Chapter 5: IRIDIUM-BASED ELECTROCATALYSTS – ELECTROCHEMICAL PROPERTIES

In this chapter, the development of an understanding of the behaviour of the electrochemical performance of the prepared iridium oxide nanomaterials using two different oxidising agents, the three cooling post-treatments, mixed-metal and supported materials. The effective electrocatalyst is compared with those IrOx or Ta-IrOx electrocatalysts in recent publications.

5.1 Cyclic voltammetry (CV): surface oxide analysis

5.1.1 IrO_x nanomaterials using different oxidising reagents and post-treatment

The electrochemical properties of the IrO_x nanomaterials were investigated using a three-electrode electrochemical cell and the analysis methods. The cyclic voltammetry for each sample was done in triplicates and the voltammograms are presented in Figure 5.1. The information contained within the CV of IrO_x is used to analyse the oxidation and reduction processes that occur at the electrode's surface, which is typically regarded as an electrochemical function of the applied potential. In this study, the cyclic voltammetry analysis was performed to determine the surface oxidation states and the properties of the electrode surface for each IrO_x nanomaterials.

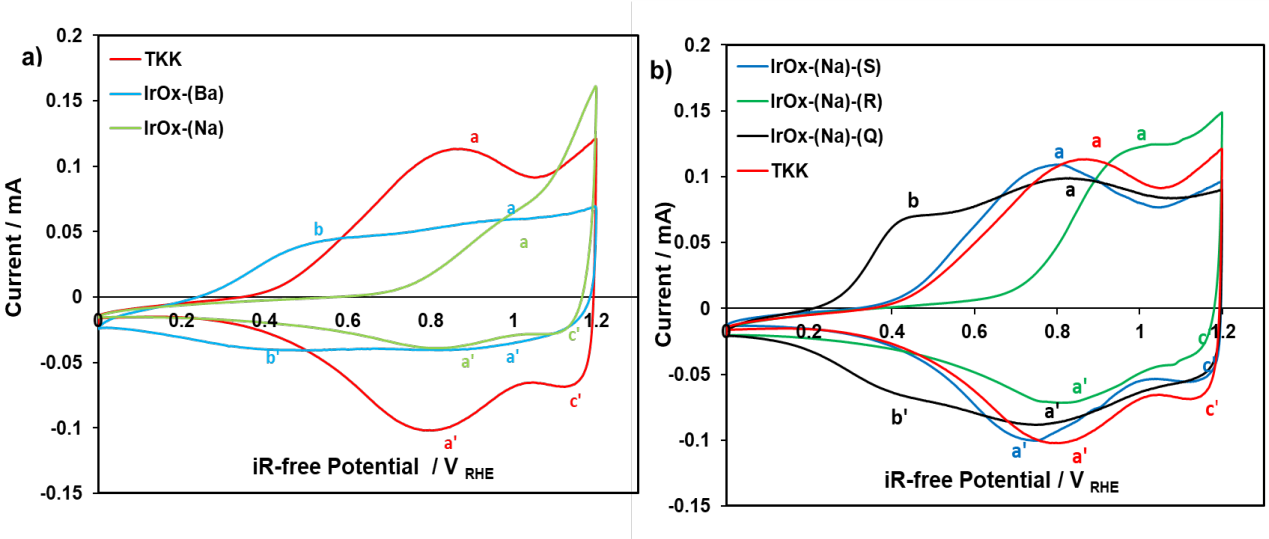

Figure 5-1: Cyclic voltammograms measured in potential window of 0 – 1.2 mV voltammograms in (a) are $IrO_{x\text{-}(Na)}$ (light green), $IrO_{x\text{-}(Ba)}$ (light blue), commercial

benchmark IrO_x TKK (red), and voltammograms shown in (b), $IrO_{x-(Na)-(S)}$ (blue), $IrO_{x-(Na)-(R)}$ (green), and $IrO_{x-(Na)-(Q)}$ (black), at 20 $mV.s^{-1}$ in 0.1 M $HClO_4$ under Argon saturation.

Figure 5.1 (a) shows the surface oxidation states of the IrO_x nanomaterials, and all samples' illustrations to have active surface due to the visible redox peaks. The peak current density, measured during the anodic scan at 0.8 V to 0.95 V range, increased linearly with increasing Ir content for each nanomaterial (Casella et al., 2015). As previously learned from the EDS data all the nanomaterials exhibit varied Ir loading with the highest being the TKK and the lowest being $IrO_{x-(Na)}$ similar results were observed in a study conducted by Alia in 2016.

The broad and flat peaks in the CV suggest that IrO_x has a complex behaviour involving several oxidation states. The XPS results revealed that each sample exhibits a combination of both Ir^{3+} and Ir^{4+} oxidation states. This indicates that these materials can be reversibly switched between Ir^{3+} and Ir^{4+}states during an electrochemical cycle (Velasco-Vélez et al., 2021). The surface's heterogeneity can lead to various redox potentials, which can cause the CV peaks to broaden. The flatness of CV peak surfaces suggests that there is a significant amount of capacitance behaviour. This could be caused by the reversible desorption or adsorption of ions from the surface.

The TKK sample CV has three well-defined peaks in the potential range of 0.6 V to 1.2 V (vs. reference electrode). The two peaks labelled (a & a') are symmetrical to each other whilst peak c' is asymmetrical. A similar trend is observed for sample $IrO_{x-(Na)}$ CV, however, the two peaks (a & a') are asymmetrical. The $IrO_{x-(Ba)}$ CV, shows flat four peaks in the oxidation-reduction potential range 0.3 V and 1.1 V. All three samples exhibited the two redox peaks (a & a') in 0.4 V to 1.2 V potential range, this primary anodic and cathodic pair is assigned to the Ir^{III} oxide ⇆ Ir^{IV} oxide transition (Geiger et al., 2019, Steegstra et al., 2013 & Velasco-Vélez et al., 2021). Similar results were obtained by a study conducted by Tan 2019, and colleagues revealed the surface chemistry of TKK IrO_x is likely that of a quasi-amorphous hydrous iridium (III/IV) oxide/hydroxide phase. The $IrO_{x-(Ba)}$ material exhibits two least understood redox peaks labelled (b &b') at the lower potentials (0.5 V and 0.4 V) respectively. According to Birss, the phenomenon originates from the oxidation of Ir^{III} sites near the oxide-metal interface and the in-situ mass transformations have also revealed an extensive water exchange. The cathodic peak (c') is assigned to be one of the Ir^{IV} ⇆ Ir^{V-VI} redox couples, which overlaps the OER (Geiger et al., 2019 & Velasco-Vélez et al., 2021).

CVs for the nanomaterials cooling post-treatment methods are shown in Figure 5.1 (b). All the samples have clear surface-based redox reactions shown by anodic and cathodic peaks at different potentials. These are due to the amorphous nature attributed to the transition between $Ir^{(III)} \leftrightarrows Ir^{(IV)}$ which is characteristic of a hydrous a-$IrO(OH)_x$ & Velasco-Vélez et al., 2021 & Geiger et al., 2019). The CV shapes seen in Figures 5.1a and 5.1b exhibits similar shapes. The CV shape of the $IrO_{x\text{-}(Na)\text{-}(S)}$ sample corresponds to that of TKK, but the two (a & a') redox couples shift toward the lower potentials. The $IrO_{x\text{-}(Na)\text{-}(R)}$, $IrO_{x\text{-}(Na)}$ and TKK samples exhibit the same two cathodic peaks, however peak (a) is located at different potentials. The same CV shape is observed for $IrO_{x\text{-}(Ba)}$ and $IrO_{x\text{-}(Na)\text{-}(Q)}$. Different studies conducted by Zhao 2019 and Weber in 2019 revealed that certain hydroxyl groups can function as active sites for important OER reactants and intermediates. The presence in the environment of OH-species can influence the desorption and adsorption of reactants, which helps in the overall process of oxidation.

5.1.2 IrO_x nanomaterials IrO_x nanomaterials of the mixed-metal and supported material

Figure 5.2 shows three cyclic voltammograms, the $TaIrO_x$ catalyst shows an active surface due to the visible redox peaks labelled (a & a'). These are due to the amorphous nature attributed to the transition between $Ir^{(III)} \leftrightarrows$ and $Ir^{(IV)}$ which is characteristic of a hydrous a-$IrO(OH)_x$ (Velasco-Vélez et al., 2021 and Geiger et al., 2019). Similar results were observed in section 5.1.1 for the unsupported electrocatalysts, however, the $TaIrO_x$ catalyst does not exhibit the peak labelled (c) in Figure 5.2. Even though the catalysts exhibit an Ir^{3+} oxidation state and with the highest Ir the Ta content could hinder the electrochemical activity and conductivity of the material.

The IrO_2-TiO_2 catalyst has the lowest current when compared to the other two catalysts. This could be due to the crystallinity material revealed by XRD analysis. According to Stavrou et al., 2017 and Zhang et al., 2017, the smaller double-charging surface of titanium dioxide compared to Ta_2O_5 can be attributed to its higher dielectric constant, various band structures, and interface properties. The interaction between the electrolyte and the surface also plays a vital role in determining its thickness.

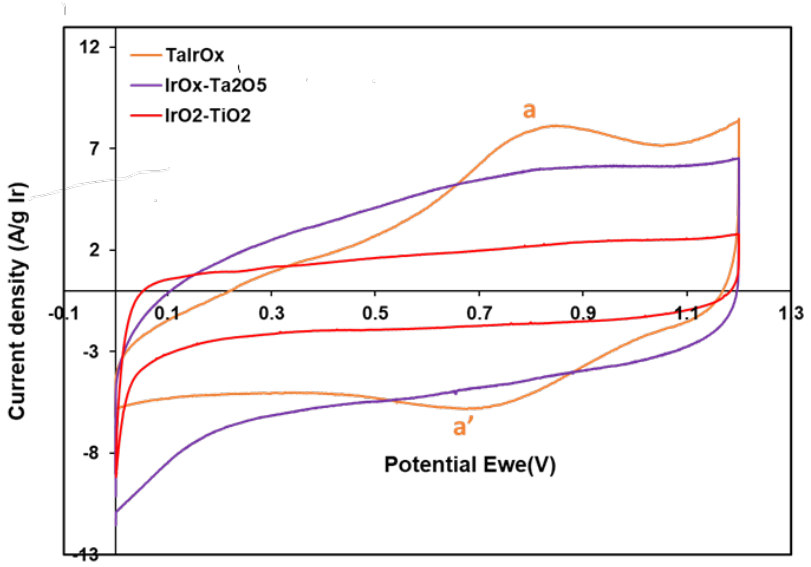

Figure 5-2: Cyclic voltammograms measured in the potential window of 0 – 1.2 mV (A) of the sample (orange) $TaIrO_x$, (purple) IrO_x-Ta_2O_5, and (red) commercial benchmark IrO_2-TiO_2 at 20 mV.s^{-1} in 0.1 M $HClO_4$ under Argon saturation.

5.2 Electrochemical active surface area of IrO_x nanomaterials

5.2.1 ECSA of IrO_x nanomaterials using different oxidising reagents and post-treatment

The ECSA refers to the catalyst surface area available for the OER. Unlike oxygen reduction reaction catalysts like Pt, it is more complicated to determine the ECSA of IrO_2-based catalysts as they are not active for proton adsorption/desorption nor CO_2 poisoning (Jackson et al., 2017 &Nagai et al., 2019). According to Vincent 2016, Labi 2019, McCrory 2013, and Zhao 2015, the OER catalyst ECSA estimation is calculated by considering the double-layer electrochemical capacitances of different materials and it is then normalised with the Ir loading of the catalyst. However, different ECSA methods were conducted by Duran et al., 2021 and Felix et al.,2019. According to Biesheuvel and Dykstra in 2018, the non-Faradaic potential refers to the region responsible for storing charge on a catalyst's surface. In this work, the ECSA of the electrocatalysts were estimated using the double-layer capacitance of the catalysts. The linear slope of the current vs scan rate, which is equivalent to twice the double-layer capacity (Cdl), was then used as the ECSA's representation. The same approach was used by the studies conducted by Merki et al., 2012; Song et al., 2014 & Lukowski et al., 2013. Figure 5.3 (a-d) shows the various CVs taken in the non-Faradaic region from 0.2 - 0.3 V at various scan rates for each of the electrocatalysts.

The electrochemical surface area of $IrO_{x\text{-}(Ba)}$ and $IrO_{x\text{-}(Na)\text{-}(Q)}$ samples was not established since a redox reaction occurred in the 0.25 V vs RHE region. The gradient values were used to represent the ECSA estimation values as seen in Figure 5.3 (e), the $IrO_{x\text{-}(Na)\text{-}(R)}$ sample has the highest gradient followed by TKK, $IrO_{x\text{-}(Na),}$ and the lowest $IrO_{x\text{-}(Na)\text{-}(S)}$. A high ECSA leads to improved performance in catalytic and while the presence of Ir^{3+} and Ir^{4+} influence the material's reactivity and stability. An increase in the number of surface atoms can interact with the electrolyte. This allows for a higher concentration of Ir^{3+}, which is more reactive than Ir^{4+} and can lead to better catalytic performance for reactions such as the OER. In contrast, the low ECSA and the Ir^{4+} oxidation states in IrO_x materials can indicate a more passively surface with reduced reactivity. This is unsuitable for high-activity applications and could be advantageous for those that require high resistance to corrosion and stability (Islam et al., 2024 & Galyamin et al., 2023).

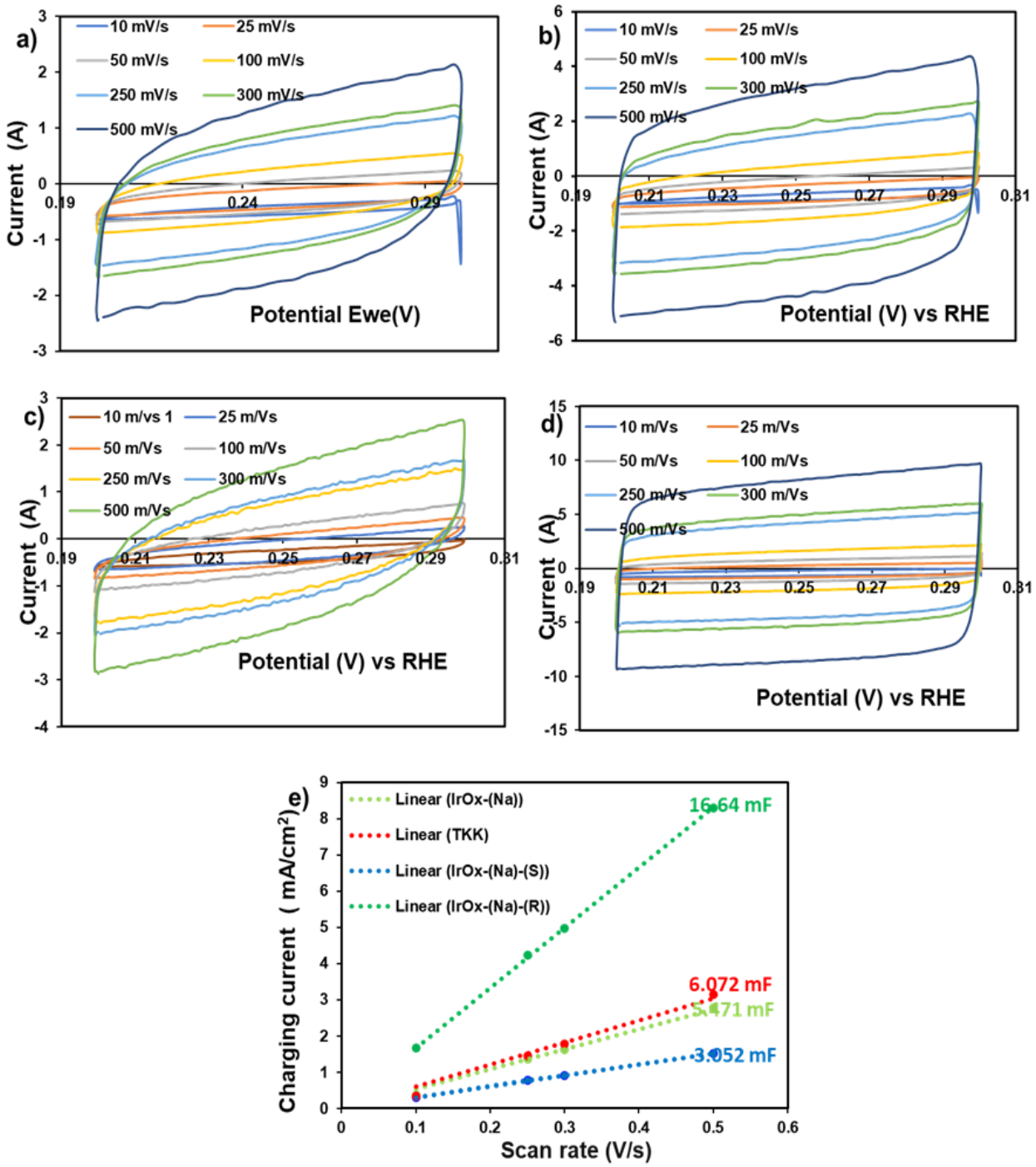

Figure 5-3: Non-Faradaic region for the cyclic voltammograms measured in potential window of 0.2 – 0.3 V of catalyst $IrO_{x-(Na)}$ (a), and commercial benchmark IrO_x TKK (b), $IrO_{x-(Na)-(S)}$ (c), $IrO_{x-(Na)-(R)}$ (d), and gradients values representing each nanomaterial electrochemical surface area estimation (e).

The ECSA cyclic voltammogram for the $IrO_{x-(Na)-(R)}$ sample and TKK have a box shape classified more as non-faradaic, while the $IrO_{x-(Na)-(S)}$ sample and $IrO_{x-(Na)}$ have a tilted shape.

According to the literature (Rajan et al., 2024; Agrawal et al., 2021 & Elgrishi et al., 2018) a cyclic voltammogram with a box-shaped or constant current over a range of potentials indicates that the process being studied has limited diffusion. This is because the reaction rate is restricted by the transport of products and species from the electrode surface to the other parts of the system. In ECSA determination, this suggests that the reaction's intrinsic kinetics are different from those of the transport of species. The shape of the cyclic voltammogram is usually caused by the presence of a porous or rough electrode surface. This characteristic leads to a large ECSA due to the limited reaction rate (Brownson et al., 2014 & Monteiro 2020). In the case of a tilted cyclic voltammogram, ECSA analysis can be interpreted as a sign that the reaction rate changes due to external influences (Agrawal et al., 2021). This could mean that there are multiple active regions with different surface characteristics.

5.2.2 ECSA of IrO_x nanomaterials of the mixed-metal and supported material

The ECSA for low-conductivity metal oxides and mixed metal oxides can be hard to determine due to various factors: Conductivity reduction in metal oxides can hinder the transfer of charge. This makes it difficult to determine the active surface area of an electrochemical process (Zhao et al., 2015). The double-layer capacitance of certain materials can be affected by differences in their electronic properties. This can make it difficult to differentiate between faradaic and capacitive currents as the particles would need to be the same size as well. The use of different electrochemical methods can lead to different ECSA values. For instance, methods such as impedance spectroscopy and cyclic voltammetry can provide different results due to the materials' surface characteristics and conductivity. The ECSA measurement process needs robust and reliable tools to be able to accommodate different morphologies and structures.

The ECSA for supported iridium oxide catalysts can be estimated using similar principles to those used for unsupported catalysts. However, the contribution of the support material to the overall behaviour of the catalyst should be considered carefully. Figure 5.4 (a, b & c) shows the various CVs taken in the non-Faradaic region from 0.2 - 0.3 V at various scan rates for each of the samples. The gradient measurements were used to represent the ECSA estimation as seen in Figure 5.4 (d), the IrO_x-Ta_2O_5 sample has the highest gradient followed by $TaIrO_x$ and the lowest commercial IrO_2-TiO_2. All samples have an ECSA cyclic voltammogram of a box shape classified more as non-faradaic. According to literature studies conducted by (Monteiro et al., 2020) a cyclic voltammogram with a box-shaped or constant current over a range of

potentials indicates that the process being studied has limited diffusion. This is because the reaction rate is restricted by the transport of products and species from the electrode surface to the other parts of the system.

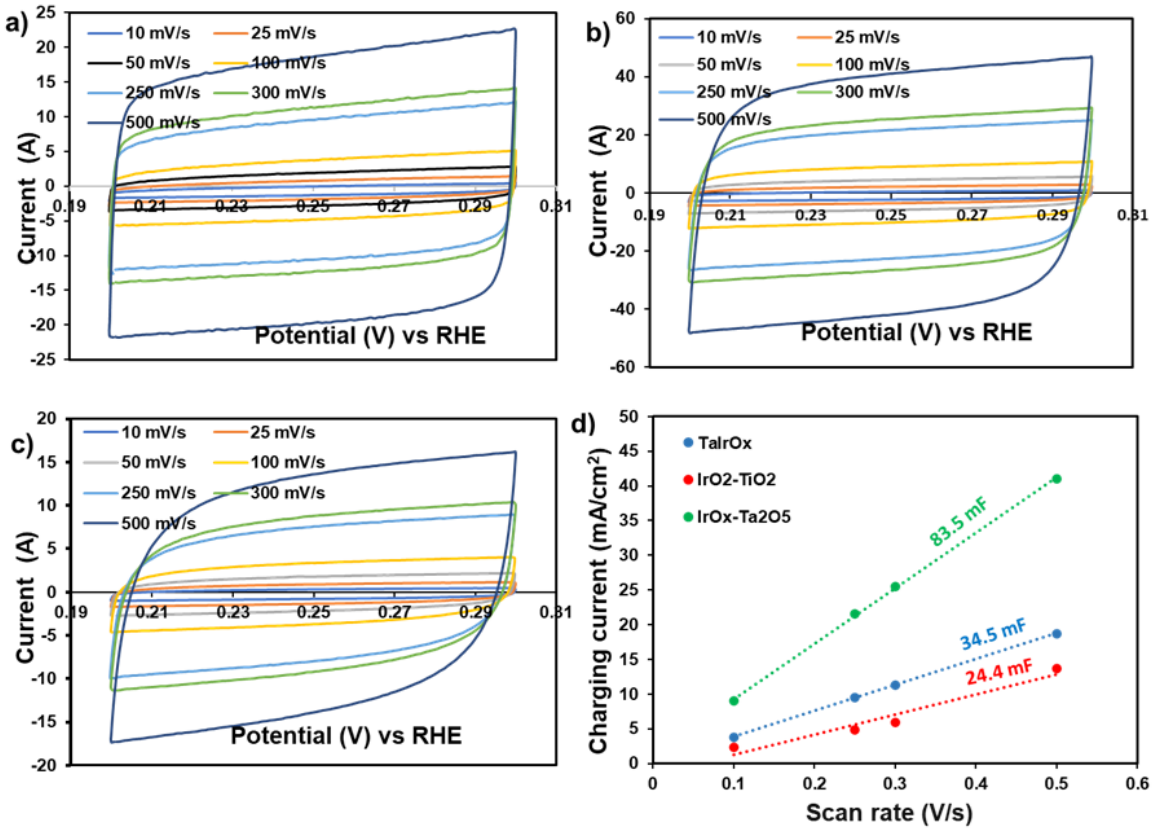

Figure 5-4: non-faradaic region for the cyclic voltammograms measured in the potential window of 0.2 – 0.3 V of the sample (a) IrO_x-Ta_2O_5, (b) $TaIrO_x$,(c) commercial benchmark IrO_2-TiO_2 and (d) gradients values representing the ECSA estimation.

5.3 The electrochemical performance evaluation of the electrocatalysts

5.3.1 OER activity of IrO_x nanomaterials using different oxidising reagents and post-treatment

The cyclic voltammetry method was used to analyse the OER activities for each catalyst at 1 - 1.6 V vs. RHE at a scan rate of 10 $mV.s^{-1}$. The results are shown in Figure 5.5, and the method is described in Chapter 3 section 3.5.4. The current measured at 1.525 volts was normalised for

the different Ir masses in the catalysts and the ink deposited on the glassy carbon electrode. The bar graph clearly shows the OER mass-specific activity evaluated at 1.525 V vs. RHE. Figure 5.5 (a) shows that the OER polarization curves for the $IrO_{x\text{-}(Na)}$ catalyst exhibit similar catalytic activity to that of the TKK. The $IrO_{x\text{-}(Ba)}$ exhibited poor activity despite having a higher BET surface area, and Ir loading, compared to the sodium sample. Through literature studies the OER activity can be influenced by the oxidation state of iridium, Ir^{3+} and Ir^{4+} (Kasian et al., 2018; Kasian et al., 2019; Cherevko et al., 2016 & Gu et al., 2020). The Ir-based catalysts associated with Ir^{4+} oxidation states are less active compared to Ir^{3+} oxidation states which are more active (Ma et al., 2023).

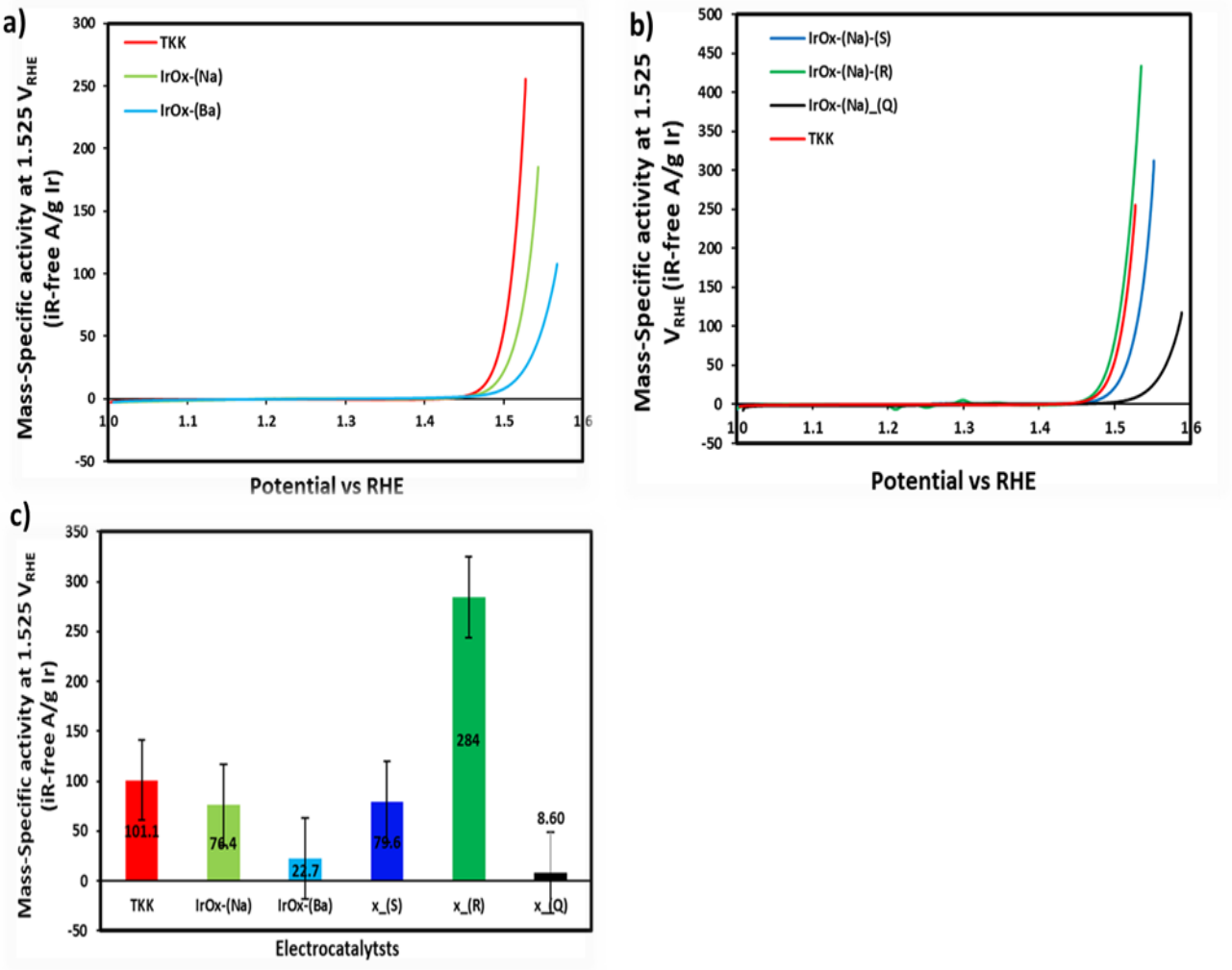

X = $IrO_{x\text{-}(Na)}$

Figure 5-5: Linear sweep voltammograms measured in the potential window of 1 – 1.6 mV (a & b) of sample commercial benchmark IrO_2 TKK (red), $IrO_{x\text{-}(Na)}$ (light green); $IrO_{x\text{-}(Ba)}$, (light blue), $IrO_{x\text{-}(Na)\text{-}(S)}$ (blue), $IrO_{x\text{-}(Na)\text{-}(R)}$ (green), and $IrO_{x\text{-}(Na)\text{-}(Q)}$ (black). Bar graph (c) of

all samples showing mass-specific activity (A/g Ir) at a scan rate of 10 mV.s^{-1} in 0.1 M $HClO_4$ under Argon saturation.

The activity in decreasing order, of the $IrO_{x\text{-}(Na)}$ based catalysts (R) exhibit the highest followed by the commercial TKK, (S) and the least (Q) shown in Figure 5.5 (b). The catalysts exhibit different catalytic activities, linked to their unique structure or surface properties. The mass activities of certain catalysts correlate with their ECSA. Higher ECSA were associated with higher mass activities. The rapidly cooled $IrO_{x\text{-}(Na)\text{-}(R)}$ catalyst yielded to more active catalyst compared to other catalysts. Modifying the electronic structure or adding active sites, nitrogen can be introduced to the IrO_x-based catalyst, which can enhance its catalytic performance. This can help activate the reactant molecules and facilitate the adsorption process (Velasco-Vélez et al., 2021). The $IrO_{x\text{-}(Na)\text{-}(R)}$ catalyst is more active compared to $IrO_{x\text{-}(Na)\text{-}(Q)}$. In a study by Li and colleagues 2022, the use of IrO_x/N-TiO_2 as the anode catalyst results in lower single-cell voltages, highlighting its enhanced performance and efficiency in the electrochemical system compared to the commercial IrO_2 counterpart. In another study conducted in 2023, Deng and colleagues discovered that a nitrogen-doped carbon material can enhance the adsorption and conversion rates of carbon dioxide in a process known as CO_2 hydrogenation. It can also improve selectivity and lower the starting temperature of the reaction.

Table 5.1 shows comparison of Figure 5.5 to relevant literature. The $IrO_{x\text{-}(Na)\text{-}(R)}$ catalyst stands out with the lowest overpotential (~0.30 V) and highest mass activity 284 A/g Ir, suggesting a favourable surface structure, increased active site exposure, or enhanced conductivity. Its performance is comparable to Ir/IrO_x on Ti (Wang et al., 2020) and Ir-NiO_x hybrids (Chen et al., 2019), indicating its potential for real-world applications. The $IrO_{x\text{-}(Na)\text{-}(Q)}$ catalyst has the highest overpotential (>0.45 V) and lowest activity 8.60 A/g Ir, suggesting poor conductivity, low active site availability, or an unfavourable oxidation state. In comparison to literature Ir-RuO_x alloys reported by Ma et al., 2022, show the best performance (~0.26–0.30 V overpotential, ~300–400 A/g Ir), likely due to Ru's ability to enhance OER kinetics while reducing Ir content. Ir/IrO_x on Ti (Wang et al., 2020) and Ir-NiO_x hybrids (Chen et al., 2019) also achieve high activity with lower overpotentials, emphasizing the role of support interactions and alloying effects in improving Ir utilization.

Table 5-1: Comparative table of OER performance for various Ir-based catalysts, including relevant literature.

Catalyst	Overpotential @ 10 mA/cm² (V vs. RHE)	Mass-Specific Activity @ 1.525 V (A/g Ir)	Reference
IrO_2	~0.35 – 0.40	~100	Lee et al., 2021
Ir/IrO_x on Ti	~0.28 – 0.32	~250 – 300	Wang et al., 2020
Ir-NiO_x Hybrid	~0.29 – 0.33	~200 – 250	Chen et al., 2019
Ir-RuO_x Alloy	~0.26 – 0.30	~300 – 400	Ma et al., 2022

5.3.2 OER activity of IrO_x nanomaterials of the mixed-metal and supported material

Cyclic voltammetry was used to analyse the OER activities for each catalyst at 1 - 1.6 V vs. RHE at a scan rate of 10 $mV.s^{-1}$ and the results are shown in Figure 5.6 (a). The bar graph provides the OER mass-specific activity evaluated at 1.525 V vs. RHE. As seen in Figure 5.6 (b), the mass activities of each catalyst are similar. However, the $TaIrO_x$ catalyst is more active than the others, according to the literature, $TaIrO_x$ and other mixed metal oxides can exhibit enhanced catalytic capabilities due to their improved active site attributes and electronic environment. The addition of Ta to IrO_x lowered the OER activity as compared to $IrO_{x\text{-}(Na)}$ catalyst. Although Ta_2O_5 does not directly interact with the catalytic process, it can have a significant impact on the iridium oxide but can influence the stability, and dispersion properties (Mahfoudh et al., 2023 & Wang et al., 2021).

The IrO_x-TiO_2 catalyst exhibited a lower activity due to the lower conductivity of the TiO_2 support. These values closely resembled the values obtained from the literature describing the commercial catalyst (Rajan 2020; Hartig-Weiss 2020, & Hoffman et al., 2023). The unsupported catalysts from previous section 5.31, showed greater OER activity compared to the mixed-metals and supported catalysts.

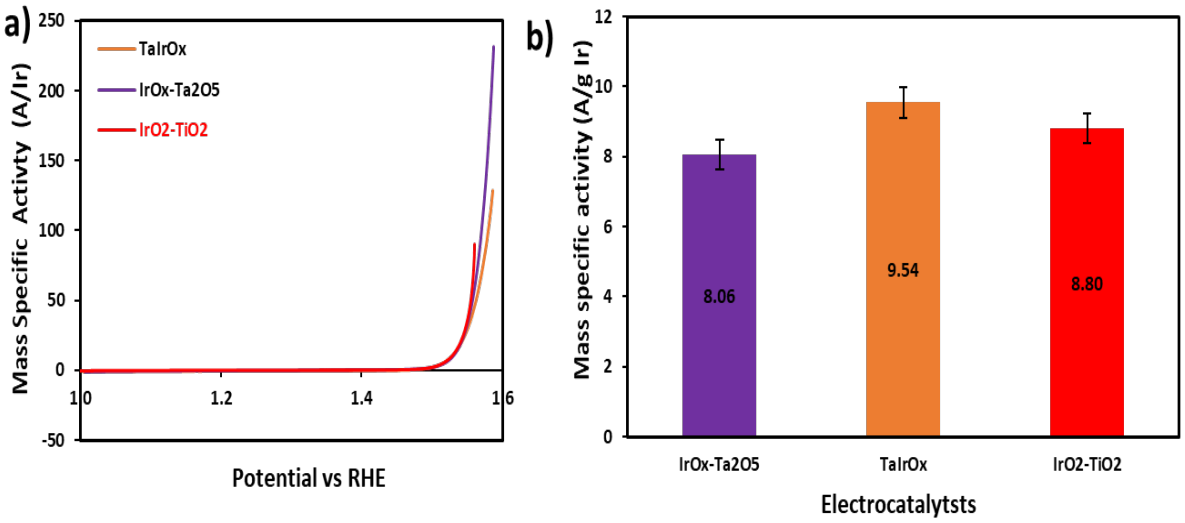

Figure 5-6: Linear sweep voltammograms measured in the potential window of 1 – 1.6 mV (a) and (b) bar graph of the sample (purple) IrO_x-Ta_2O_5, (orange) $TaIrO_x$,(red) commercial benchmark IrO_2-TiO_2 showing mass-specific activity (A/g Ir) at a scan rate of 10 mV.s^{-1} in 0.1 M $HClO_4$ under Argon saturation.

5.4 Electrochemical stability studies

5.4.1 Electrochemical stability studies of IrO_x nanomaterials using different oxidising reagents and post-treatment

Chronoamperometry (CA) analysis was performed to obtain information about the catalytic performance, and stability, and results are shown in Figure 5.7. Table 5.2 shows the before and after two hours relative OER percentage activity loss after stability tests. The corresponding Tafel slope values were measured using chronoamperometry steps between 1.525 and 1.560 mV. s^1. Figure 5.7 shows the Tafel slope values for each catalyst before and after the durability test. A steeper slope is associated with slower kinetics a higher activation energy required for the reaction to occur, and a shallow slope has faster kinetics, indicating that it is faster. In IrO_2 literature, higher Tafel slopes of 60 mV dec^{-1} are frequently reported (Reier et al., 2012; Guerrini et al., 2017; Guerrini et al., 2017 & Ferro et al., 2014). However, these catalysts tend to show a higher concentration of crystallinity. On the other hand, lower Tafel slopes are characterised by a hydrous surface that is usually associated with amorphization (Abbott et al., 2016).

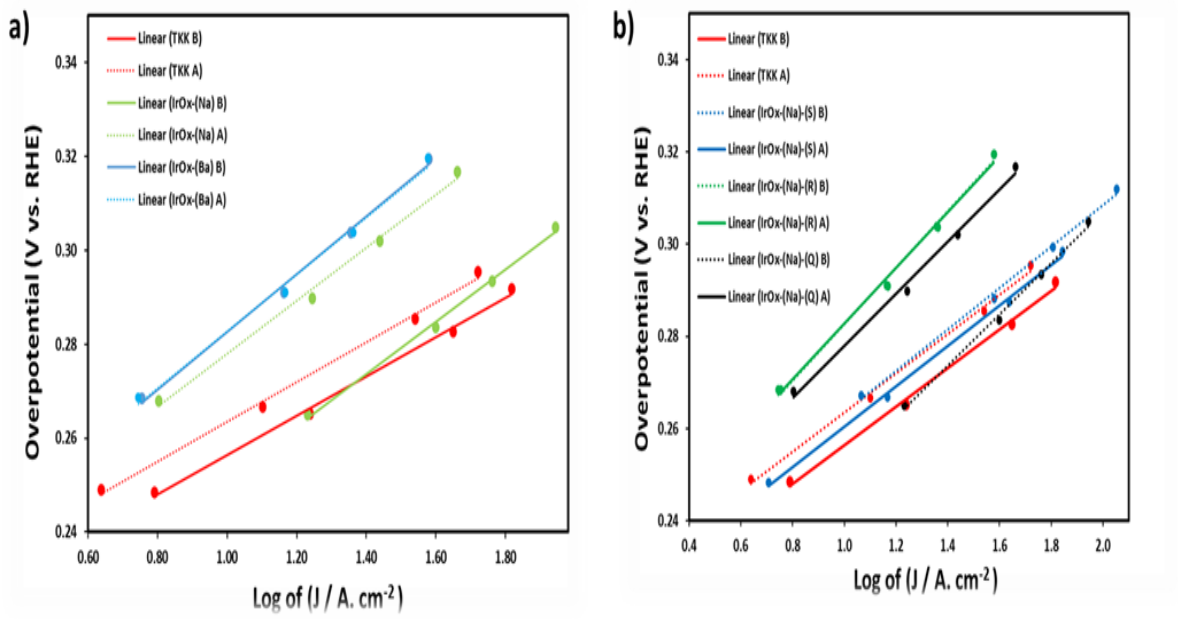

Figure 5-7: Before and after two hours stability Tafel plots were measured using chronoamperometry steps between 1.525 – 1.560 mV. s^1 of catalysts (a) commercial benchmark IrO_2 TKK (red), $IrO_{x\text{-}(Na)}$ (light green); $IrO_{x\text{-}(Ba)}$ (light blue), and in (b) $IrO_{x\text{-}(Na)\text{-}(S)}$ (blue), $IrO_{x\text{-}(Na)\text{-}(R)}$ (green), and $IrO_{x\text{-}(Na)\text{-}(Q)}$ (black). The solid lines (before) and dotted lines stability evaluation (after).

The $IrO_{x\text{-}(Na)}$ and $IrO_{x\text{-}(Ba)}$ samples have higher Tafel slope values, with values ranging from 60 to 65 mV dec^{-1} which indicates that the OER is slower compared to that of TKK which ranges 41 to 43 mV dec^{-1}. In contrast to the samples using different cooling post-treatment methods, the catalyst $IrO_{x\text{-}(Na)\text{-}(R)}$ has the lowest Tafel slope before the applied voltage, this indicates that the electrochemical reaction taking place is faster, followed by TKK, $IrO_{x\text{-}(Na)\text{-}(S)}$, and the catalyst $IrO_{x\text{-}(Na)\text{-}(Q)}$ has the slowest kinetics. After the two hours hold at 1.6 V, the $IrO_{x\text{-}(Na)\text{-}(R)}$, and $IrO_{x\text{-}(Na)\text{-}(Q)}$ catalysts exhibited a significant increase in the Tafel slope values indicating a decrease in reaction kinetics. While catalysts $IrO_{x\text{-}(Na)\text{-}(S)}$, and TKK had a slight decrease indicating improved reaction kinetics after the stability test. If the slope remains the same there is a physical degradation in which the surface chemistry remains the same, but it is evident that there is less conversion. Sample $IrO_{x\text{-}(Na)\text{-}(Q)}$ has a significant change after the 2-hour hold, this the surface undergoes a higher chemical degradation which changes the surface chemistry and therefore the kinetics.

Table 5-2: Comparison of percentage stability loss and Tafel plots of before and after two hours hold at 1.6 volts of the in-house and commercial TKK iridium oxide catalysts.

Electrocatalysts	Stability			Tafel Plot	
	Before @1,525 V	**After @1,525 V**	**% relative losses after 2hrs hold**	**Before @mV/dec**	**After @mV/dec**
TKK	83.8	55.4	33.9	42.5	41.8
$IrO_{x-(Na)}$	74.4	47.1	27.3	64.2	60.4
$IrO_{x-(Ba)}$	20.0	18.4	1.60	61.4	60.7
$IrO_{x-(Na)-(S)}$	50.7	61.7	-11.1	45.1	43.9
$IrO_{x-(Na)-(R)}$	215.1	144.5	70.6	46	50.7
$IrO_{x-(Na)-(Q)}$	6.30	5.01	1.29	51.7	61.3

All the catalysts have different catalytic performance at 1.525 V voltage. After a two-hour hold, significant performance losses were observed in samples TKK, $IrO_{x-(Na)}$, $IrO_{x-(Na)-(R)}$, and $IrO_{x-(Na)-(Q)}$. The $IrO_{x-(Ba)}$ catalyst is the most stable activity, while performance improved in sample $IrO_{x-(Na)-(S)}$ refer to Table 5.1. A study conducted by Tan and his colleagues in 2019 revealed that the catalyst TKK IrO_x degraded significantly after three hours of continuous CA analysis. Sample $IrO_{x-(Na)-(R)}$, has a high significant percentage relative loss after the two-hour hold. Dissolution of iridium is one of the primary ways in which iridium oxide OER catalysts deactivate. The phenomenon can be attributed to the oxidation state of iridium in the catalyst. According to the work published by Cherevko 2016 & Vélez, 2016), research has shown that Ir(IV) is the most stable phase of iridium. On the other hand, Ir(III) is known to dissolve in iridium oxide materials. The percentages of relative losses exhibited by various nanomaterials can be explained by their respective contributions to Ir(III) and Ir(IV).

5.4.2 Electrochemical stability studies of IrO_x nanomaterials of the mixed-metal and supported material

Table 5.3 shows the before and after percentage OER activity loss following a stability test. The corresponding Tafel slope values were measured using chronoamperometry steps between 1.525 and 1.560 mV. s^{1}. The Tafel slope for the initial and after stability tests are shown in Figure 5.8.

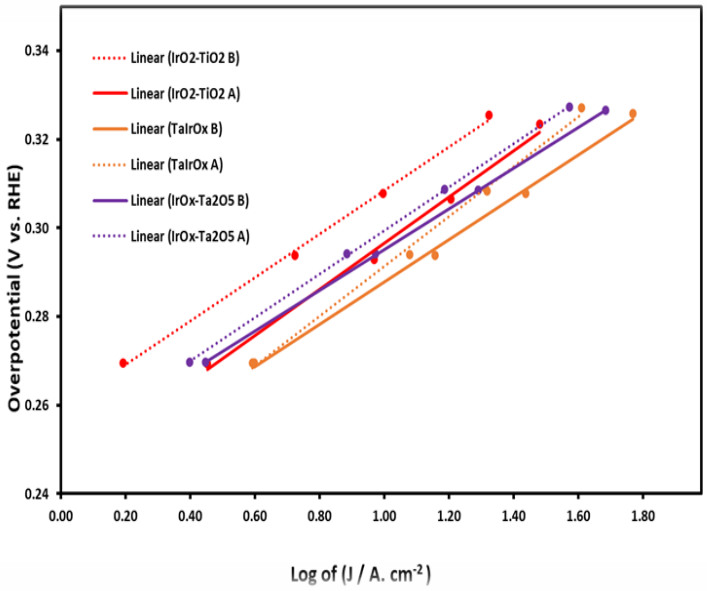

Figure 5-8: Before and after two hours Tafel plots were measured using chronoamperometry steps between 1.525 – 1.560 mV. s^{1} of catalysts (orange)-($TaIrO_x$), (purple)-(IrO_x-Ta_2O_5), and (red)- (IrO_x -TiO_2).

After the stability test, the performance of the IrO_x-Ta_2O_5 sample had decreased significantly. With a percentage loss of 4.8%, which indicates a degradation, this could be attributed to the Ir (III) oxidation state revealed by XPS. A similar loss weight percentage was observed for commercial IrO_2-TiO_2 catalysts and Hoffman et al., 2023, and colleagues obtained the equivalent losses after two hours of hold. The $TaIrO_x$ sample percentage loss is incredibly low at 1.34%, suggesting almost low degradation over time. In section 5.4.1, it was discussed that the $IrO_{x\text{-}(Na)}$ catalysts were unstable about ± 30% degradation was observed in all catalysts. By adding Ta on IrO_x, the degradation rate of the catalyst was only 1.34%, which is lower than the samples made from monometallic materials. The synergistic effects of Ta and IrO_x can enhance the stability and catalytic activity of a material (Xie et al., 2024). The $TaIrO_x$ exhibit a higher Tafel slope value ranging from 51 to 66 mV dec^{-1} which indicates that they OER is considerably slower compared to the supported catalysts IrO_x-Ta_2O_5, and commercial IrO_2-TiO_2 which range 45 to 52 mV dec^{-1}. Hoffman et al., 2023 obtained a similar Tafel slope value

54.0 mV dec^{-1}. This is comparable to the values found in literature for similar supported catalysts (Rajan 2020, and Spöri 2019).

Table 5-3: Comparison of percentage stability loss and Tafel plots of before and after two hours hold at 1.6 volts of the in-house catalysts and commercial IrO_x-TiO_2 catalyst.

Electrocatalysts	Stability			Tafel Plot	
	Before @1,525 V	After @1,525 V	% relative losses after 2hrs hold	Before @mV/dec	After @ mV/dec
IrO_x-Ta_2O_5	8.71	3.88	4.83	45.9	49.0
$TaIrO_x$	9.06	7.72	1.34	51.4	66.1
IrO_2-TiO_2	8.90	4.86	4.04	49.2	52.2

5.5 References

Abbott, D. F., Lebedev, D., Waltar, K., Povia, M., Nachtegaal, M., Fabbri, E., Copéret, C., & Schmidt, T. J. (2016). Iridium oxide for the oxygen evolution reaction: Correlation between particle size, morphology, and the surface hydroxo layer from operando XAS. *Chemistry of Materials*, *28*(18), 6591–6604. https://doi.org/10.1021/acs.chemmater.6b02625.

Agrawal, K., Naik, A. A., Chaudhary, S., Parvatalu, D., & Santhanam, V. (2021). Prudent Practices in ex situ Durability Analysis Using Cyclic Voltammetry for Platinum-based Electrocatalysts. *In Chemistry - An Asian Journal* (Vol. 16, Issue 21, pp. 3311–3325). https://doi.org/10.1002/asia.202100746.

Ali, A., Chiang, Y. W., & Santos, R. M. (2022). X-Ray Diffraction Techniques for Mineral Characterization: A Review for Engineers of the Fundamentals, Applications, and Research Directions. *Minerals*, *12*(2). https://doi.org/10.3390/min12020205.

Alia, S. M., Rasimick, B., Ngo, C., Neyerlin, K. C., Kocha, S. S., Pylypenko, S., Xu, H., & Pivovar, B. S. (2016). Activity and Durability of Iridium Nanoparticles in the Oxygen

Evolution Reaction. *Journal of The Electrochemical Society*, *163*(11), F3105–F3112. https://doi.org/10.1149/2.0151611jes.

Alia, S. M., Hurst, K. E., Kocha, S. S., & Pivovar, B. S. (2016). Mercury Underpotential Deposition to Determine Iridium and Iridium Oxide Electrochemical Surface Areas. *Journal of The Electrochemical Society*, *163*(11), F3051–F3056. https://doi.org/10.1149/2.0071611jes.

Atanassova, E., & Spassov, D. (1998). X-ray photoelectron spectroscopy of thermal thin Ta O films on 2 5 Si. *In Applied Surface Science* (Vol. 135).

Baik, C., Cho, J., Cha, J. I., Cho, Y., Jang, S. S., & Pak, C. (2023). Electron-rich Ir nanostructure supported on mesoporous Ta_2O_5 for enhanced activity and stability of oxygen evolution reaction. *Journal of Power Sources*, *575*. https://doi.org/10.1016/j.jpowsour.2023.233174.

Baudouy, B. (2014). Heat transfer and cooling techniques at low temperatures. *CAS-CERN Accelerator School: Superconductivity for Accelerators - Proceedings*, 329–352. https://doi.org/10.5170/CERN-2014-005.329.

Biesinger, M. C. (2022). Accessing the robustness of adventitious carbon for charge referencing (correction) purposes in XPS analysis: Insights from a multi-user facility data review. *Applied Surface Science*, *597*. https://doi.org/10.1016/j.apsusc.2022.153681.

Biesheuvel, P. M., Porada, S., & Dykstra, J. E.(2018). (n.d.). The difference between Faradaic and non-Faradaic electrode processes.

Bernt, M., Schramm, C., Schröter, J., Gebauer, C., Byrknes, J., Eickes, C., & Gasteiger, H. A. (2021). Effect of the IrO x Conductivity on the Anode Electrode/Porous Transport Layer Interfacial Resistance in PEM Water Electrolyzers. *Journal of The Electrochemical Society,* 168(8), 084513. https://doi.org/10.1149/1945-7111/ac1eb4.

Birss-et-al-2011-hydrous-ir-oxide-films-the-mechanism-of-the-ano. (n.d.).

Brownson, D. A. C., & Banks, C. E. (2014). Interpreting Electrochemistry. *In The Handbook of Graphene Electrochemistry* (pp. 23–77). Springer London. https://doi.org/10.1007/978-1-4471-6428-9_2.

Casella, I. G., Contursi, M., & Toniolo, R. (2015). Anodic electrodeposition of iridium oxide particles on glassy carbon surfaces and their electrochemical/SEM/XPS characterization.

Journal of Electroanalytical Chemistry, *736*, 147–152. https://doi.org/10.1016/j.jelechem.2014.11.012.

Chen, F. Y., Wu, Z. Y., Adler, Z., & Wang, H. (2021). Stability challenges of electrocatalytic oxygen evolution reaction: From mechanistic understanding to reactor design. *In Joule* (Vol. 5, Issue 7, pp. 1704–1731). Cell Press. https://doi.org/10.1016/j.joule.2021.05.005

Cherevko, S., Geiger, S., Kasian, O., Mingers, A., & Mayrhofer, K. J. J. (2016). Oxygen evolution activity and stability of iridium in acidic media. Part 2. - Electrochemically grown hydrous iridium oxide. *Journal of Electroanalytical Chemistry*, *774*, 102–110. https://doi.org/10.1016/j.jelechem.2016.05.015.

Deng, C., Xu, L., Hu, K., Chen, X., Gao, R., Zhang, L., Wang, L., & Zhang, C. (2023). Research Advances on Nitrogen-Doped Carbon Materials in CO_x Hydrogenation. In *Atmosphere* (Vol. 14, Issue 10). *Multidisciplinary Digital Publishing Institute (MDPI)*. https://doi.org/10.3390/atmos14101510.

Dwivedi, V. K., & Mukhopadhyay, S. (2019). Suppression of long-range magnetic ordering and electrical conduction in Y1.7Bi0.3Ir2O7 thin film. *In Journal of Magnetism and Magnetic Materials* (Vol. 484, pp. 313–319). Elsevier B.V. https://doi.org/10.1016/j.jmmm.2019.04.049

Duran, S., Elmaalouf, M., Odziomek, M., Piquemal, J. Y., Faustini, M., Giraud, M., Peron, J., & Tard, C. (2021). Electrochemical Active Surface Area Determination of Iridium-Based Mixed Oxides by Mercury Underpotential Deposition. *ChemElectroChem*, *8*(18), 3519–3524. https://doi.org/10.1002/celc.202100649.

Elgrishi, N., Rountree, K. J., McCarthy, B. D., Rountree, E. S., Eisenhart, T. T., & Dempsey, J. L. (2018). A Practical Beginner's Guide to Cyclic Voltammetry. *Journal of Chemical Education*, *95*(2), 197–206. https://doi.org/10.1021/acs.jchemed.7b00361.

Elmaalouf, M., Odziomek, M., Duran, S., Gayrard, M., Bahri, M., Tard, C., Zitolo, A., Lassalle-Kaiser, B., Piquemal, J. Y., Ersen, O., Boissière, C., Sanchez, C., Giraud, M., Faustini, M., & Peron, J. (2021). The origin of the high electrochemical activity of pseudo-amorphous iridium oxides. *Nature Communications*, *12*(1). https://doi.org/10.1038/s41467-021-24181-x.

Felix, C., Maiyalagan, T., Pasupathi, S., Bladergroen, B., & Linkov, V. (2012). Synthesis, characterisation, and evaluation of IrO_2-based binary metal oxide electrocatalysts for oxygen

evolution reaction. *International Journal of Electrochemical Science*, *7*(12), 12064–12077. https://doi.org/10.1016/s1452-3981(23)16526-6.

Felix, C., Bladergroen, B. J., Linkov, V., Pollet, B. G., & Pasupathi, S. (2019). Ex-situ electrochemical characterization of IrO2 synthesized by a modified Adams fusion method for the oxygen evolution reaction. *Catalysts*, *9*(4). https://doi.org/10.3390/catal9040318.

Fernández, M. P. R., Gehrke, S. A., Martinez, C. P. A., Guirado, J. L. C., & de Aza, P. N. (2017). SEM-EDX study of the degradation process of two xenograft materials used in sinus lift procedures. *Materials*, *10*(5). https://doi.org/10.3390/ma10050542.

Ferro, S., Rosestolato, D., Martínez-Huitle, C. A., & de Battisti, A. (2014). On the oxygen evolution reaction at IrO2-SnO2 mixed-oxide electrodes. *Electrochimica Acta*, *146*, 257–261. https://doi.org/10.1016/j.electacta.2014.08.110.

Galyamin, D., Tolosana-Moranchel, Á., Retuerto, M., & Rojas, S. (2023). Unravelling the Most Relevant Features for the Design of Iridium Mixed Oxides with High Activity and Durability for the Oxygen Evolution Reaction in Acidic Media. *In JACS Au* (Vol. 3, Issue 9, pp. 2336–2355). American Chemical Society. https://doi.org/10.1021/jacsau.3c00247.

Geiger, S., Kasian, O., Shrestha, B. R., Mingers, A. M., Mayrhofer, K. J. J., & Cherevko, S. (2016-9). Activity and Stability of Electrochemically and Thermally Treated Iridium for the Oxygen Evolution Reaction. *Journal of The Electrochemical Society*, *163*(11), F3132–F3138. https://doi.org/10.1149/2.0181611jes.

Guerrini, E., Chen, H., & Trasatti, S. (2017). Oxygen evolution on aged IrO x /Ti electrodes in alkaline solutions. *Journal of Solid-State Electrochemistry*, *11*(7), 939–945. https://doi.org/10.1007/s10008-006-0238-4s.

Gu, X. K., Camayang, J. C. A., Samira, S., & Nikolla, E. (2020). Oxygen evolution electrocatalysis using mixed metal oxides under acidic conditions: Challenges and opportunities. In *Journal of Catalysis* (Vol. 388, pp. 130–140). Academic Press Inc. https://doi.org/10.1016/j.jcat.2020.05.008.

Hartig-Weiss, A., Miller, M., Beyer, H., Schmitt, A., Siebel, A., Freiberg, A.T.S., Gasteiger, H.A. & El-Sayed, H.A. (2020). Iridium Oxide Catalyst Supported on Antimony-Doped Tin Oxide for High Oxygen Evolution Reaction Activity in Acidic Media. *ACS Applied Nano Materials.* 3(3):2185-2196.

Harvey, D. (n.d.).2024. Instrumental analysis. https://LibreTexts.org.

Hoffman, J. A., Rajan, Z. S. H. S., Susac, D., Matoetoe, M. C., & Mohamed, R. (2023). Influence of Support Physicochemical Properties on the Oxygen Evolution Reaction Performance of ITO-Supported IrOx Nanoparticles. *Journal of Physical Chemistry C*, *127*(2), 894–906. https://doi.org/10.1021/acs.jpcc.2c06501.

Hong, B. K., Mandal, P., Oh, J. G., & Litster, S. (2016). On the impact of water activity on reversal tolerant fuel cell anode performance and durability. *Journal of Power Sources*, *328*, 280–288. https://doi.org/10.1016/j.jpowsour.2016.07.002.

Huang, Y., Liu, L., & Liu, X. (2019). Modulated electrochemical oxygen evolution catalysed by MoS_2 nanoflakes from atomic layer deposition. *Nanotechnology*, *30*(9). https://doi.org/10.1088/1361-6528/aaef13.

Hu, J. M., Meng, H. M., Zhang, J. Q., & Cao, C. N. (n.d.). (2021). Degradation mechanism of long service life Ti/IrO_2-Ta_2O_5 oxide anodes in sulphuric acid. www.elsevier.com/locate/corsciCorrosionScience44.

Islam, J., Kim, S. K., Rahman, M. M., Thien, P. T., Kim, M. J., Cho, H. S., Lee, C., Lee, J. H., & Lee, S. (2023). The effect of iridium content in boron carbide-supported iridium catalyst on the activity and stability of proton exchange membrane water electrolyser. *Materials Today Energy*, *32*. https://doi.org/10.1016/j.mtener.2022.101237.

Islam, J., Yoon, B. S., Thien, P. T., Ko, C. H., & Kim, S. K. (2024). Enhancing oxygen evolution reaction performance in PEM water electrolyzers through support pore structure optimization. *Catalysis Today*, *425*. https://doi.org/10.1016/j.cattod.2023.114349

Jagga, S., & Vanapalli, S. (2020). Cooldown of insulated metals in saturated and subcooled liquid nitrogen. *Cryogenics*, *109*. https://doi.org/10.1016/j.cryogenics.2020.103114

Johnson Space Center. (2022). *Using Dry Ice as a Coolant for Cutting Tools.* Available: https://www.techbriefs.com/component/content/article/tb/pub/briefs/materials/6745. [2022, 20 September].

Kasian, O., Grote, J., Geiger, S., Cherevko, S., & Mayrhofer, K. J. J. (2018). The Common Intermediates of Oxygen Evolution and Dissolution Reactions during Water. *130*(9), 2514–2517. https://doi.org/10.1002/ange.201709652.

Kasian, O., Geiger, S., Li, T., Grote, J. P., Schweinar, K., Zhang, S., Scheu, C., Raabe, D., Cherevko, S., Gault, B., & Mayrhofer, K. J. J. (2019). Degradation of iridium oxides via oxygen evolution from the lattice: Correlating atomic-scale structure with reaction mechanisms. *Energy and Environmental Science*, *12*(12), 3548–3555. https://doi.org/10.1039/c9ee01872g.

Krizan, J. W., Roudebush, J. H., Fox, G. M., & Cava, R. J. (2014). The chemical instability of Na_2IrO_3 in air. *Materials Research Bulletin*, *52*, 162–166. https://doi.org/10.1016/j.materresbull.2014.01.021.

Labi, T. N. (2019). Iridium oxide is supported on graphitized carbon for reversal tolerant anodes in PEM fuel cells.

Labi, T., van Schalkwyk, F., Andersen, S. M., Morgen, P., Ray, S. C., & Chamier, J. (2021). Increasing fuel cell durability during prolonged and intermittent fuel starvation using supported IrOx. *Journal of Power Sources*, *490*. https://doi.org/10.1016/j.jpowsour.2021.229568.

Lee, J., & Kim, Y. (2011). Chemical dissolution of iridium powder using alkali fusion followed by high-temperature leaching. *Materials Transactions,* 52(11), 2067–2070. https://doi.org/10.2320/matertrans.M2011202.

Li, G., Jia, H., Liu, H., Yang, X., & Lin, M. C. (2022). Nanostructured IrO_x supported on N-doped TiO_2 as an efficient electrocatalyst towards acidic oxygen evolution reaction. *RSC Advances*, *12*(45), 28929–28936. https://doi.org/10.1039/d2ra05374h

Liu, Y., Wang, C., Lei, Y., Liu, F., Tian, B., & Wang, J. (2018). Investigation of high-performance IrO_2 electrocatalysts prepared by Adams method. *International Journal of Hydrogen Energy*, *43*(42), 19460–19467. https://doi.org/10.1016/j.ijhydene.2018.08.196.

Lukowski, M. A., Daniel, A. S., Meng, F., Forteau, A., Li, L., & Jin, S. (2013). Enhanced hydrogen evolution catalysis from chemically exfoliated metallic MoS2 nanosheets. *Journal of the American Chemical Society*, *135*(28), 10274–10277. https://doi.org/10.1021/ja404523s.

Lv, H., Zhang, G., Hao, C., Mi, C., Zhou, W., Yang, D., Li, B., & Zhang, C. (2017). The activity of IrO_2 supported on tantalum-doped TiO_2 electrocatalyst for solid polymer electrolyte water electrolyzer. *RSC Advances*, *7*(64), 40427–40436. https://doi.org/10.1039/c7ra06534e.

Mabate, T. P., Maqunga, N. P., Ntshibongo, S., Maumela, M., & Bingwa, N. (2023). Metal oxides and their roles in heterogeneous catalysis: special emphasis on synthesis protocols,

intrinsic properties, and their influence in transfer hydrogenation reactions. *In SN Applied Sciences* (Vol. 5, Issue 7). Springer Nature. https://doi.org/10.1007/s42452-023-05416-6.

Masliuk, L., Nam, K., Terban, M. W., Lee, Y., Kube, P., Delgado, D., Girgsdies, F., Reuter, K., Schlögl, R., Trunschke, A., Scheurer, C., Zobel, M., & Lunkenbein, T. (2024). Linking Bulk and Surface Structures in Complex Mixed Oxides. *ACS Catalysis*, *14*(11), 9018–9033. https://doi.org/10.1021/acscatal.3c05230.

Ma, Q., & Mu, S. (2023). Acidic oxygen evolution reaction: Mechanism, catalyst classification, and enhancement strategies. *Interdisciplinary Materials*, *2*(1), 53–90. https://doi.org/10.1002/idm2.12059.

McLellan, R. A., Dutta, A., Zhou, C., Jia, Y., Weiland, C., Gui, X., Place, A. P. M., Crowley, K. D., Le, X. H., Madhavan, T., Gang, Y., Baker, L., Head, A. R., Waluyo, I., Li, R., Kisslinger, K., Hunt, A., Jarrige, I., Lyon, S. A., … de Leon, N. P. (2023). Chemical Profiles of the Oxides on Tantalum in State-of-the-Art Superconducting Circuits. *Advanced Science*, *10*(21). https://doi.org/10.1002/advs.202300921.

Merki, D., Vrubel, H., Rovelli, L., Fierro, S., & Hu, X. (2012). Fe, Co, and Ni ions promote the catalytic activity of amorphous molybdenum sulphide films for hydrogen evolution. *Chemical Science*, *3*(8), 2515–2525. https://doi.org/10.1039/c2sc20539d.

Miller, D. J., Biesinger, M. C., & McIntyre, N. S. (2002). Interactions of CO_2 and CO at fractional atmosphere pressures with iron and iron oxide surfaces: One mechanism for surface contamination. *Surface and Interface Analysis*, *33*(4), 299–305. https://doi.org/10.1002/sia.1188.

Monteiro, M. C. O., Jacobse, L., & Koper, M. T. M. (2020). Understanding the Voltammetry of Bulk CO Electrooxidation in Neutral Media through Combined SECM Measurements. *Journal of Physical Chemistry Letters*, *11*(22), 9708–9713. https://doi.org/10.1021/acs.jpclett.0c02779.

Nagai, T., Jahn, C., & Jia, H. (2019). Improved Accelerated Stress Tests for ORR Catalysts Using a Rotating Disk Electrode. *Journal of The Electrochemical Society*, 166(7), F3111–F3115. https://doi.org/10.1149/2.0161907jes.

Jackson, C., Smith, G. T., Inwood, D. W., Leach, A. S., Whalley, P. S., Callisti, M., Polcar, T., Russell, A. E., Levecque, P., & Kramer, D. (2017). Electronic metal-support interaction

enhanced oxygen reduction activity and boron carbide-supported platinum stability. Nature Communications, 8. https://doi.org/10.1038/ncomms15802. *Journal of Physical Chemistry Letters, 11*(22), 9708–9713. https://doi.org/10.1021/acs.jpclett.0c02779.

Oh, H. S., Nong, H. N., Reier, T., Bergmann, A., Gliech, M., Ferreira De Araújo, J., Willinger, E., Schlögl, R., Teschner, D., & Strasser, P. (2016). Electrochemical Catalyst-Support Effects and Their Stabilizing Role for IrO_x Nanoparticle Catalysts during the Oxygen Evolution Reaction. *Journal of the American Chemical Society*, *138*(38), 12552–12563. https://doi.org/10.1021/jacs.6b07199.

Park, J., Lee, S., & Kim, S. (2022). Recent advances in amorphous electrocatalysts for oxygen evolution reaction. *In Frontiers in Chemistry* (Vol. 10). Frontiers Media S.A. https://doi.org/10.3389/fchem.2022.1030803.

Pfeifer, V., Jones, T. E., & Velasco, J. J. (2015). Supplementary Information to The Electronic Structure of Iridium Oxide Electrodes Active in Water Splitting.

Powers, J. M. (2024). *LECTURE NOTES ON THERMODYNAMICS*.

Rasten, E. (2001). *Electrocatalysis in Water Electrolysis with Solid Polymer Electrolyte*.

Regmi, Y. N., Tzanetopoulos, E., Zeng, G., Peng, X., Kushner, D. I., Kistler, T. A., King, L. A., & Danilovic, N. (2020). Supported Oxygen Evolution Catalysts by Design: Toward Lower Precious Metal Loading and Improved Conductivity in Proton Exchange Membrane Water Electrolyzers. *ACS Catalysis*, *10*(21), 13125–13135. https://doi.org/10.1021/acscatal.0c03098.

Reier, T., Oezaslan, M., & Strasser, P. (2012). Electrocatalytic oxygen evolution reaction (OER) on Ru, Ir, and pt catalysts: A comparative study of nanoparticles and bulk materials. *ACS Catalysis*, *2*(8), 1765–1772. https://doi.org/10.1021/cs3003098.

Rheinländer, P. J., & Durst, J. (2021). Transformation of the OER-Active IrO_x Species under Transient Operation Conditions in PEM Water Electrolysis. *Journal of The Electrochemical Society*, *168*(2), 024511. https://doi.org/10.1149/1945-7111/abe0d4.

Rodríguez-Parra, J. M., Moreno, R., & Nieto, M. I. (2012). Effect of cooling rate on the microstructure and porosity of alumina produced by freeze casting. *Journal of the Serbian Chemical Society*, *77*(12), 1775–1785. https://doi.org/10.2298/JSC121018132R.

Rong, C., Dastafkan, K., Wang, Y., & Zhao, C. (2023). Breaking the Activity and Stability Bottlenecks of Electrocatalysts for Oxygen Evolution Reactions in Acids. *In Advanced*

Materials (Vol. 35, Issue 49). John Wiley and Sons Inc. https://doi.org/10.1002/adma.202211884.

Ruiz-Cornejo, J. C., Sebastián, D., Martínez-Huerta, M. v., & Lázaro, M. J. (2019). Tantalum-based electrocatalysts are prepared by a microemulsion method for the oxygen reduction and evolution reactions. *Electrochimica Acta*, *317*, 261–271. https://doi.org/10.1016/j.electacta.2019.05.145.

Saveleva, V. A., Wang, L., Teschner, D., Jones, T., Gago, A. S., Friedrich, K. A., Zafeiratos, S., Schlögl, R., & Savinova, E. R. (2018). Operando Evidence for a Universal Oxygen Evolution Mechanism on Thermal and Electrochemical Iridium Oxides. *Journal of Physical Chemistry Letters*, 9(11), 3154–3160. https://doi.org/10.1021/acs.jpclett.8b00810.

Schalenbach, M. (n.d.). Impedance Spectroscopy and Cyclic Voltammetry to Determine Double Layer Capacitances and Electrochemically Active Surface Areas.

Serhan, M., Sprowls, M., Jackemeyer, D., Long, M., Perez, I. D., Maret, W., Tao, N., & Forzani, E. (2019). Total iron measurement in human serum with a smartphone. *AIChE Annual Meeting, Conference Proceedings*, *2019-November*. https://doi.org/10.1039/x0xx00000x.

Siracusano, S., Baglio, V., Grigoriev, S. A., Merlo, L., Fateev, V. N., & Aricò, A. S. (2017). The influence of iridium chemical oxidation state on the performance and durability of oxygen evolution catalysts in PEM electrolysis. *Journal of Power Sources*, *366*, 105–114. https://doi.org/10.1016/j.jpowsour.2017.09.020.

Smith, R. D. L., Sporinova, B., Fagan, R. D., Trudel, S., & Berlinguette, C. P. (2014). Facile photochemical preparation of amorphous iridium oxide films for water oxidation catalysis. *Chemistry of Materials*, *26*(4), 1654–1659. https://doi.org/10.1021/cm4041715.

Song, F., & Hu, X. (2014). Exfoliation of layered double hydroxides for enhanced oxygen evolution catalysis. *Nature Communications*, *5*. https://doi.org/10.1038/ncomms5477.

Spöri, C., Briois, P., Nong, H.N., Reier, T., Billard, A., Kühl, S., Teschner, D. & Strasser, P. 2019. Experimental Activity Descriptors for Iridium-Based Catalysts for the Electrochemical Oxygen Evolution Reaction (OER). *ACS Catalysis.* 9:6653-6663.

Stavrou, E., Zaug, J. M., Bastea, S., & Kunz, M. (2017). *A study of tantalum pentoxide Ta_2O_5 structures up to 28 GPa.*

Steegstra, P., Busch, M., Panas, I., & Ahlberg, E. (2013). Revisiting the redox properties of hydrous iridium oxide films in the context of oxygen evolution. *Journal of Physical Chemistry C*, *117*(40), 20975–20981. https://doi.org/10.1021/jp407030r.

Tan, X., Shen, J., Semagina, N., & Secanell, M. (2019). Decoupling structure-sensitive deactivation mechanisms of Ir/IrO_x electrocatalysts toward oxygen evolution reaction. *Journal of Catalysis*, *371*, 57–70. https://doi.org/10.1016/j.jcat.2019.01.018.

van der Merwe, M., Garcia-Diez, R., Lahn, L., Wibowo, R. E., Frisch, J., Gorgoi, M., Yang, W., Ueda, S., Wilks, R. G., Kasian, O., & Bär, M. (2023). The Chemical and Electronic Properties of Stability-Enhanced, Mixed Ir-TiO_x Oxygen Evolution Reaction Catalysts. *ACS Catalysis*, *13*(23), 15427–15438. https://doi.org/10.1021/acscatal.3c02948.

Velasco-Vélez, J. J., Carbonio, E. A., Chuang, C. H., Hsu, C. J., Lee, J. F., Arrigo, R., Hävecker, M., Wang, R., Plodinec, M., Wang, F. R., Centeno, A., Zurutuza, A., Falling, L. J., Mom, R. V., Hofmann, S., Schlögl, R., Knop-Gericke, A., & Jones, T. E. (2021). Surface Electron-Hole Rich Species Active in the Electrocatalytic Water Oxidation. *Journal of the American Chemical Society*, *143*(32), 12524–12534. https://doi.org/10.1021/jacs.1c01655.

Verner, A., Tokarský, J., Najser, T., Matějová, L., Kutláková, K. M., Kielar, J., & Peer, V. (2023). Effects of Structure and Composition of Adsorbents on Competitive Adsorption of Gaseous Emissions: Experiment and Modeling. *Nanomaterials*, *13*(4). https://doi.org/10.3390/nano13040724.

Vincent, I., & Bessarabov, D. (2016). Electrochemical characterization and oxygen reduction kinetics of Cu-incorporated cobalt oxide catalyst. *International Journal of Electrochemical Science*, *11*(9), 8002–8015. https://doi.org/10.20964/2016.09.12.

Wang, H., Zhang, K. H. L., Hofmann, J. P., de la Peña O'Shea, V. A., & Oropeza, F. E. (2021). The electronic structure of transition metal oxides for oxygen evolution reaction. *In Journal of Materials Chemistry A* (Vol. 9, Issue 35, pp. 19465–19488). Royal Society of Chemistry. https://doi.org/10.1039/d1ta03732c.

Wei, C., Rao, R. R., Peng, J., Huang, B., Stephens, I. E. L., Risch, M., Xu, Z. J., & Shao-Horn, Y. (2019). Recommended Practices and Benchmark Activity for Hydrogen and Oxygen Electrocatalysis in Water Splitting and Fuel Cells. *In Advanced Materials* (Vol. 31, Issue 31). Wiley-VCH Verlag. https://doi.org/10.1002/adma.201806296.

Weber, D., Schoop, L. M., Wurmbrand, D., Laha, S., Podjaski, F., Duppel, V., Müller, K., Starke, U., & Lotsch, B. v. (2018). IrOOH nanosheets as acid-stable electrocatalysts for the oxygen evolution reaction. *Journal of Materials Chemistry A*, *6*(43), 21558–21566. https://doi.org/10.1039/C8TA07950A.

Xie, Y., Luo, F., & Yang, Z. (2024). Strategies for the enhancements in catalytic performance and stability of anodic electrocatalyst in PEM water splitting. *Energy Reviews*, 100103. https://doi.org/10.1016/j.enrev.2024.100103.

Yuan, M., Zhu, Y., Deng, L., Ming, R., Zhang, A., Li, W., Chai, B., & Ren, Z. (2017). IrO_2-TiO_2 electrocatalysts for the hydrogen evolution reaction in acidic water electrolysis without activation. *New Journal of Chemistry*, *41*(14), 6152–6159. https://doi.org/10.1039/c7nj00756f.

Zhao, F., Wen, B., Niu, W., Chen, Z., Yan, C., Selloni, A., Tully, C. G., Yang, X., & Koel, B. E. (2021). Increasing Iridium Oxide Activity for the Oxygen Evolution Reaction with Hafnium Modification. *Journal of the American Chemical Society*, *143*(38), 15616–15623. https://doi.org/10.1021/jacs.1c03473.

Zhao, S., Yu, H., Maric, R., Danilovic, N., Capuano, C. B., Ayers, K. E., & Mustain, W. E. (2015). Calculating the Electrochemically Active Surface Area of Iridium Oxide in Operating Proton Exchange Membrane Electrolyzers. *Journal of The Electrochemical Society*, *162*(12), F1292–F1298. https://doi.org/10.1149/2.0211512jes.

Zhao, X., Liu, X., Huang, B., Wang, P., & Pei, Y. (2019). Hydroxyl group modification improves the electrocatalytic ORR and OER activity of graphene-supported single and bi-metal atomic catalysts (Ni, Co, and Fe). *Journal of Materials Chemistry A*, *7*(42), 24583–24593. https://doi.org/10.1039/c9ta08661g.

Chapter 6: CONCLUSIONS AND RECOMMENDATIONS

This chapter provides a summary of the main findings and recommendations from the study.

6.1 Conclusions

The synthesis of unsupported, supported, and mixed metal iridium oxide/tantalum-based nanomaterials was successful using the Adam fusion method. These were confirmed using various techniques, including spectroscopy, morphological analysis, and electrochemistry. The XRD and TEM analyses revealed that most of the synthesised catalysts were amorphous/low crystalline nanomaterial with an average particle size of ± 5 nm. The highest OER performance was obtained from the catalyst produced by using sodium peroxide oxidizing agent compared to barium peroxide. The $IrO_{x\text{-}(Na)}$ catalyst outperformed both $IrO_{x\text{-}(Ba)}$ and $TaIrO_x$ mixed oxide with greater mass-specific activity at 1.525 V. The post-treatment method did not show any significant difference in the surface area and the particle size from the original method [$IrO_{x\text{-}(Na)}$] nanomaterial. Even though the $IrO_{x\text{-}(Na)\text{-}(R)}$ catalyst had the highest OER compared to all catalysts it was the least stable. A notable increase in surface area was achieved due to the usage of barium peroxide from 11.0 m^2/g to 31.7 m^2/g, while for mixed-oxide catalyst 18.4 m^2/g was obtained. Furthermore, the electrochemical stability of the catalyst was achieved for $IrO_{x\text{-}(Ba)}$ and $TaIrO_x$ catalysts, however at the expense of OER activity. For $TaIrO_x$, XPS revealed that Ta is present as Ta^{5+} (Ta_2O_5) at the catalyst surface. This likely affected OER activity since it is a non-conductive material.

6.2 Recommendations

Some of the recommendations for future research are based on the results and literature analysis of this study. The activity of the best catalysts needs to be evaluated in a PEM water electrolysis cell. The presence of sodium traces, which are likely residual from the sodium peroxide oxidizing agent, can interfere with performance or long-term stability. Implementing a purification mechanism is essential. Further work time and temperature optimisation for the $TaIrO_x$ mixed oxide catalyst are required to identify the influence on the surface area, particle size, OER performance, and stability. Dispersing IrO_x on high-surface-area support materials

such as (e.g., Tungsten carbide, niobium pentoxide, carbon, and Tin(IV) oxide) to increase the surface area and OER performance.

APPENDIX A: PHYSICAL CHARACTERISATION

Section 4.1: Energy Dispersive X-ray Spectroscopy (EDX) spectra of IrO_x nanomaterials.

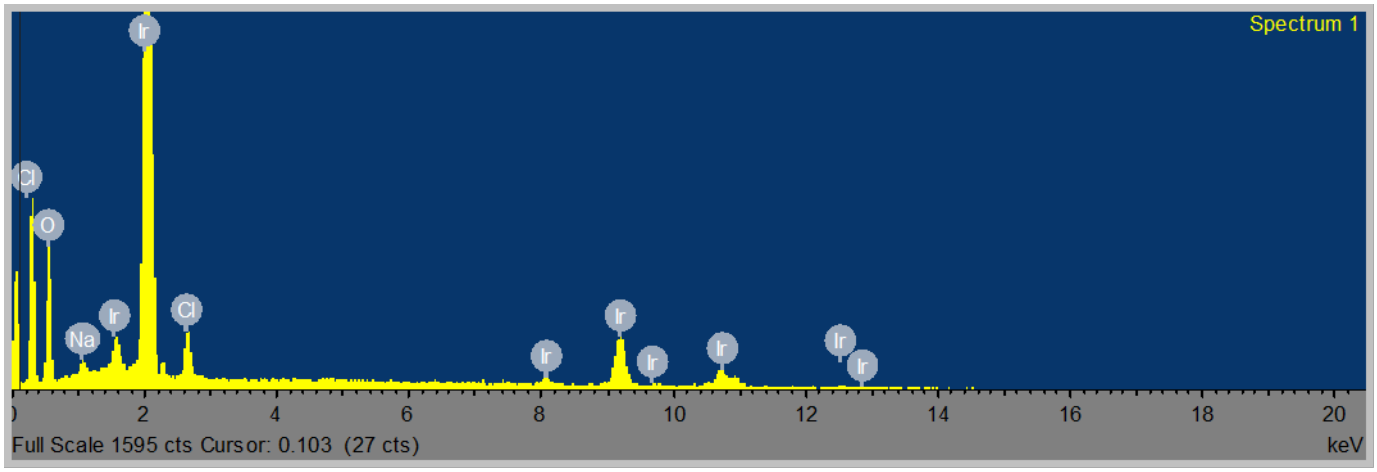

Figure A.1: Energy Dispersive X-ray Spectroscopy (EDX) spectra of $IrO_{x\text{-}(Na)}$.

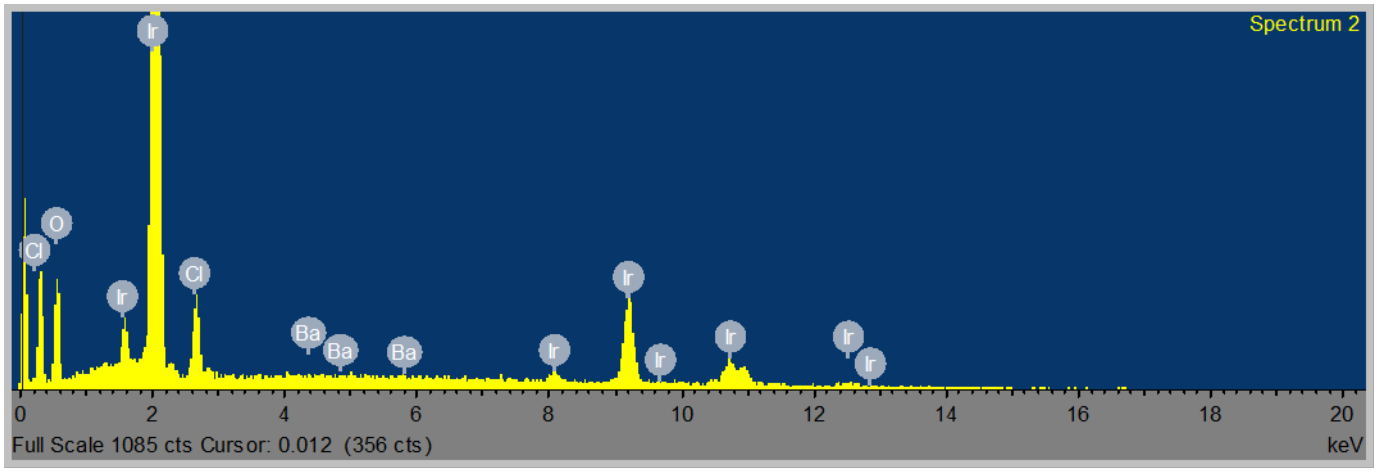

Figure A.2: Energy Dispersive X-ray Spectroscopy (EDX) spectra of $IrO_{x\text{-}(Ba)}$.

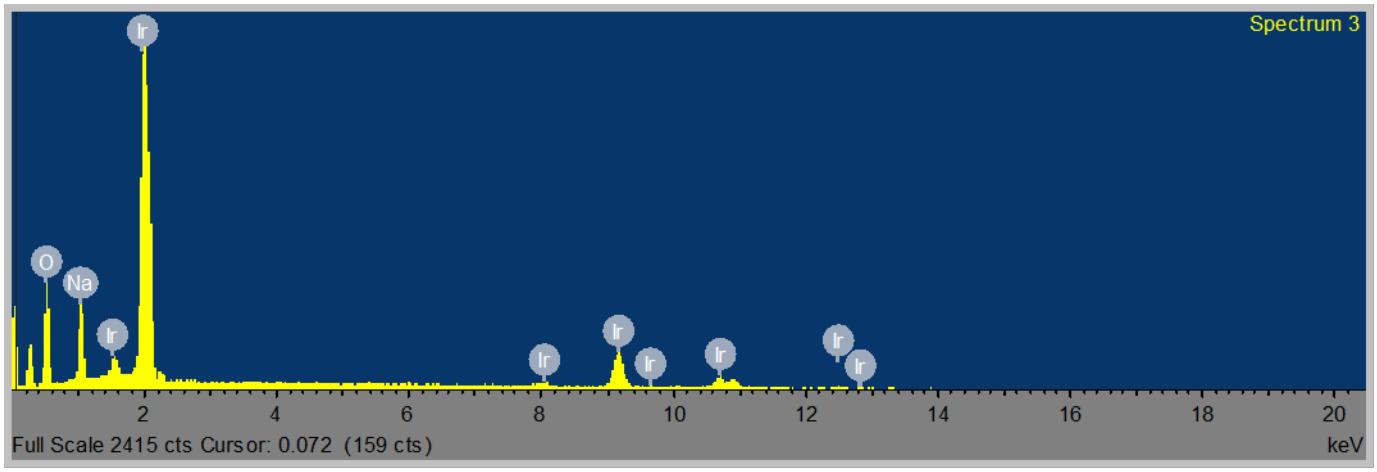

Figure A.3: Energy Dispersive X-ray Spectroscopy (EDX) spectra of $IrO_{x\text{-}(Na)\text{-}(S)}$.

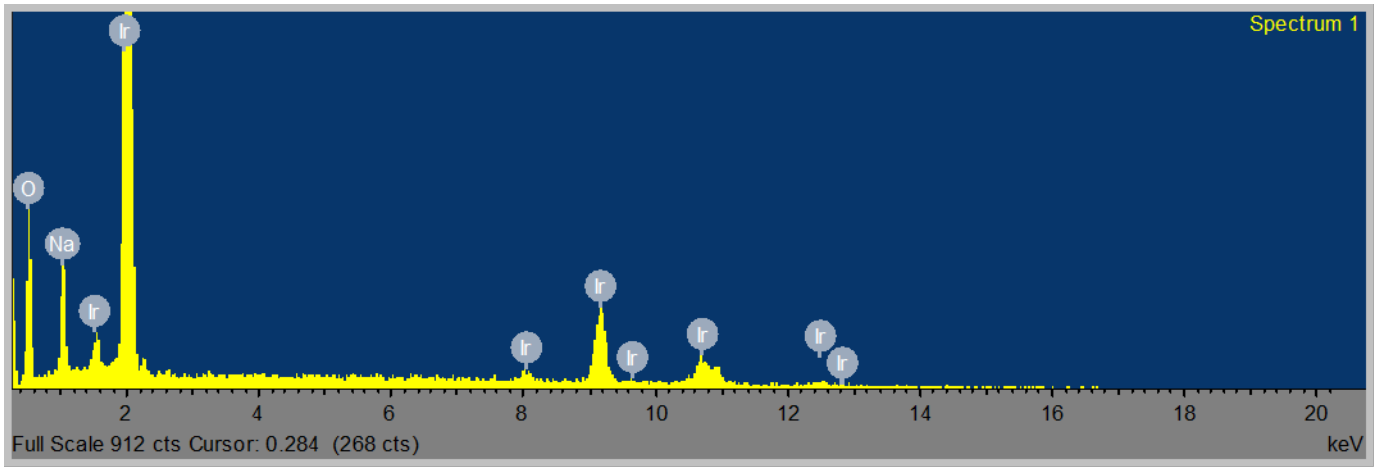

Figure A.4: Energy Dispersive X-ray Spectroscopy (EDX) spectra of $IrO_{x\text{-}(Na)\text{-}(R)}$.

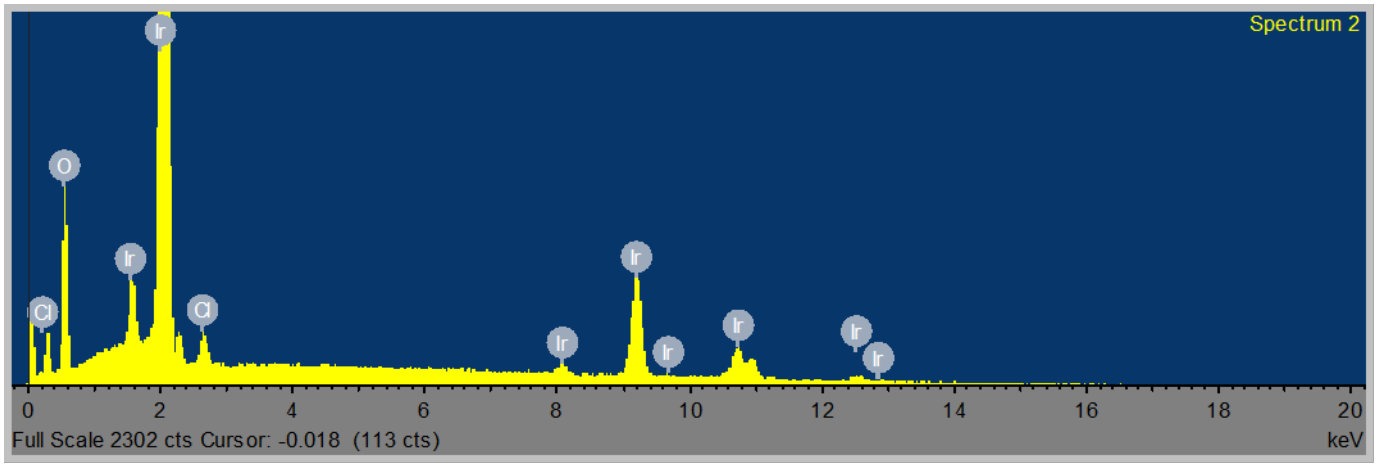

Figure A.5: Energy Dispersive X-ray Spectroscopy (EDX) spectra of $IrO_{x\text{-}(Na)\text{-}(Q)}$.

Section 4.2: Energy Dispersive X-ray Spectroscopy (EDX) spectra of Ir-based nanomaterials.

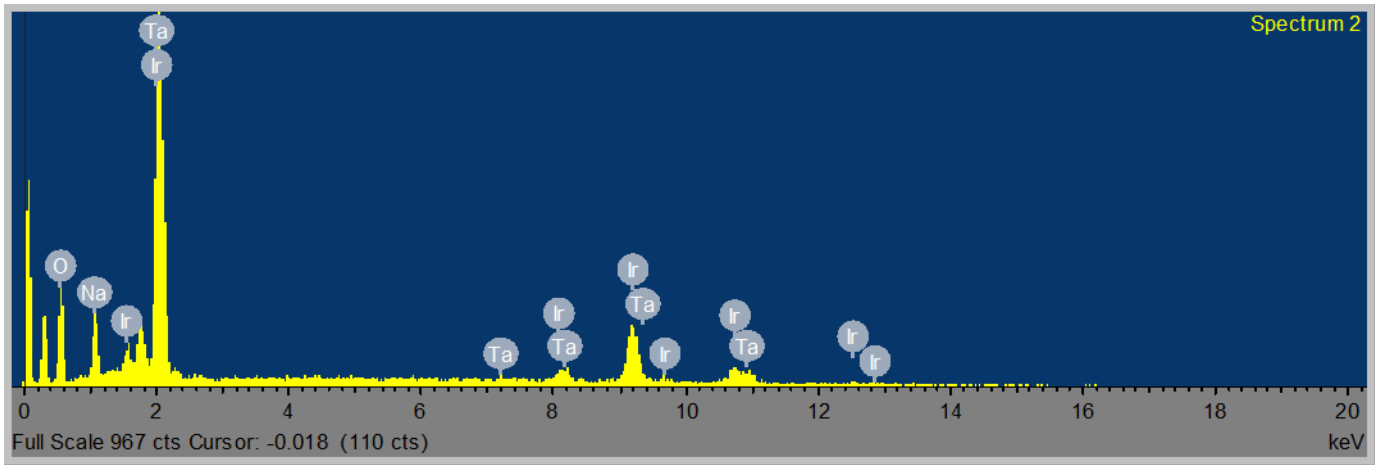

Figure A.6: Energy Dispersive X-ray Spectroscopy (EDX) spectra of $TaIrO_x$.

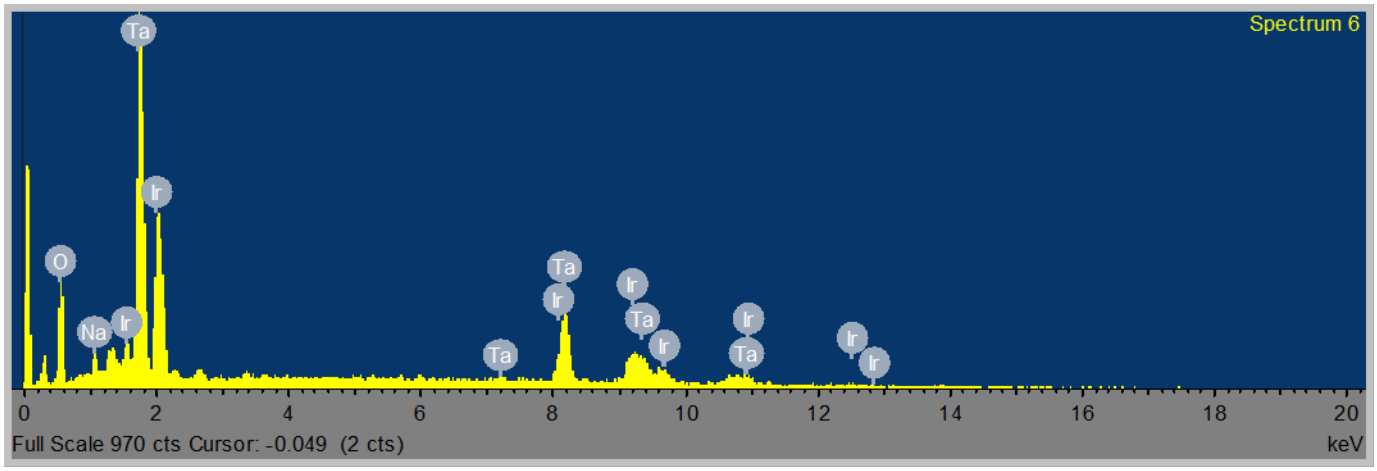

Figure A.7: Energy Dispersive X-ray Spectroscopy (EDX) spectra of IrO_x-Ta_2O_5.

APPENDIX B: CORRESPONDING ISOTHERM GRAPH AND PORE DISTRIBUTION GRAPHS

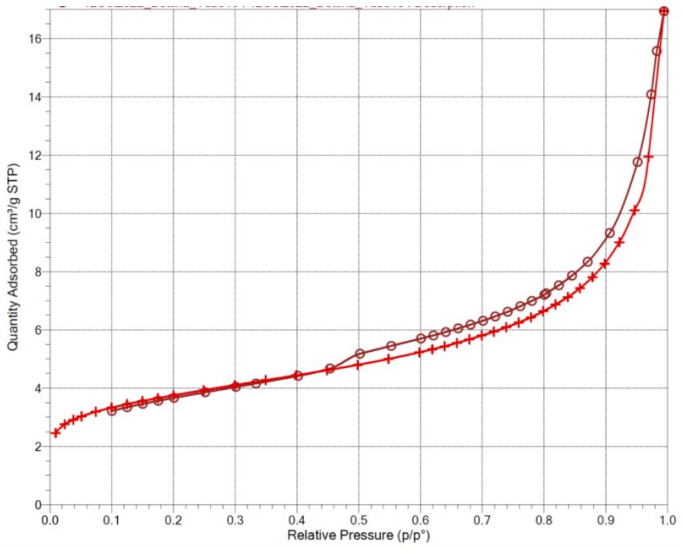

Figure B.1: Isotherm linear plot of $IrO_{x\text{-}(Na)}$.

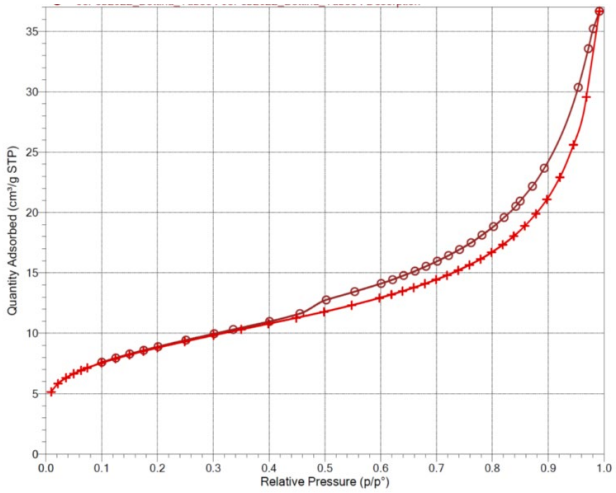

Figure B.2: Isotherm linear plot of $IrO_{x\text{-}(Ba)}$.

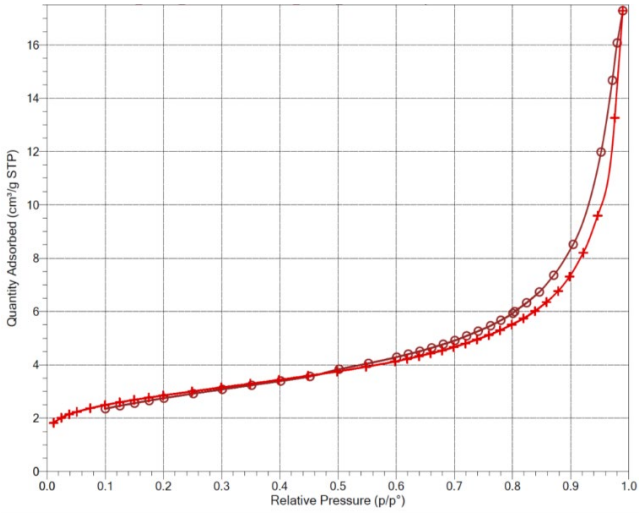

Figure B.3: Isotherm linear plot of $IrO_{x\text{-}(Na)\text{-}(S)}$.

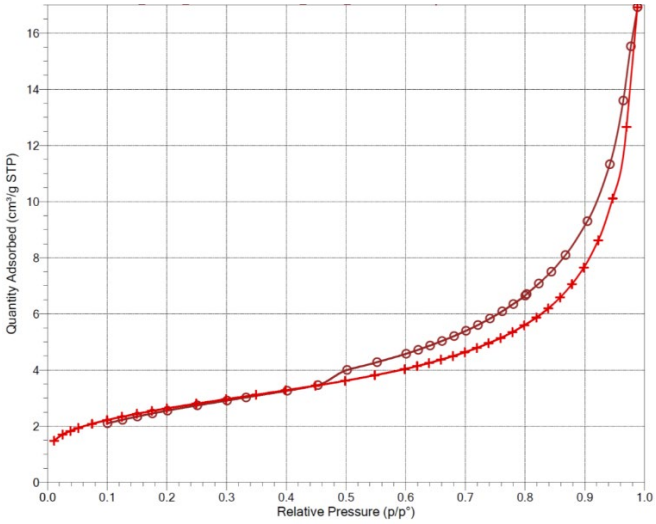

Figure B.4: Isotherm linear plot of $IrO_{x\text{-}(Na)\text{-}(R)}$.

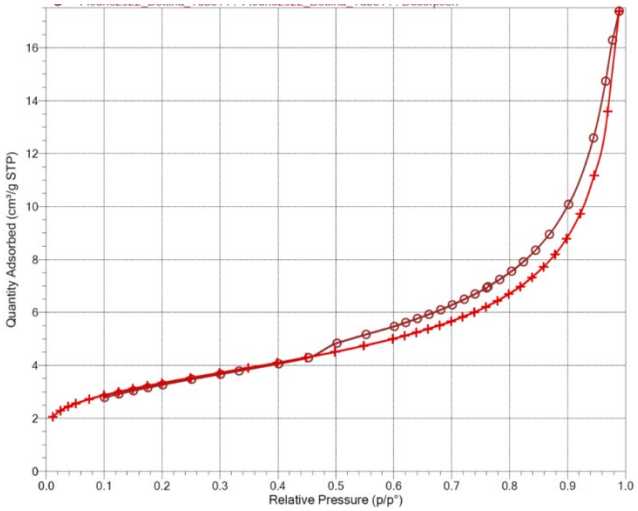

Figure B.5: Isotherm linear plot of $IrO_{x\text{-}(Na)\text{-}(Q)}$.

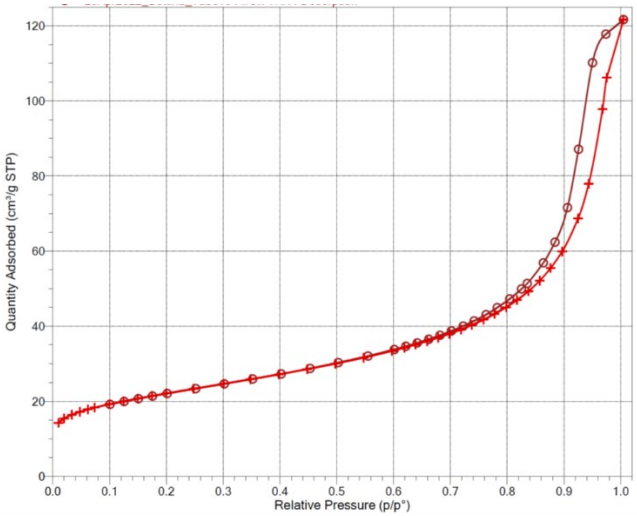

Figure B.4: Isotherm linear plot of TKK.

APPENDIX C: X-RAY PHOTOELECTRON SPECTROSCOPY SURVEY SPECTRA

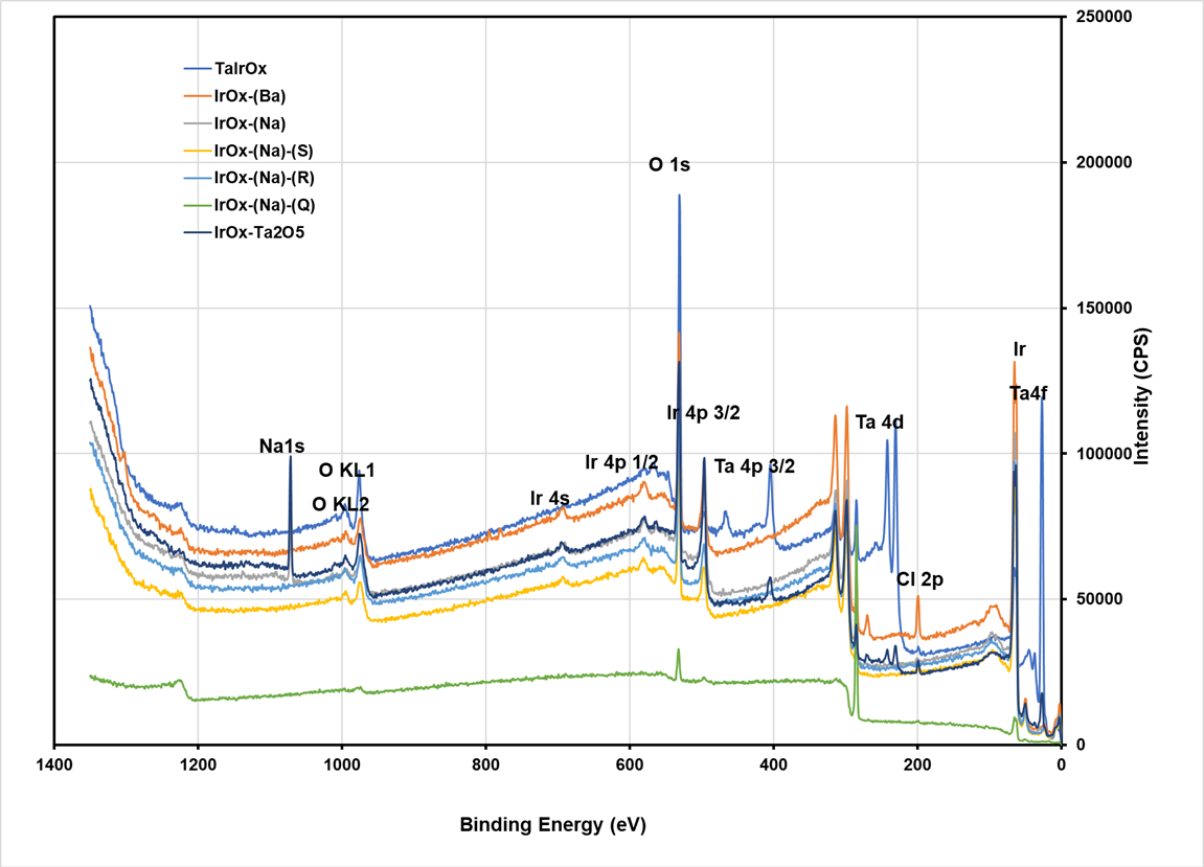

Figure C.1: X-ray photoelectron spectroscopy survey spectra